LITHOLOGIC DISCRIMINATION AND MAPPING BY ASTER
THERMAL INFRARED IMAGERY

A THESIS SUBMITTED TO
THE GRADUATE SCHOOL OF NATURAL AND APPLIED SCIENCES
OF
MIDDLE EAST TECHNICAL UNIVERSITY

BY

ÜNAL OKYAY

IN PARTIAL FULFILLMENT OF THE REQUIREMENTS
FOR
THE DEGREE OF MASTER OF SCIENCE
IN
GEOLOGICAL ENGINEERING

AUGUST 2012

Approval of the thesis:

LITHOLOGIC DISCRIMINATION AND MAPPING BY ASTER THERMAL INFRARED IMAGERY

submitted by **ÜNAL OKYAY** in partial fulfillment of the requirements for the degree of **Master of Science in Geological Engineering Department, Middle East Technical University** by,

Prof. Dr. Canan ÖZGEN   _____
Dean, Graduate School of **Natural and Applied Sciences**

Prof. Dr. Erdin BOZKURT   _____
Head of Department, **Geological Engineering**

Assoc. Prof. Dr. M. Lütfi Süzen   _____
Supervisor, **Geological Engineering Department, METU**

Prof. Dr. Nuretdin Kaymakçı   _____
Co-Supervisor, **Geological Engineering Department, METU**

Examining Committee Members:

Assist. Prof. Dr. Arda Özacar   _____
Geological Engineering, METU

Assoc. Prof. Dr. M. Lütfi Süzen   _____
Geological Engineering, METU

Prof. Dr. Nuretdin Kaymakçı   _____
Geological Engineering, METU

Çağıl Kolat, PhD.   _____
VERISIS Inc.

Nihat Serkan Öztan, MSc.   _____
Remote Sensing Center, MTA

                                                      Date: _____

I hereby declare that all information in this document has been obtained and presented in accordance with academic rules and ethical conduct. I also declare that, as required by these rules and conduct, I have fully cited and referenced all material and results that are not original to this work.

Name, Last name   : Ünal OKYAY

Signature   :

ABSTRACT

LITHOLOGIC DISCRIMINATION AND MAPPING BY ASTER THERMAL INFRARED
IMAGERY

OKYAY, Ünal

M.Sc, Department of Geological Engineering
Supervisor: Assoc. Prof. Dr. M. Lütfi Süzen
Co-Supervisor: Prof. Dr. Nuretdin Kaymakçı

August 2012, 95 pages

In conventional remote sensing, visible-near infrared (VNIR) and shortwave infrared (SWIR) part of the electromagnetic spectrum (EMS) have been utilized for lithological discrimination extensively. Additionally, TIR part of the EM spectrum can also be utilized for discrimination of surface materials either through emissivity characteristics of materials or through radiance as in VNIR and SWIR. In this study, ASTER thermal multispectral infrared data is evaluated in regard to lithological discrimination and mapping through emissivity values rather than conventional methods that utilize radiance values. In order to reach this goal, Principle Component Analysis (PCA) and Decorrelation Stretch techniques are utilized for ASTER VNIR and SWIR data. Furthermore, the spectral indices which directly utilize the radiance values in VNIR, SWIR and TIR are also included in the image analysis. The emissivity values are obtained through Temperature-Emissivity Separation (TES) algorithm. The results of the image analyses, except spectral indices, are displayed in RGB color composite along with the geological map for visual interpretation. The results showed that utilizing emissivity values possesses potential for discrimination of organic matter bearing surface mixtures which has not been possible through the conventional methods. Additionally, PCA of emissivity values may increase the level of discrimination even further. Since the emissivity utilization is rather unused throughout in literature and new, further assessment of accuracy is highly recommended along with the field validations.

Keywords: ASTER, Thermal Remote Sensing, TIR, Temperature-Emissivity Separation (TES), Lithologic Discrimination

ÖZ

ASTER ISIL KIZILÖTESİ GÖRÜNTÜLERİNİ KULLANARAK LİTOLOJİK AYRIM VE HARİTALAMA

OKYAY, Ünal

Yüksek Lisans, Jeoloji Mühendisliği Bölümü

Tez Yöneticisi: Doç. Dr. M. Lütfi Süzen

Ortak Tez Yöneticisi: Prof. Dr. Nuretdin Kaymakçı

Ağustos 2012, 95 sayfa

Geleneksel uzaktan algılamada, litolojik ayrım ve haritalama amacıyla, elektromanyetik tayfın görülebilir-yakın kızılötesi ve kısa dalga kızılötesi verileri geniş bir biçimde kullanılmaktadır. Buna ek olarak elektromanyetik tayfın ısıl kızılötesi bölümü de; hem yayımlılık değerleri, hem de görülebilir-yakın kızılötesi ve kısa dalga kızılötesi bölgelerinde olduğu gibi ışınılık değerleri kullanılarak litolojik ayırım ve haritalamada kullanılabilmektedir. Bu çalışmada, çok bantlı ASTER ısıl kızılötesi verileri, litolojik ayırım ve haritalama bakımından değerlendirilmiştir. Bu değerlendirmede litolojik ayırım ve haritalamada ışınırlık değerlerine bağlı geleneksel yöntemler yerine yayımlılık değerlerinin kullanımına yer verilmiştir. Bu bağlamda, görülebilir-yakın kızılötesi ve kısa dalga kızılötesi verileri için temel bileşen analizi ve ilişkisiz gerdirme teknikleri kullanılmıştır. Buna ek olarak, görülebilir-yakın kızılötesi, kısa dalga kızılötesi ve ısıl kızılötesi ışınırlık değerlerinin direkt olarak kullanıldığı tayfsal indislerde görüntü analizinde kullanılmıştır Isıl kızılötesi verilerinde yayımlılık değerleri, sıcaklık-yayımlılık ayırma tekniği kullanılarak elde edilmiştir. Tayfsal indisler dışında elde edilen sonuçlar RGB temel renk birleşiminde gösterilmiştir. Tüm görüntüler görsel yorumlama için çalışma alanının jeolojik haritasını da içermektedir. Sonuçlar, yayımlılık değerlerinin kullanımının organik madde ihtiva eden yüzey malzemeleri ayrımında potansiyele sahip olduğunu göstermektedir. Buna ek olarak,, yayımlılık değerlerinin temel bileşen analizi litolojik ayırım seviyesini artırabilmektedir. Yayımlılık değerlerinin kullanımı alışagelmemiş ve yeni bir yöntem olduğundan ilave inceleme ve arazi doğrulaması yüksek derecede önerilmektedir.

Anahtar Kelimeler: Isıl Uzaktan Algılama, TIR, Sıcaklık-Yayımlılık Ayırımı, TES, ASTER, Litolojik Ayırım

To my Dad

ACKNOWLEDGEMENTS

TABLE OF CONTENTS

LIST OF TABLES

TABLES

LIST OF FIGURES

FIGURES

CHAPTER 1

INTRODUCTION

Remote Sensing techniques including analog aerial photographs and digital airborne or spaceborne images have been utilized for over half a century for geological purposes. One of the most widespread uses of remote sensing in geology is detection and identification of surface materials and structures. The spatial and spectral resolutions of the images have been the key factors for discrimination of surface materials.

Multispectral imaging systems provide information regarding from the surface materials and utilizes wide range on the electromagnetic spectrum from visible part to thermal region. In other words, multispectral imaging systems provide information from the range of the electromagnetic spectrum (EMS) that is visible to human eye to non-visible range extending from near-infrared, shortwave infrared to thermal and microwave region. Therefore, they can be used to discriminate materials which may have exactly same color within the visible range while having different response in non-visible part of the EMS. In such instances they are much useful than even human eye in an outcrop.

Most of the multispectral imaging systems cover the visible-near infrared (VNIR) and shortwave infrared (SWIR) region of the spectrum. Additionally, some of them such as LANDSAT and ASTER imaging systems cover mid-long wave infrared region also known thermal infrared (TIR) region. As in VNIR and SWIR, the TIR radiance values of materials can be used for surface material discrimination and mapping. However, the chief purpose of the thermal systems has been to recover the land surface temperatures, provided that the emissivity information is known a priori. On the other hand, these imaging systems can also be used for recovering

emissivity information if the temperature is known or estimated. For this purpose several techniques have been developed for recovering emissivity and temperature values of surface materials. Emissivity is pertinent to any material and rather than radiances, emissivity values can be used for discrimination of surface materials.

Studies concerning surface material discrimination and mapping, regardless of the approach and technique preferred, used either radiance or reflectance values of materials in VNIR, SWIR and TIR. In this study, essentially band radiance values have been utilized for image analyses which include principal component analysis (PCA), decorrelation stretch and spectral indices for material discrimination and mapping. In addition to radiance, band emissivities calculated through Temperature-Emissivity Separation (TES) algorithm have also been utilized for discrimination and mapping purposes.

1.1. Purpose and Scope

The purpose of this study is to evaluate the ASTER thermal multispectral infrared data for lithological discrimination and mapping through emissivity; more precisely, to evaluate the capacity and usability of emissivity with respect to radiance in regard to level of discrimination and mapping

In this manner the main scope of this study is not only applying temperature-emissivity separation in order to recover emissivity values and interpret the results accordingly but also applying previously suggested remote sensing techniques for VNIR, SWIR and TIR for surface material discrimination and mapping.

1.2. Research Questions

- Can the emissivity values of materials be used for surface material discrimination and mapping?
- Does utilization of emissivity for surface material discrimination increase the level of discrimination over utilization of radiance? i.e. Can surface material that cannot be identified through radiance/reflectance be discriminated through emissivity?

1.3. Study Area

The study area is located within the Çankırı Basin in northern central Anatolia. Essentially, the boundaries of the study area is determined by the coverage of the used ASTER scene which extends from the area between Çankırı and Süleymanlı settlements in the west, İskilip in the northeast; Satıyüzü village in the middle, Dedeköy region in the south; Yapraklı, Ovacık, Tatlıpınar, Kayacık and Bayat regions in the north and northwest.
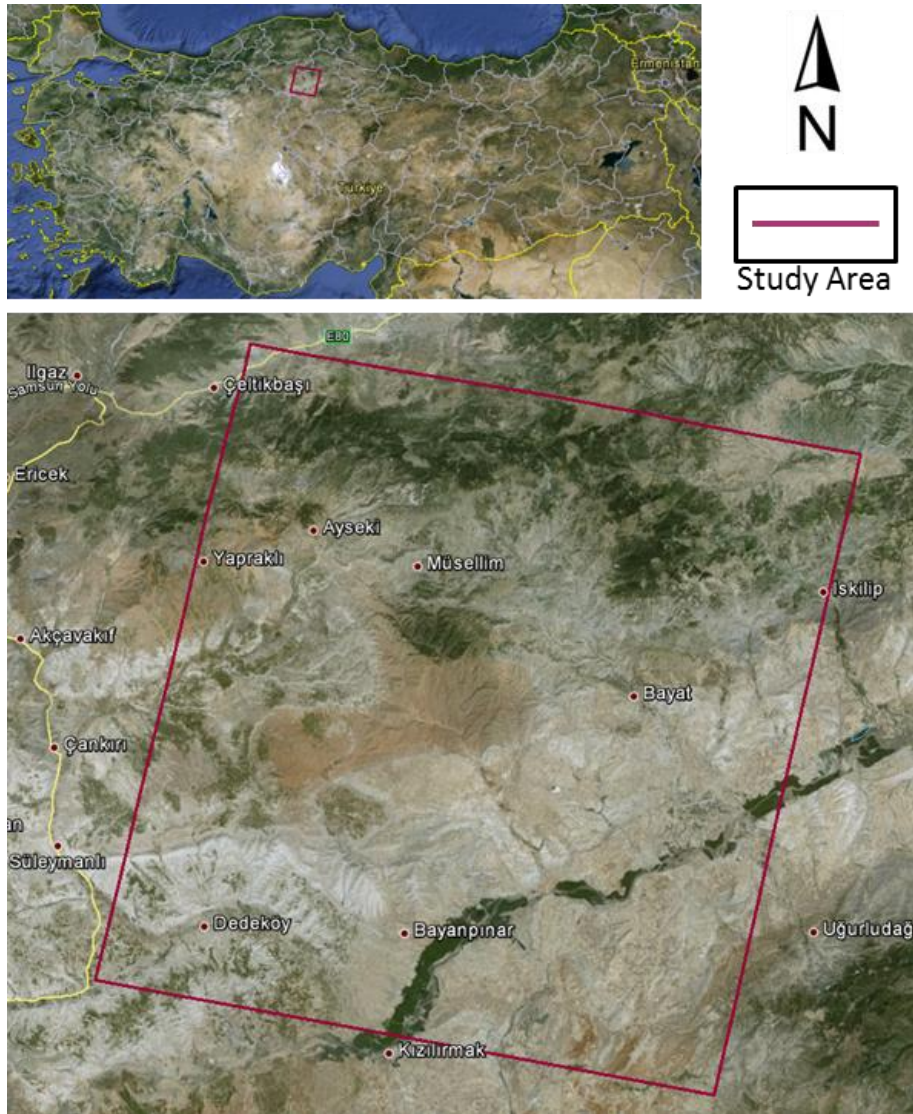
Figure 1.1. Location of the study area

1.4. Organization of the thesis

This thesis includes six chapters and the contents of the chapters are as follows: **Chapter 1** defines the purpose and scope of the thesis along with the study area; **Chapter 2** includes the geology of the study area. In this chapter the stratigraphy of the Çankırı Basin within the study area is compiled briefly; **Chapter 3** covers the background information about fundamentals of thermal radiation, use of thermal remote sensing for surface material discrimination and temperature-emissivity separation algorithm; **Chapter 4** is the main part of the thesis that includes the data analyses; **Chapter 5** gives the results of the image analyses; and finally **Chapter 6** includes the discussion, conclusion, limitations and recommendations for the future work.

CHAPTER 2

GEOLOGY

The Çankırı basin straddles the İzmir-Ankara-Erzincan Suture Zone (IAESZ) between Sakarya Continent in the north and Kırşehir Block in the south is and one of the largest Tertiary basins in Turkey with possible economic hydrocarbon and industrial mineral (mainly evaporatic) reserves. It is bounded in the west, north and the east by the North Anatolian Optiolitic Mélange belt (Kaymakçı et al., 2000)

The accumulation on Çankırı Basin happened in 5 different cycles of sedimentation (Kaymakçı et al., 2010). These cycles are represented as (1) Upper Cretaceous to Paleocene volcanoclastic rocks (Yaylaçayı and Yapraklı formations), regressive shallow marine units and Paleocene mixed environment red clastics and carbonates (Dizilitaşlar, Kavak and Badiğin formations; (2) Paleocene to Oligocene regressive flysch to molasses sequence (Yoncalı, Karabalçık and Osmankahya Formations), Middle Eocene nummulitic limestone (Kocaçay Formation), Middle Eocene to Oligocene continental red clastics (İncik formation) and Oligocene evaporites (Güvendik Formation); (3) Early to Middle Miocene fluvio-lacustrine clastics (Çandır Formation) and Tortonian evaporates Tuğlu Formation; (4) Upper Miocene fluvio-lacustrine deposits alternating with evaporites (Süleymanlı and Bozkır formations); (5) Plio-Quaternary alluvial fan and recent alluvium deposits. Within the studied portion of the Çankırı Basin, however, not all the units mentioned above are exposed. The study area comprises mainly Oligocene, Neogene and Quaternary units. Thus, the stratigraphy is compiled accordingly. Figure 2.1 depicts the generalized columnar section within the study area. The extent of the study area over the Çankırı Basin and exposed units are shown on Figure 2.2.

AGE				STRATIGRAPHY
			Quaternary	Alluvium (Qual)
TERTIARY	NEOGENE		Pliocene	Deyim Fm
			Miocene	Bozkır Fm
				Süleymanlı Fm
				Tuğlu Fm
				Çandır Fm
	PALEOGENE		Oligocene	Güvendik Fm / İncik Fm
			Eocene	Paleocene-Eocene Units
			Paleocene	
LATE CRETACEOUS				Upper Cretaceous
				Ophiolites and NAOM
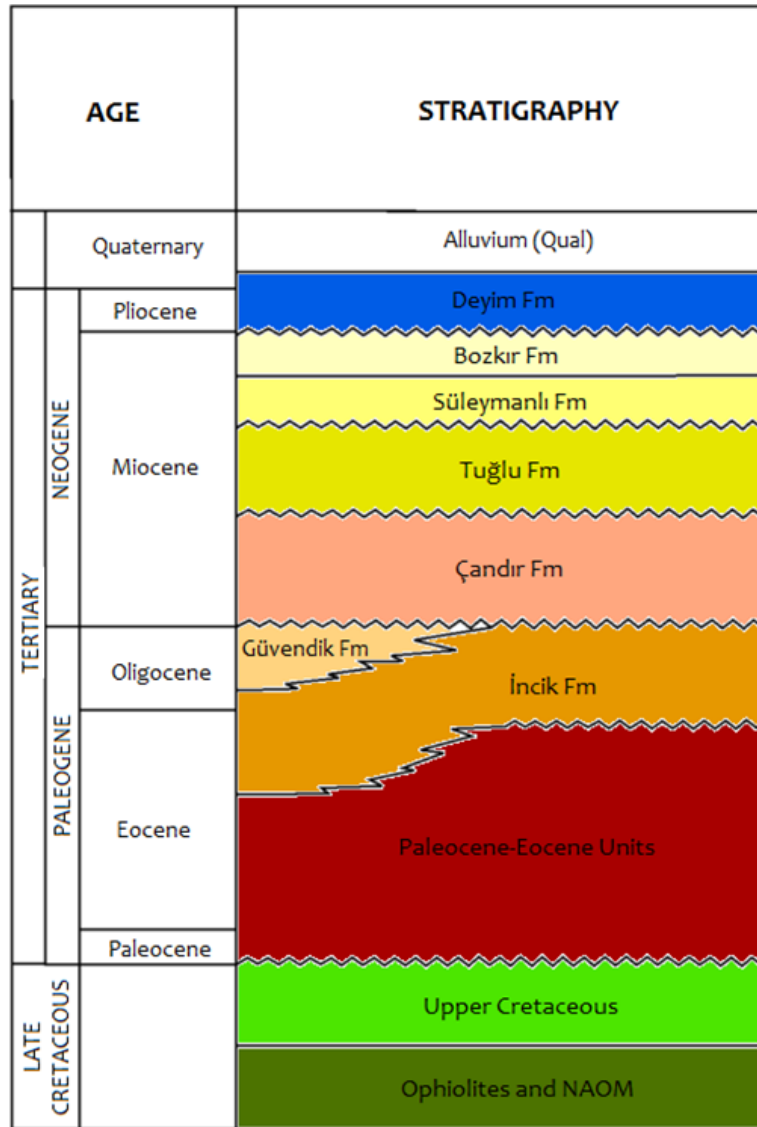
- ■ Deyim Formation (fluvial clastics)
- □ Bozkır Formation (evaporites)
- ■ Süleymanlı Formation (fluvio-lacustrine red clastics)
- ■ Tuğlu Formation (evaporites and lacustrine shale/marl)
- ■ Çandır Formation (fluvio-lacustrine sediments)
- ■ Güvendik Formation (evaporites)
- ■ İncik Formation (continental red clastics)
- ■ Paleocene-Eocene Units
- ■ Upper Cretaceous
- ■ Ophiolites and NAOM

Figure 2.1 Generalized columnar section of the Çankırı Basin within the study area
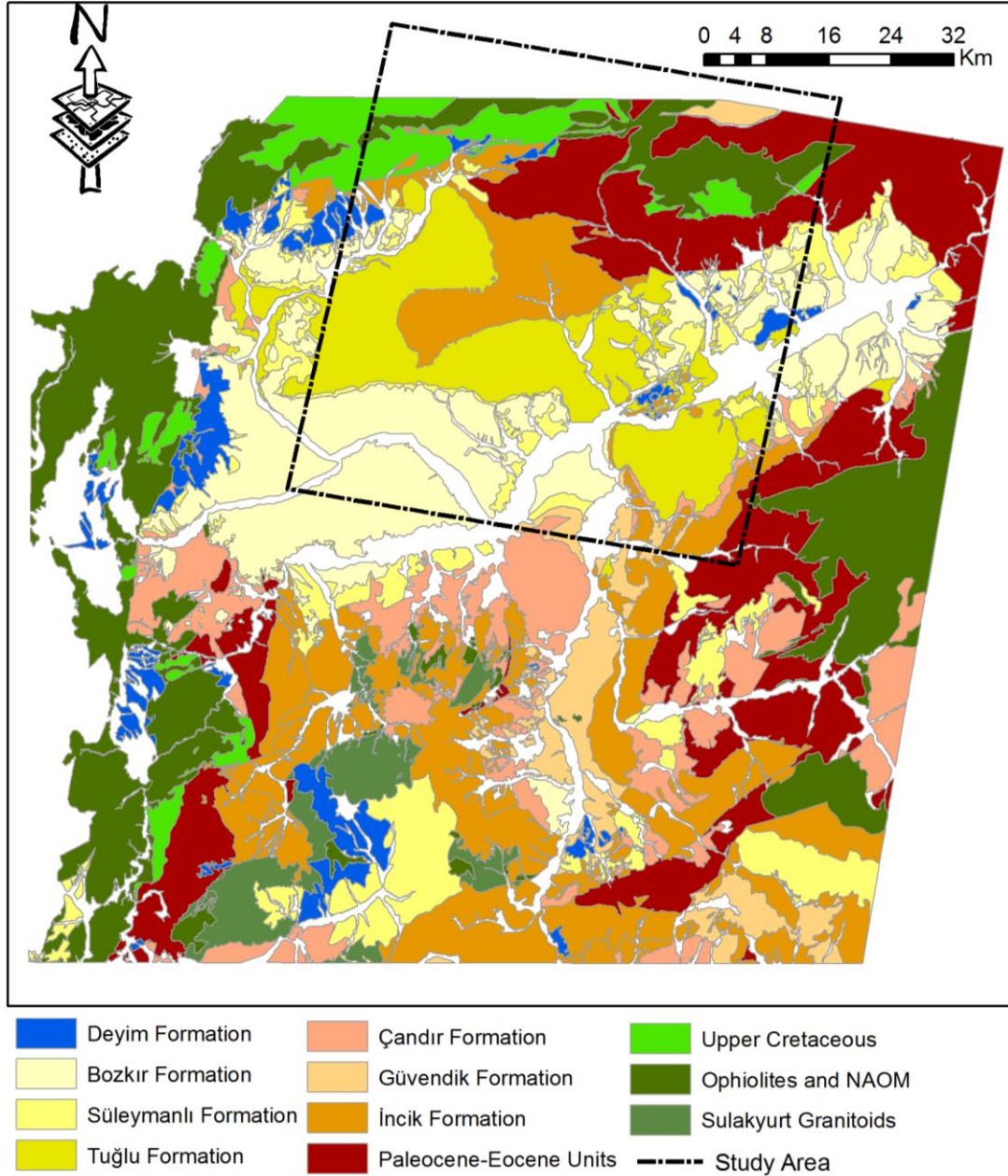
Figure 2.2 Geological map of the Çankırı Basin with the extent of the study area

2.1. Stratigraphy

2.1.1. Pre-Oligocene Units

Ophiolites and North Anatolian Ophiolitic Mélange (NAOM)

North Anatolian Ophiolitic Mélange (NAOM) forms the rim of the Çankırı Basin from west to east through north and exposed in the north of the study area. NAOM is considered to be underlying much of the Çankırı Basin. Tectonic mixture of spilites, pillow lavas, diabease dykes, red to purple radiolarian chert, cherty limestone, reddish pelagic mudstone and serpentinized ultramafic rocks such as peridotites and pyroxinites forms the lithological composition of the NAOM along with gabbros, plagio-granites, basement metamorphic blocks from Sakarya Continent and derived limestones from nearby platforms (Koçyiğit et al., 1988; Koçyiğit, 1991; Rojay, 1993; Özçelik, 1994).

Upper Cretaceous Units

Upper Cretaceous units within the study area are mainly composed of volcano-sedimentary sequence and exposed in the north of the study area. Marly pelagic limestone-volcanogenic sandstone-tuff alternation, micritic limestone-green shale alternation, sandstone-green shale alternation, agglomerate and beige benthic fossil bearing limestone (Yaylaçayı Formation); Macrofossil bearing limestone, silty argillaceous limestone, white tuff and agglomerate intercalations, yellow-buff volcanogenic conglomerate sandstone, gray, green, reddish shale and limy units (Yapraklı Formation) comprise the Upper Cretaceous units (Kaymakçı et al., 2001).

Paleocene-Eocene Units

Paleocene units are exposed in the north-east of the study area. These units are overlain by Upper Cretaceous units, Ophiolites and NAOM. Red clastics and carbonates (Kavak Formation); Neritic limestones (Badiğin Formation); Turbidites and intercalated limestones (Dizilitaşlar and Hacıhalil Formation); Flysch (Yoncalı Formation); Conglomerates and sandstone with coal seams (Karabalçık Formation); Clastics from Kırşehir Block (Karagüney Formation); Clastics from granitoids (Mahmatlar Formation); Volcanics and volcanoclastics (Bayat Formation); Mixed environment clastics and red bends (Osmankahya Formation) and Nummulitic limestone (Kocaçay Formation) comprise the Paleocene-Eocene units (Kaymakçı et al., 2010).

2.1.2. İncik Formation (Ti, post-Middle Eocene – Oligocene)

The İncik formation is the most widespread and voluminous unit of the Çankırı Basin. The formation is characterized by alternation of very thick bedded red conglomerates with very thick bedded red sandstones and purple to brick red thick to very thick bedded mudstones in the northern and south-western parts of the basin; by creamy white gypsum which laterally and vertically grades into green shale in the eastern part of the basin (Kaymakçı et al., 2000). Higher up in the eastern part, the formation is characterized by an alternation of brick red to purple sandstones, siltstones, shale and greenish gray to bluish shale and very thick bedded red to orange gypsum layers (Kaymakçı et al., 2001).

2.1.3. Güvendik Formation (Tg, Oligocene)

The Güvendik Formation intensely deformed at the bottom and at the top, however, Kaymakçı (2000) recognized three distinct levels: (1) at the bottom and (2) at the top very thick bedded finely laminated and intensely deformed gypsum alternating with thin to medium bedded buff to creamy white gypsiferous marls; and (3) in the middle greenish gray shales scoured by lenses of micro-conglomerate (Kaymakçı et al., 2001).

2.1.4. Çandır Formation (Tç, Burdigalian(?) – Serravallian)

The extent of the Çandır Formation is exposed mainly in the SW and southern part of the study area. The formation unconformably overlies Pre-Neogene units while it is unconformably overlain by Süleymanlı and Bozkır formations (Kaymakçı et al. 2001).

The formation is characterized by an alternation of red to pink, buff to creamy white pebbly mudstone, clayey limestone, siltstone, matrix supported conglomerate intercalated with white limy-marl, thin silty-limestone, oolite bearing limestone, clayey limestone and very thin organic rich layers at the bottom; alternation of red to pink sandy-silty mudstone, loose matrix supported conglomerates, clayey sandstone, siltstone intercalated with caliche limestone, paleosol layers with carbonate concretions and cross bedded sandstone and conglomerates locally discordant with these layers in the middle; and pink sandy, limy-concretion bearing mudstone, clayey porous limestone, siltstone, silty-limestone, white to creamy white marl, greenish shale alternations and clayey, pebbly sandstone intercalations at the top (Kaymakçı et al, 2001).

2.1.5. Tuğlu Formation (Ttu, Tortonian)

The Tuğlu Formation unconformably overlies Çandır Formation, Güvendik Formation and other Pre-Neogene units while it is unconformably overlain by Süleymanlı Formation (Kaymakçı et al., 2001).

The formation is characterized by dark gray shale, mudstone, siltstone and sandstone alternations at the bottom; alternation of green, pelecypoda bearing stiff bentonitic claystone and dark green to gray organic rich mudstone, intercalated with cherty limestone beds and lenses of conglomerate along with very thin coal seams in the middle; and at the top it gradually becomes marl dominated and grades laterally into alternation of thick-bedded white gypsum and thick bedded yellow to pinkish silty mudstone (Kaymakçı et al., 2001)

2.1.6. Süleymanlı Formation (Ts, Messinian – Pliocene)

The Süleymanlı Formation laterally and vertically grades into the Bozkır Formation while unconformably overlies the Tuğlu Formation along with Çandır formation and older formations (Kaymakçı et al., 2001).

The formation is characterized mainly by an alternation of thin bedded red to buff, brick re mudstone, gray marl with small gastropod fragments, buff laminated mudstone, thin bedded siltstone, silty and sandy mudstone alternation while at the bottom the formation is dominated by conglomerates along western margin of the Çankırı Basin and at the top it becomes finer and more shale-mud dominated into the center of the basin (Kaymakçı et al., 2001). Moreover, the formation laterally grades into Bozkır Formation which comprises a very thick white gypsum alternating with white yellow to buff marl and red mudstone at the top (Kaymakçı et al., 2001).

2.1.7. Bozkır Formation (Tbo, Messinian – Pliocene)

The Bozkır Formation overlies on the Çandır Formation while is overlain unconformably by Deyim Formation (Kaymakçı et al. 2001). The formation grades vertically and laterally into Süleymanlı Formation.

The formation is mainly characterized by alternation of gypsum with marls and thin bedded sandstones while the dominant lithology is white to pale gray gypsum (Kaymakçı et al. 2001). In

the central part of the basin thick bedded re-crystallized gypsum and thin bedded yellow to buff gypsum flakes bearing marl dominate the formation (Kaymakçı et al. 2001). In the area to west of Bayat, the formation comprises an alternation of white and pinkish beds where the white layers are characterized by an alternation of thin bedded to laminated gypsum with thin bedded shale-marl (Kaymakçı et al. 2001).

2.1.8. Deyim Formation (Tde, Gelasian – Early Quaternary)

The Deyim Formation is overlain by Quaternary alluvium unconformably while the formation unconformably overlies the older units (Kaymakçı et al. 2001).

The Deyim Formation is characterized mainly by variable sized, poorly sorted, polygenic loose conglomerates/gravel and sandstone (loosely compacted coarse clastics) with intercalation of minor fine clastics (siltstone and mudstone) (Kaymakçı et al., 2001).

CHAPTER 3

THERMAL REMOTE SENSING

3.1. Fundamentals of Thermal Radiation

Thermal radiation is the emission of electromagnetic radiation generated by the thermal motion of charged particles in matter. All bodies with a temperature greater than the absolute zero have thermal energy. Thermal energy results in kinetic energy with the random movements of atoms and molecules in matter. These atoms and molecules are composed of charged particles i.e. protons and electrons. Interaction of these particles with each other creates charge acceleration and dipole oscillation. Subsequently, this results in the emission of photons radiating away from the surface of the matter.

3.1.1. Blackbody Concept

A black-body is an idealized hypothetical radiator that totally absorbs and re-emits incident electromagnetic radiation, regardless of frequency or angle of incidence (Landsberg, 1990). Hence, a black-body does not reflect or transmit radiation. As stated, all matter have a temperature greater than absolute zero emits electromagnetic radiation, therefore electromagnetic radiation emitted from a black-body in thermal equilibrium, i.e. at constant temperature, is called black-body radiation. In that sense black-body reemits all the radiation it absorbs.

3.1.1.1 The Planck's Law

Black-body radiation has a characteristic, continuous frequency spectrum (radiance curve) that depends only on the temperature since a black-body emits radiation in all wavelengths. The

emissive power – energy radiated – of a black-body at any wavelength and temperature is explained by Planck's Law (Eq.3.1) (Planck, 1914). The radiance curve of a black-body is peaked at a characteristic frequency, and therefore a characteristic wavelength, that shifts to higher frequencies with increasing temperature (Figure 3.1). In other words, the amount of radiation a black-body emits increases along with increasing temperature. Conversely, the amount of radiation decreases along with increasing wavelength.

$$L_{BB(\lambda)} = \frac{C_1}{\lambda^5 \pi [e^{\frac{C_2}{\lambda T_{BB}}} - 1]}$$ (Eq.3.1)

where
$L_{BB(\lambda)}$ *spectral blackbody radiance [W/(m^2 sr µm)];*
λ *wavelength [µm];*
T_{BB} *temperature of blackbody [K];*
C_1 *1st fundamental physical constant 3.7415x10^{-16}W m^{-2}*
C_2 *2nd fundamental physical constant 0.0143879 m K*
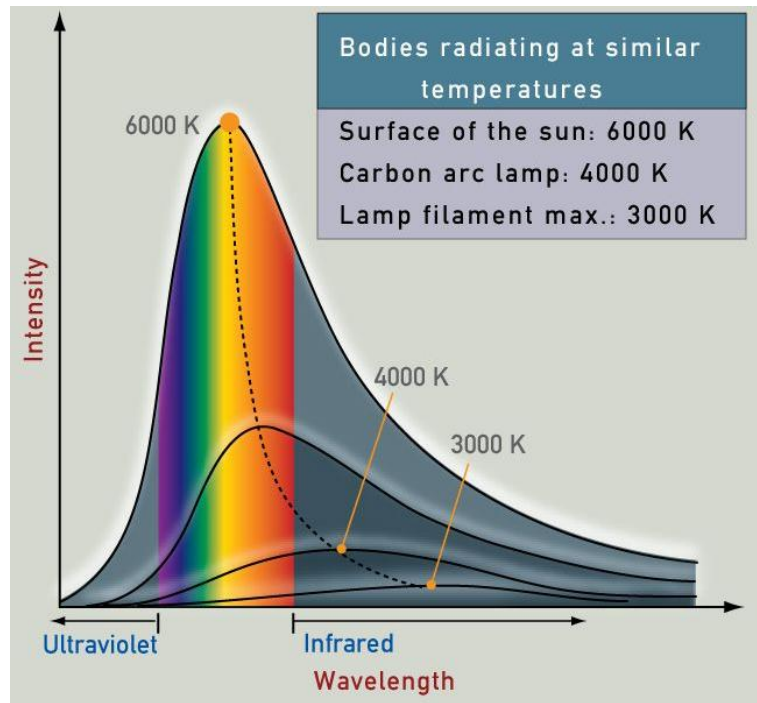
Figure 3.1 Blackbody Radiation Curves

The inferences of Planck's Law can be summarized as follows:

1. The emissive power of a black-body at any wavelength can be obtained through calculating the area under the radiance curve of the black-body.
2. The emissive power of a black-body increases along with increasing temperature regardless of the wavelength
3. Black-body emits relatively more energy in shorter wavelengths (high frequencies)
4. The peak of the black-body radiance curve that represents the maximum emissive power shifts to shorter wavelengths

3.1.1.2. The Stefan – Boltzmann Law

The total emissive power per unit surface of a black-body per unit time – also known as black-body irradiance can be explained by Stefan-Boltzmann Law (Eq.3.2). It states that the total energy is directly proportional to the fourth power of the black-body's temperature. The Stefan-Boltzmann Law utilizes a constant derived from other known constants of nature – Boltzmann constant, Planck's constant and speed of light in vacuum called Stefan-Boltzmann constant.

$$L_{BB} = \int_{\lambda=0}^{\lambda=\infty} L_{BB(\lambda)} d\lambda = \int_{\lambda=0}^{\lambda=\infty} \frac{C_1}{\lambda^5 \pi [e^{\frac{C_2}{\lambda T_{BB}}} - 1]} d\lambda = \frac{C_1 \pi^4}{15 C_2^{\;4}} (T_{BB})^4 = \sigma (T_{BB})^4 \qquad \text{(Eq.3.2)}$$

where
L_{BB} total spectral blackbody radiance [W/m^2];
$L_{BB(\lambda)}$ spectral blackbody radiance [W/(m^2 sr µm)];
λ wavelength [µm];
T_{BB} temperature of blackbody [K];
C_1 1st fundamental physical constant 3.7415x10^{-16}W m^{-2}
C_2 2nd fundamental physical constant 0.0143879 m K
σ Stefan-Boltzmann constant, 5.6697x10^{-8} Wm^{-2}K^{-4}

3.1.1.3. The Wien's Displacement Law

The wavelength of the maximum emissive power i.e. wavelength of the peak of the black-body radiance curve is explained by Wien's Law. The Wien's Displacement Law states that the wavelength distribution of black-body radiation has essentially the same shape at any temperature. From the general law, it follows that there is an inverse relationship between the wavelength of the peak of the emission of a black-body and its temperature when it is

expressed as a function of wavelength (Eq.3.3). In other words, Wien's displacement Law implies that the hotter an object is the shorter the wavelength at which it will emit most of its radiation and also that the wavelength for peak radiation power is found by dividing Wien's constant by the temperature in Kelvin.

$$\lambda_m = \frac{A}{T_{BB}}$$

(Eq.3.3)

where
A   *Wien's constant 2897.768 μm K*
λ_m   *wavelength of maximum spectral radiance [μm];*
T_{BB}   *temperature of blackbody [K];*

3.1.2. Interactions of Thermal Radiation with Terrestrial Materials

Incident radiation interacts with the surface of the terrestrial materials. This interaction can be diversion of the radiation, absorption of the radiation which could be used to increase the internal energy or transmission of the radiation. So, the incident radiation (i.e. energy) on the surface of any natural terrestrial material can be reflected, transmitted or absorbed unlike a black-body where all the energy is absorbed and re-emitted.

Part of the incident energy is reflected back to atmosphere that is the energy is lost and cannot be used by the material. The ratio between the energy reflected and the incident energy is called *reflectance (*ρ) of the material. The reflectance of the material is not constant and changes with the wavelength therefore can be further called *spectral reflectance,* ρ(λ).

Another part of the energy could be transmitted through the material. A hypothetical transparent body can transmit all the incident energy. Opaque bodies, on the other hand do not transmit energy and note that most of the terrestrial materials, particularly in remote sensing are considered being opaque. The ratio between the energy transmitted and the incident energy is called *transmittance (τ).*Similarly, the transmittance changes with the wavelength therefore can be further called *spectral transmittance,* τ(λ).

The last part of the incident energy is used by the material itself in order to increase the internal energy i.e. heat the body up. This energy is basically absorbed and stored by the material and rises the temperature of the body. The ratio between the absorbed energy and

the total incident energy is called *absorptance (α).* Along with reflectance and transmittance, absorptance also changes with wavelength and called *spectral absorptance, α(λ).*

According to conservation of energy, following equation (Eq.3.4) states the relation between the incident energy and its disposition upon interaction with terrestrial materials:

$$E_I = E_R + E_T + E_A \qquad \text{(Eq.3.4)}$$

where

E_I	incident energy on the surface of the terrestrial material;
E_R	component of the incident energy reflected by the terrestrial material;
E_T	component of the incident energy transmitted by the terrestrial material;
E_A	component of the incident energy absorbed by the terrestrial material

Furthermore, all the parameters in Eq.3.4 can be divided by the total incident energy. This operation essentially normalizes the linear equation of energy conservation (Eq.3.5). The new parameters express the reflectance, transmittance and absorptance; respectively (Eq.3.6).

$$\frac{E_I}{E_I} = \frac{E_R}{E_I} + \frac{E_T}{E_I} + \frac{E_A}{E_I} \qquad \text{(Eq.3.5)}$$

$$\rho(\lambda) = \frac{E_R}{E_I} \; ; \; \tau(\lambda) = \frac{E_T}{E_I} \; ; \; \alpha(\lambda) = \frac{E_A}{E_I} \qquad \text{(Eq.3.6)}$$

Thus, the sum of reflectance, transmittance and absorptance is equal to 1 for any terrestrial material. This relation is expressed in the following equation (Eq.3.7).

$$\rho(\lambda) + \tau(\lambda) + \alpha(\lambda) = 1 \qquad \text{(Eq.3.7)}$$

3.1.3. Emissivity

Relative ability of a surface to emit energy by radiation is called emissivity, often written as ε. In other words, the "emitting ability" of a material compared to that of a black-body is referred as emissivity of the body (Eq.3.8). Kirchhoff's Law states that for the materials in thermal equilibrium i.e. at constant temperature the spectral absorptance is equal to the spectral emissivity (Kirchhoff, 1860).

$$\varepsilon_{(\lambda)} = \frac{L_{(\lambda)}(material)}{L_{(\lambda)}(blackbody)}$$

(Eq.3.8)

where
$L_{(\lambda)}$ *spectral radiance [W/(m^2 sr μm)];*
λ   *wavelength [μm];*

As a black-body absorbs and re-emits all the incident energy, it has emissivity equals to 1 while any terrestrial material would have emissivity less than 1. Emissivity for most of the terrestrial materials ranges between 0.7 <Ɛ <1.0 (Prabhakara and Dalu, 1976). Terrestrial material that has emissivity less than 1 but constant at all wavelengths similar to a black-body is called as a **gray-body.** A **selective radiator**, on the other hand, has emissivity that varies with wavelength. Vegetation, water bodies and snow are examples of near-gray-body while other terrestrial materials are selective radiators (Figure 3.2).
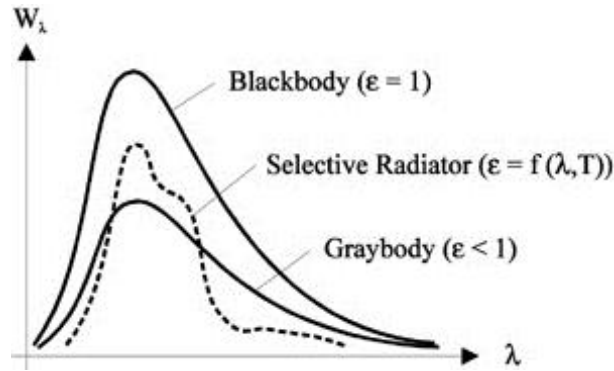
Figure 3.2 Emissivity changes of Black-body, Gray-body and Selective Radiator (*Riedl, 2001*)

In most cases, as the terrestrial materials are opaque, they transmit negligible amount of radiation if not zero. Therefore the transmittance of terrestrial materials is ignored. Based on this information equation (Eq.3.7) is simplified as follows:

$$\rho(\lambda) + \alpha(\lambda) = 1$$

(Eq.3.9)

Then the Kirchhoff's Law is introduced into the equation (Eq.3.9) and the following equation can be obtained:

$$\rho(\lambda) + \varepsilon(\lambda) = 1 \qquad \text{(Eq.3.10)}$$

As each material has characteristic spectral reflectance, each material has a distinctive emissivity signature depending on the wavelength. In other words, emissivity is an inherent property of a material. Therefore, juxtaposed materials on the surface of the earth that have the same temperature will have different emissivities. Based on equation (Eq.3.10) it can be inferred that spectral reflectance and emissivity of a material are inversely correlated i.e. the higher reflectance a material has, the lower emissivity it has or vice versa.

3.2. Use of Thermal Remote Sensing for Surface Material Discrimination and Mapping

As stated previously, multispectral and hyperspectral imaging systems sense radiation not only in visible and reflected infrared portion but also in emitted infrared i.e. thermal infrared portion of the electromagnetic spectrum. In order to detect emitted energy, the sensors of thermal imaging systems use photo detectors sensitive to direct contact of photons on the surface of the sensor. These thermal sensors measure the surface temperature and thermal properties of the Earth's surface.

The wavelength of thermal radiation, when it is compared to visible or reflected infrared radiation, is relatively long which minimizes the atmospheric scattering. However, remote sensing of thermal radiation is restricted to specific wavelengths due to total absorption of certain wavelengths by the atmospheric gases and water vapor. This is in fact also valid for visible and reflected infrared remote sensing. Therefore, two specific regions, called atmospheric windows, are used for thermal remote sensing and involve 3 to 5 μm and 8 to 14 μm ranges. Since the energy decreases with increasing wavelength, sensors of thermal imaging systems have large IFOVs in order to capture sufficient energy for reliable measurements which makes the spatial resolution of the thermal sensors relatively coarse when compared to that of visible and reflected infrared.

Data collected through airborne and spaceborne systems such as NASA Thermal Infrared Multispectral Scanner (TIMS), NASA Atlas Scanner, LANDSAT Thematic Mapper (TM), and NASA

Heat Capacity Mapping Mission (HCMM) have been used for geological purposes (Dudley-Murphy and Nash 2003). Abrams et al. (1984), Kahle et al. (1984), Hook et al. (1998), Price (1985) and Allis et al. (1999) have evaluated TIR data for geological mapping and mineral exploration. All of these authors concluded that neither the spectral nor the spatial resolution of the data gathered is adequate for geological purposes and both spectral and spatial resolutions have been the major limiting factors. New hyperspectral and multispectral instruments like Advanced Spaceborne Thermal Emission and Reflection Radiometer (ASTER) having higher spatial resolution and increased number of spectral bands that cover TIR increase the potential use of TIR for surface material discrimination and mapping.

Recent hyperspectral and multispectral TIR instruments along with various algorithms have been used for surface material discrimination and mapping by several researches. Ninomiya and Matsunaga (1997), Chabrillat et al. (2000), Ninomiya (2002, 2003), Ninomiya and Fu (2002), Ninomiya et al. (2005), Saldanha et al. (2004), Swayze et al. (2004). Hook et al. (2005), Rowan et al. (2005), Gürçay (2010) used hyperspectral and/or multispectral TIR data in order to evaluate or identify mafic/ultramafic rocks and related mineralization through absorption and emittance interactions in TIR utilizing various algorithms.

For the multispectral ASTER data TIR spectral indices defined by Ninomiya (2002, 2003) and Ninomiya and Fu (2002) are widely used. These indices are using band radiances of ASTER TIR data. The spectral index (Mafic Index) defined by Ninomiya (2002, 2003) and Ninomiya and Fu (2002) for mafic and ultramafics is basically related with the bulk silica content of the target. Apart from mafic index used for mafic and ultramafic discrimination, many other indices for quartz, carbonate and evaporate minerals are also defined and used (Ninomiya, 2002, 2003; Ninomiya and Fu, 2002; Öztan, 2008; Öztan and Süzen, 2011). Misra et al. (2007) and Corrie et al. (2010) also used the indices defined for carbonate, quartz and mafic minerals for surface material discrimination.

It is common practice in TIR remote sensing that the radiance values of the multispectral bands are directly used instead of recovering the emissivity values. Regarding the emissivity of the surface materials, generally the studies concerned with acquisition of the emissivity values for individual materials rather than mapping the materials, which resulted in a collection of values which can be considered as a spectral library of emissivities (Salisbury and D'Aria 1992a, 1992b).

3.3. Recovering Temperature and Emissivity from TIR Data

Thermal radiation originated from the surface of a material and depends on the materials kinetic energy and its emissivity. The main problem in TIR is that there are more unknowns than measurements (radiance values of different bands are known, whereas emissivity values, temperature and atmospheric parameters are unknown). The basic purpose of TIR remote sensing is to estimate the surface temperature. If the surface emissivity value is known then this information makes the problem deterministic and straightforward (Gillespie et al., 1999). As Masuda et al. (1988) indicated, the water bodies such as oceans would be suitable targets where emissivity is measured independently and same everywhere.

Several deterministic and non-deterministic approaches have been used for inversion of TIR data for temperature and emissivity. The main purpose of TIR, as stated above, has been estimating the surface temperature where emissivity is not the main concern. In that sense, TIR remote sensing of oceans, snow covers, glaciers and dense vegetation is considered to be deterministic. For most of the deterministic approaches, on the other hand, it requires atmospheric parameters to be utilized directly in order to correct the measured radiance (Gillespie et al., 1999). The correction is not always feasible since the atmospheric parameters are not always available. Several ocean- temperature studies utilized AVHRR data which has two separate TIR bands. Atmospheric effects can be compensated through the combined analysis of these bands – also called "split-windows" (Barton, 1985; McMillan and Crosby, 1984; Prabhakara et al., 1974). Brown (1994) developed a version of split-window algorithm for EOS/MODIS data. Several other studies utilized split-window technique for land surface. However, in those studies it is concluded that unknown emissivity variations cause large errors (Price, 1984; Becker, 1987; Vidal 1991). The inaccuracy over land is due to the unknown emissivities rather than atmospheric effect such that error caused by inaccuracy of only 0.01 in emissivity can be greater than that of atmospheric effects (Wan and Dozier, 1989). Therefore, the efficacy of split window on land is limited (Gillespie et al., 1999). Some of the geological studies did not attempt to separate temperature and emissivity but rather utilized decorrelation stretching through radiance values (Kahle et al., 1980; Abrams et al., 1991). Gillespie (1992) used a spectral unmixing approach for temperature and emissivity recovery and concluded that the results are imperfect.

The methods which include the temperature-independent spectral indices (TISI) (Becker and Li, 1990), the thermal log residuals and alpha residuals (Hook et al., 1992), the spectral emissivity ratios (SER) (Watson, 1992a; Watson et al., 1990), the day-night two channel (DN2C) method (Watson, 1992b), the normalized emissivity method (NEM) (Gillespie, 1985; Realmuto, 1990), alpha derived emissivity (ADE) (Hook et al., 1992; Kealy and Gabell, 1990; Kealy and Hook, 1993) and minimum-maximum difference (MMD) method (Matsunaga, 1994) are some of the approaches developed for temperature-and emissivity recovery. Gillespie et al. (1999), summarizes the drawback of these methods as follows:

1. Determine spectral shape but not temperature
2. Require multiple observations under different conditions
3. Assume a value for one of the unknowns
4. Assume a relationship between spectral contrast and emissivity
5. All require independent atmospheric correction

3.3.1 Temperature-Emissivity Separation (TES) Algorithm

The Temperature/Emissivity Separation (TES) algorithm is introduced by Gillespie et al. (1998) and basically combines two already existed approaches and added some new features. Gillespie et al. (1999) defined this algorithm closely related to MMD method of Matsunaga (1994) which is based on ADE method of Kealy and Gabell (1990), Hook et al. (1992) and Kealy and Hook (1993).

TES utilizes atmospherically corrected (land leaving) TIR radiance based on Palluconi et al. (1994). This includes correction for atmospheric transmissivity and upwelling atmospheric path radiance. The reflected down-welling sky irradiance (reported in ASTER standard product), on the other hand, cannot be removed in the absence of emissivity information. Therefore, reflected down-welling sky irradiance is removed iteratively. Essentially, TES algorithm has three modules: (1) NEM Module, (2) Ratio Module (RAT) and (3) MMD Module all of which are summarized below.

3.3.1.1. NEM Module

Normalized Emissivity Method (NEM) was first introduced by Gillespie (1985) and is used for estimating the initial surface kinetic temperature while subtracting the reflected sky irradiance

iteratively. Basically, the maximum emissivity value (ε_{max}) for ASTER bands 10-14 is estimated in order to calculate temperature and emissivity values from at-sensor radiance. These calculated emissivity values are used for an iterative correction for reflected down-welling sky irradiance. A value of 0.99 would be assigned to begin with which represents a near-gray body such as water, snow and vegetation. If the NEM emissivity values have low contrast, the initial assumptions are likely to be correct and therefore an empirically based process is used for refining ε_{max}. On the other hand, if the NEM emissivity values have high contrast, this indicates that the surface is probably rock and/or soil. In this case, a lower value for ε_{max} would be assumed. The maximum emissivity values for all materials in the ASTER Spectral Library is in the range of 0.94 to 1.00, therefore a value of 0.96 could be a realistic estimate for those materials and can be assumed for processing.

As the processing in NEM module starts, the ground-emitted radiance is estimated by a simplified linear equation for each band (Eq.3.11). Temperatures of each band, T_b, are calculated by utilizing inverse Planck's function for ε_{max}, R_b and band wavelength, λ_b. The NEM temperature (T_{NEM}), to be used for calculations of band emissivity values, is the maximum temperature (T_b) estimated from the radiances (R_b) of different image bands (*b=10-14* for ASTER) (Eq.3.12).

$$R_b = L'_b - (1 - \varepsilon_{max})S_{\downarrow} \qquad \text{(Eq.3.11)}$$

where
R   *ground-emitted radiance;*
L'   *at-sensor radiance,*
$S_{\downarrow}$ *down-welling sky irradiance,*
b   *band number*

$$T_b = \frac{c_2}{\lambda_b}(\ln(\frac{c_1\varepsilon_{max}}{\pi R_b \lambda_b^5}+1))^{-1}, \quad T_{NEM} = \max(T_b) \qquad \text{(Eq.3.12)}$$

where
c_1 and c_2   *constants from Planck's Law;*
R   *ground-emitted radiance;*
λ   *band wavelength;*
b   *band number*

Once T_{NEM} is known, interim NEM emissivity values, $Ɛ_b$, are calculated based on equation (Eq.3.13). NEM emissivity values are used iteratively in order to re-estimate R for each band. Essentially, $Ɛ_b$ replaces $Ɛ_{max}$ in the equation and R_b values are re-calculated accordingly. This iterative analysis is repeated until the difference of R_b values are less than a desired threshold (t_2) or the number of iterations reaches a limited number (N). The default value for t_2 is the radiance equivalent to Noise Equivalent Delta Temperature (NEΔT) (0.05 W/m^2 sr μm) and N = 12 (Gillespie et al., 1998; Gillespie et al., 1999). As the iterative analysis ends the emissivity values, calculated from T_{NEM} and ground-emitted radiance values (R_b), are reported as final NEM emissivity values along with T_{NEM}.

$$\varepsilon_b = \frac{R_b}{B_{b(T_{NEM})}}$$ (Eq.3.13)

where
R	ground-emitted radiance;
B	black-body radiance,
T_{NEM}	down-welling sky irradiance,
b	band number

3.3.1.2. Ratio Module

The relative emissivity values ($β_b$) are calculated by normalizing the NEM emissivities of each band by the average emissivity of all bands (Eq.3.14)

$$\beta_b = \varepsilon_b * 5 * (\Sigma \varepsilon_b)^{-1} ;\qquad b\text{=10-14}$$ (Eq.3.14)

In general emissivity values for terrestrial surfaces are restricted to 0.7 <$Ɛ_b$ <1.0 (Prabhakara and Dalu, 1976); therefore the values of relative emissivity is restricted to 0.75 < βb <1.32. It is showed that emissivity band ratios are not affected by the errors in temperature estimation and this is also true for normalized β spectra i.e. relative emissivity values, $β_b$ (Watson et al., 1990 and Watson, 1992b).It is also stated that β spectrum does not preserve amplitude of the actual emissivities but, it does preserve the shape, on the contrary (Gillespie et al., 1999).

3.3.1.3. MMD Module

As mentioned in the previous section β spectrum in Ratio Module does not preserve the amplitude. In order to recover amplitude and therefore recover a refined temperature estimate the Maximum-Minimum Difference (MMD) is calculated and used to predict minimum emissivity ($\mathcal{E}_{min}$). In order to convert β_b into $\mathcal{E}_b$, $\mathcal{E}_{min}$ is predicted from MMD through an empirical relationship.

The first step of MMD module is to calculate the spectral contrast of the β spectrum through the equation (Eq.3.15). This calculated value of MMD is used to predict minimum emissivity to be used for calculation of TES emissivities through equations (Eq.3.16 and 3.17).

$$MMD = \max(\beta_b) - \min(\beta_b) ; b\text{=10-14}$$ (Eq.3.15)

$$\mathcal{E}_{min} = 0.994 - 0.687 * MMD^{0.737}$$ (Eq.3.16)

$$\mathcal{E}_b = \beta_b \left(\frac{\mathcal{E}_{min}}{\min(\beta_b)} \right) ; b\text{=10-14}$$ (Eq.3.17)

The actual emissivity contrast in a scene element is much greater than the apparent contrast. This error is due only to measurement errors. Apart from that MMD is claimed to be an unbiased estimate. On the other hand, MMD values of gray bodies are dominated by measurement errors and cannot be considered as unbiased. It is found that if MMD is smaller than a defined threshold (currently set to 0.032) $\mathcal{E}_{min}$ is not found from equation (Eq.3.16) but set to a constant value (0.983) appropriate for gray-bodies, such as vegetation and processing continues.

Thus far, the temperature is only calculated in the NEM module. It is stated that NEM temperature can have an error up to 3K (Gillespie et al., 1998; Gillespie et al., 1999). This error is due to the inaccuracy in assumption of $\mathcal{E}_{max}$ particularly for surface materials. Through recalculation of temperature using maximum TES emissivity values and atmospherically corrected radiances the inaccuracy in temperature values can be reduced (Eq.3.18).

$$T = \frac{C_2}{\lambda_{b*}} (\ln(\frac{\varepsilon_{b*}C_1}{R_{b*}\pi\lambda_{b*}} + 1))^{-1}$$

(Eq.3.18)

where
c_1 and c_2 *constants from Planck's Law;*
R   *ground-emitted radiance;*
λ   *band wavelength;*
b*   *band for which the emissivity is maximum*

3.3.1.4. Final Correction for Sky Irradiance and Bias in β

When it is compared TES values of temperature and emissivity are more accurate than that of NEM. The accuracy of temperature and emissivity can be improved through recalculation. In order to do so, maximum of TES emissivity values of each pixel is used as ε_{max} in NEM to make a single correction to at-sensor radiance for reflected down-welling sky irradiance in equation (Eq.3.11). Instead of NEM temperature, TES temperature is used along with new estimates of R. Then improved TES emissivity and temperature values are calculated following the same steps as explained above. Gillespie et al. (1998) and Gillespie et al. (1999) stated that if this process is repeated more than once there is a little gain observed. It is also stated that refined TES emissivity values changed as high as 0.01, therefore, this final correction is worth doing (Gillespie et al., 1998; Gillespie et al., 1999).

CHAPTER 4

DATA ANALYSES

In this chapter, detailed information regarding the data used and methods followed throughout the study is addressed. This chapter is roughly divided into two sections. The first section summarizes information about ASTER Multispectral Imaging System and preprocessing steps taken before the image analyses and the second section discusses the methods of the image analyses. The results of the image analyses will be provided separately in the following chapter.

4.1. ASTER Data Specifications

Advanced Spaceborne Thermal Emission and Reflection Radiometer (ASTER) is an advanced multispectral imager which is one of five remote sensory devices on board Terra satellite launched in December, 1999. The instrument had been collecting data with its entire 14 bands form surface of the Earth since February, 2000. However, starting in 2007 due to operational problems of SWIR detector cooler system the temperature of the detector started rising which caused degradation of the data quality. The ASTER SWIR data acquired since May 2008 are announced to have no good data quality with saturation of values and severe striping. According to the notice on ASTER Science web site on March 13th, 2010 SWIR detectors are providing data no more. It is also stated that if ASTER SWIR data are to be used, data acquired before April 2007 is recommended (ASTER GDS, 2010).

ASTER provides high spatial, spectral and radiometric resolution in Visible and Near Infrared (VNIR), Short Wave Infrared (SWIR) and Thermal Infrared (TIR) subsystems with 14 bands (Figure 4.1). The VNIR subsystem has 3 bands and it also includes an additional back-looking

near-infrared band which provides stereoscopic capability; the SWIR subsystem has 6 bands and TIR has 5 bands. The spatial resolution varies between the subsystems; 15m in VNIR, 30m in SWIR and 90m in TIR (Table 4.1). Regardless of the subsystem each ASTER scene covers an area of 60x60 km.

The Terra satellite system on which ASTER is boarded is a sun-synchronous satellite that follows a circular, near-polar orbit at an altitude of 705 km. The equatorial crossing of the satellite is at 10:30 a.m. local time and the satellite returns to the same orbit every 16 days (ASTER User's Handbook v2.0). A summary of the instrument can be found on Figure 4.2.
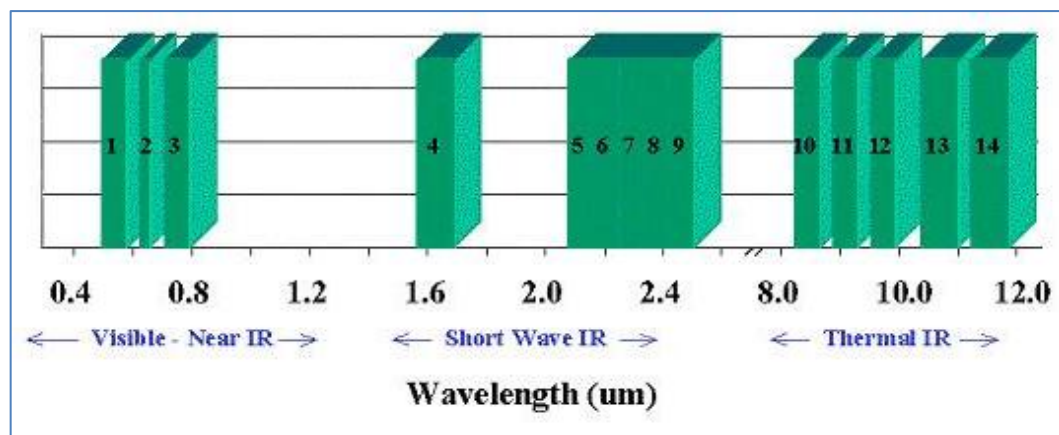
Figure 4.1 Distribution of ASTER bands on Electromagnetic Spectrum

Table 4.1 ASTER Product Description

	Data Field	Spectral Range [μm]	Units	Data Type	Valid Range	Spatial Resolution
VNIR	Band 1	0,52 - 0,60	W/(m²srμm)	8-bit unsigned integer	0 - 255	15m
	Band 2	0,63 - 0,69	W/(m²srμm)	8-bit unsigned integer	0 - 255	15m
	Band 3N	0,78 - 0,86	W/(m²srμm)	8-bit unsigned integer	0 - 255	15m
	Band 3B	0,78 - 0,86	W/(m²srμm)	8-bit unsigned integer	0 - 255	15m
SWIR	Band 4	1,600 - 1,700	W/(m²srμm)	8-bit unsigned integer	0 - 255	30m
	Band 5	2,145 - 2,185	W/(m²srμm)	8-bit unsigned integer	0 - 255	30m
	Band 6	2,185 - 2,225	W/(m²srμm)	8-bit unsigned integer	0 - 255	30m
	Band 7	2,235 - 2,285	W/(m²srμm)	8-bit unsigned integer	0 - 255	30m
	Band 8	2,295 - 2,365	W/(m²srμm)	8-bit unsigned integer	0 - 255	30m
	Band 9	2,360 - 2,430	W/(m²srμm)	8-bit unsigned integer	0 - 255	30m
TIR	Band 10	8,125 - 8,475	W/(m²srμm)	16-bit unsigned integer	0 - 65535	90m
	Band 11	8,475 - 8,825	W/(m²srμm)	16-bit unsigned integer	0 - 65535	90m
	Band 12	8,925 - 9,275	W/(m²srμm)	16-bit unsigned integer	0 - 65535	90m
	Band 13	10,25 - 10,95	W/(m²srμm)	16-bit unsigned integer	0 - 65535	90m
	Band 14	10,95 - 11,65	W/(m²srμm)	16-bit unsigned integer	0 - 65535	90m

Launch Date	18 December 1999 at Vandenberg Air Force Base, California, USA
Equator Crossing	10:30 AM (north to south)
Orbit	705 km altitude, sun synchronous
Orbit Inclination	98.3 degrees from the equator
Orbit Period	98.88 minutes
Grounding Track Repeat Cycle	16 days
Resolution	15 to 90 meters

Instrument	VNIR	SWIR	TIR
Bands	1-3	4-9	10-14
Spatial Resolution	15m	30m	90m
Swath Width	60km	60km	60km
Cross Track Pointing	± 318km (± 24 deg)	± 116km (± 8.55 deg)	± 116km (± 8.55 deg)
Quantisation (bits)	8	8	12

Figure 4.2 Summary of ASTER Instrument

Throughout the study ASTER image with granule ID of AST3A1 0211170839210603310605 is utilized. ASTER Level-3 data is the orthorectified image product which includes Level-1B radiometrically and geometrically calibrated radiance for every bands including Band3B. Note that an orthorectified image is similar to a map with near-vertical views in every location. Therefore no further geometric correction has been done. Detailed information about the ASTER image utilized can be found in Table 4.2.

Table 4.2 Detailed information on the ASTER image used

Granule ID	AST3A1 0211170839210603310605
Processing Level	3
Acquisition Date	Nov 17, 2002
Source Data Product	ASTL1A 0211170839210212050221
Scene Center	40.626988, 34.101804
Scene Upper Left	40.954567, 33.656972
Scene Upper Right	40.945966, 34.553932
Scene Lower Right	40.297682, 34.538977
Scene Lower Left	40.306090, 33.650647
Solar Direction	166.626389, 29.409205
Map Projection	Universal Transverse Mercator
Ellipsoid and Datum	WGS 84, WGS 84
UTM Zone	36 N

4.1.1. Preprocessing

ASTER image requires preprocessing prior to the image analyses. This procedure comprises calibration of ASTER VNIR, SWIR and TIR bands; recalibration of ASTER TIR bands; preparation of Normalized Difference Vegetation Index (NDVI) and vegetation mask; and resampling of ASTER SWIR bands along with vegetation masks (Figure 4.3). The steps of the preprocessing are discussed below.
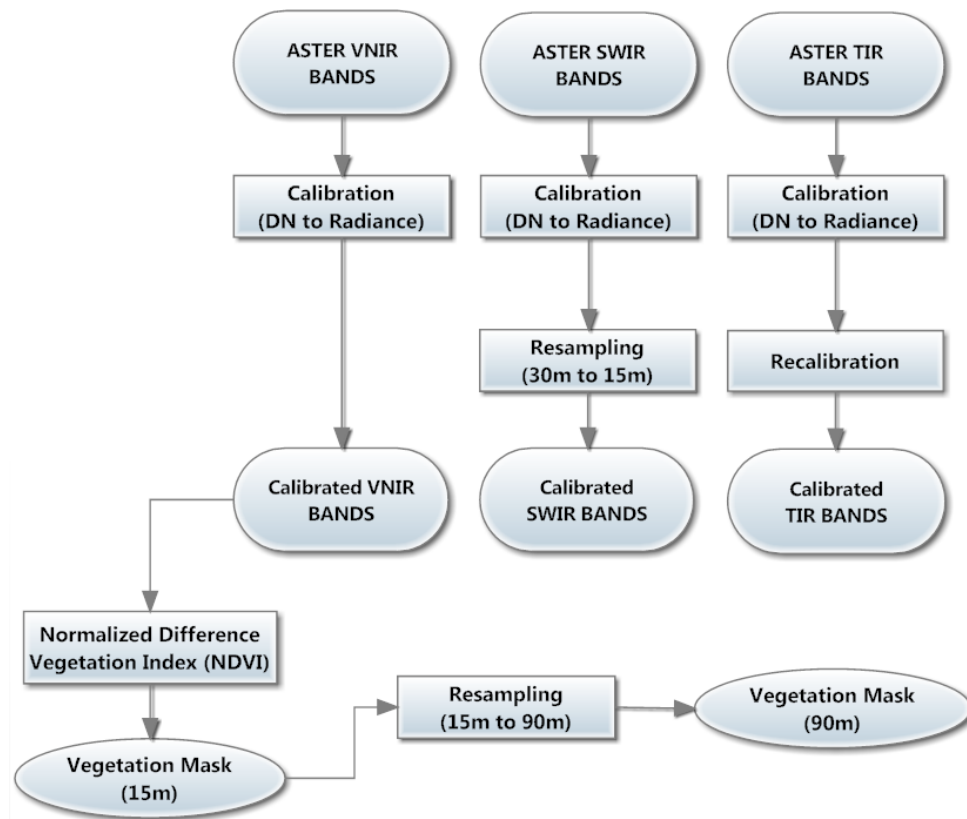
Figure 4.3 The flowchart of the ASTER image preprocessing

4.1.1.1. Calibration of ASTER VNIR, SWIR and TIR Images

Calibration consists of converting the raw "digital number" values recorded by the sensor into at-sensor radiance which better represents the surface features. In order to convert the raw data a standard unit conversion method is used (Smith, 2012; Yüksel et al., 2008). This standard unit conversion method corrects the raw digital number for sensor gain and offset by applying the following equation.

$$L' = (DN - 1) * UCC \qquad\qquad (Eq.4.1)$$

where
L'   at-sensor radiance,
DN   digital number in the original ASTER image;
UCC   unit conversion coefficient

Note that unit conversion coefficients are dependent not only on the band of ASTER image but also on the gain setting of the band which was used in image acquisition. In order to figure out gain and offset setting of the bands in an ASTER image metadata file accompanies the raster should be consulted. Detailed information regarding the unit conversion coefficients can be found in Table 4.3.

Table 4.3 The Unit Conversion Coefficient of each ASTER bands

	Band Number	Coefficient [W/(m^2 sr μm)]			
		High Gain	Normal Gain	Low Gain 1	Low Gain 2
VNIR	1	0,6760	1,6880	2,2500	N/A
	2	0,7080	1,4150	1,8900	
	3N	0,4230	0,8620	1,1500	
	3B	0,4230	0,8620	1,1500	
SWIR	4	0,1087	0,2174	0,2900	0,2900
	5	0,0348	0,6960	0,0925	0,4090
	6	0,0313	0,0625	0,0830	0,3900
	7	0,0299	0,0597	0,0795	0,3320
	8	0,0209	0,0417	0,0556	0,2450
	9	0,0159	0,0318	0,0424	0,2650
TIR	10	N/A	0,006882	N/A	N/A
	11		0,00678		
	12		0,00659		
	13		0,005693		
	14		0,005225		

4.1.1.2. Recalibration of ASTER TIR Images

It is also known that ASTER TIR products processed before Feb 8, 2006 include an error due to delay in Radiometric Calibration Coefficient (RCC) updating. It is also stated that error is reduced for RCC version 2.09 or later, the products observed after October 2002. However, for the RCC versions before 2.09 the error is large. Therefore, TIR images processed before the date stated requires recalibration before any further analysis. Recalibration coefficients can be obtained online from Tonooka Laboratory at Ibaraki University, Japan (Tonooka, 2012). It only requires observation date (UTC) and the RCC version of the image both of which can be found in metadata file. These recalibration coefficients generated by a modified version of Tonooka's method (Tonooka et al., 2003; Sakuma et al., 2005) can be used for Level-1A, 1B and 3A. Along with the coefficients estimated calibrated errors are also provided. The Tonooka's modified method follows a linear approach based on Eq.4.2.

$$\mathrm{Re}\,calibrated\_Radiance = (A * Original\_Radiance) + B \qquad \text{(Eq.4.2)}$$

where
Original_Radiance   *calibrated at-sensor radiance*
A   *first constant of RCC,*
B   *second constant of RCC*

4.1.1.3. Preparation of NDVI Mask

For image analysis of the satellite data it is necessary to reduce or remove irrelevant data such as water bodies and vegetation not only for ease of the analysis but also for the accuracy of the analysis especially that uses global statistics like PCA. Since the main focus of this study is on lithology i.e. rock units; vegetation and/or water bodies should be masked. On the image utilized for this study it is visually observed that no significant water body is present therefore the only irrelevant data is the vegetation. Vegetated pixels on the image can be identified using Normalized Difference Vegetation Index (NDVI) which uses NIR and RED wavelength responses. Essentially, vegetation is expected to show high NIR response along with low RED (Eq. 4.3.)

$$\frac{NIR - RED}{NIR + RED} = \frac{Band\,3N - Band\,2}{Band\,3N + Band\,2} \qquad \text{(Eq.4.3)}$$

4.1.1.4. Resampling

As mentioned in the data specifications part ASTER VNIR, SWIR and TIR subsystems have different spatial resolutions; 15m, 30m and 90m respectively. For VNIR and SWIR subsystems to be utilized together in the image analyses the spatial resolutions should be the same which requires resampling. Rather than down-sampling VNIR data (15m) to SWIR resolution (30m) which reduces the level of detail up-sampling SWIR data (30m) to VNIR resolution which practically does not change the level of detail, has been preferred. All the SWIR bands (Band 4-9) resampled according to affine model and nearest neighbor resampling method to 15m where VNIR Band1 is used to match reference and ensure the pixels are superimposed correctly. Since the NDVI mask already has 15m spatial resolution no resampling is required and can be utilized in the image analyses along with VNIR and resampled SWIR data. On the other hand, for TIR, NDVI mask requires resampling in order to match the spatial resolution of TIR (90m). Same parameters are used for resampling (affine model and nearest neighbor method while TIR Band10 is used to match reference and pixel superimposition).

4.2. Image Analyses

Image analyses include two of the most widespread methods used for lithological mapping; Principle Component Analysis (PCA) and Decorrelation Stretch that covers ASTER VNIR and SWIR bands. Additionally, Temperature-Emissivity Separation technique is used for ASTER TIR bands, in order to recover the band emissivities of surface materials for lithological discrimination. Along with the methods mentioned above the spectral indices based on the band ratios specified in the literature are also used (Figure 4.4).
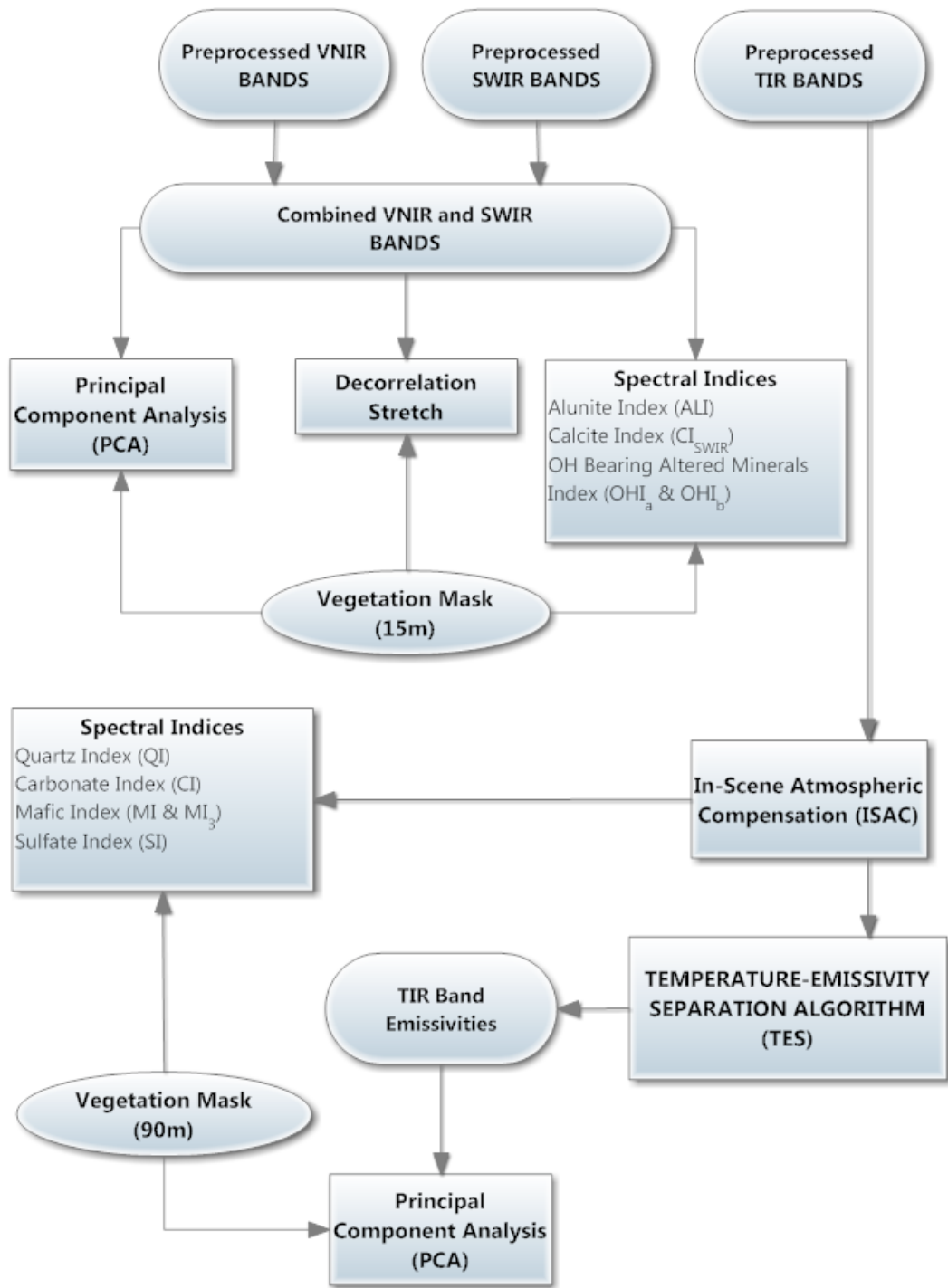
Figure 4.4 The flowchart of image analyses

4.2.1. Principal Component Analysis (PCA)

Principal Component Analysis (PCA), also known as principal-component transformation or Karhunen-Loeve transformation was first introduced by Pearson (1901). This statistical approach is basically a mathematical procedure that utilizes an orthogonal linear transformation through which observations of possibly correlated variables are converted into linearly uncorrelated variables (principal components). The idea behind this approach is to compress multispectral data sets by calculating a new different coordinate system (Sabins, 1987). Through principal component analysis the dimensionality of the data set is reduced such that the number of principal components is less than or equal to the number of original variables. The transformation is defined such a way that the first principal component accounts for as much of the variability in the data as possible. In other words, the first principal component has the largest possible variance.

Solar illumination and albedo effects at the surface govern the variation of radiant flux measured by a sensor. Spectral reflectance features of surface minerals have a very little effect of this variation (Öztan, 2008). Sabine (1999) stated that through principal component analysis irradiance effects that dominate the sensor bands can be suppressed and therefore the spectral reflectance features of surface materials can be examined. Yamaguchi and Naito (2003) stated that color composite of major principal components may enhance the visual interpretation for surface material discrimination and mapping.

4.2.2. Decorrelation Stretch

Soha and Schwartz (1978), was the first to introduce decorrelation stretch through improving the work Taylor (1973) had done earlier. The technique relies upon a principal component transformation of the original data. In general the resultant images of the transformation are stretched according to statistical distribution of the values in order to increase the contrast and remove the correlation. Then these images are assigned to primary colors to be displayed in RGB color composite. The essential difference of decorrelation stretch is that following the enhancement of contrast through transformation statistically independent principal components are retransformed into their original coordinates. Therefore the distortion due to enhancement in perceived color would be minimal (Gillespie et al., 1986).

As mentioned before principal component transformation removes the correlation between the multispectral images and therefore reduces the dimensionality of the multispectral images. The main problem with principal component transformation is that the color assignments are arbitrary and not related to any physical property. Taylor (1973) stated that once the multi spectral data is decorrelated through rotation of the coordinate system and the variances equalized in the new coordinate space, additional rotations of the coordinate system would not introduce any correlation. Soha and Schwartz (1978) proposed that the most suitable rotation for remotely sensed image interpretation is a simple inverse rotation of the image to the original color space. This technique then named "decorrelation stretch" technique although principal component transformation also produce uncorrelated images.

4.2.3. Spectral Indices

Spectral index approach is similar to that of PCA such that both of the techniques use orthogonal transformation of multispectral data. The essential difference between two methods is the determination of the transform axes. In PCA the axes are determined mathematically in order to maximize the variance of the multispectral data. On the other hand, in spectral index method the transform axes is determined in order to represent a specific pattern. Additionally, through PCA dimensionality of the multispectral data is reduced. In general PCA enhances contrast between surface materials that helps in visual interpretation and discrimination. The transformed results however do not include a physical meaning as the color composite is selected arbitrarily. On the other hand, spectral indices use pre-defined coefficients and therefore make it possible to know the physical meaning of the transformed results to some degree (Crist and Cicone, 1984). Yamaguchi and Naito (2003) stated that spectral indices for surface material discrimination make the resultant spectral index images easy to interpret in geological point of view.

Different researchers calculated several indices for surface material discrimination based on ASTER SWIR and TIR data. Yamaguchi and Naito (2003) defined alunite, kaolinite, calcite and brightness indices for SWIR data; Ninomiya (2004) defined calcite index, OH bearing altered mineral index and alunite index. For TIR, on the other hand, Ninomiya (2002) and Ninomiya and Fu (2002) defined quartz, carbonate and mafic indices. Additionally, for TIR, Öztan and Süzen (2011) proposed sulfate index for evaporate mineral mapping. The approaches of the

researchers to spectral indices are quite different. For instance, the quartz, carbonate and mafic indices defined by Ninomiya (2002) and Ninomiya and Fu (2002) utilize spectral radiance values of TIR bands; sulfate index defined by Öztan and Süzen (2011) also utilizes spectral radiance values of TIR bands; calcite, OH bearing altered mineral and alunite indices defined by Ninomiya (2004) utilizes spectral radiance values of SWIR bands while brightness, alunite, kaolinite, calcite and montmorillonite indices defined by Yamaguchi and Naito (2003) utilize surface reflectance values of SWIR bands.

4.2.4. Temperature – Emissivity Separation

In this study, essentially, TES algorithm approach as discussed previously is followed (Figure 4.5). Some modifications, however, has been applied for convenience of the analysis. These modifications are explained in detail below
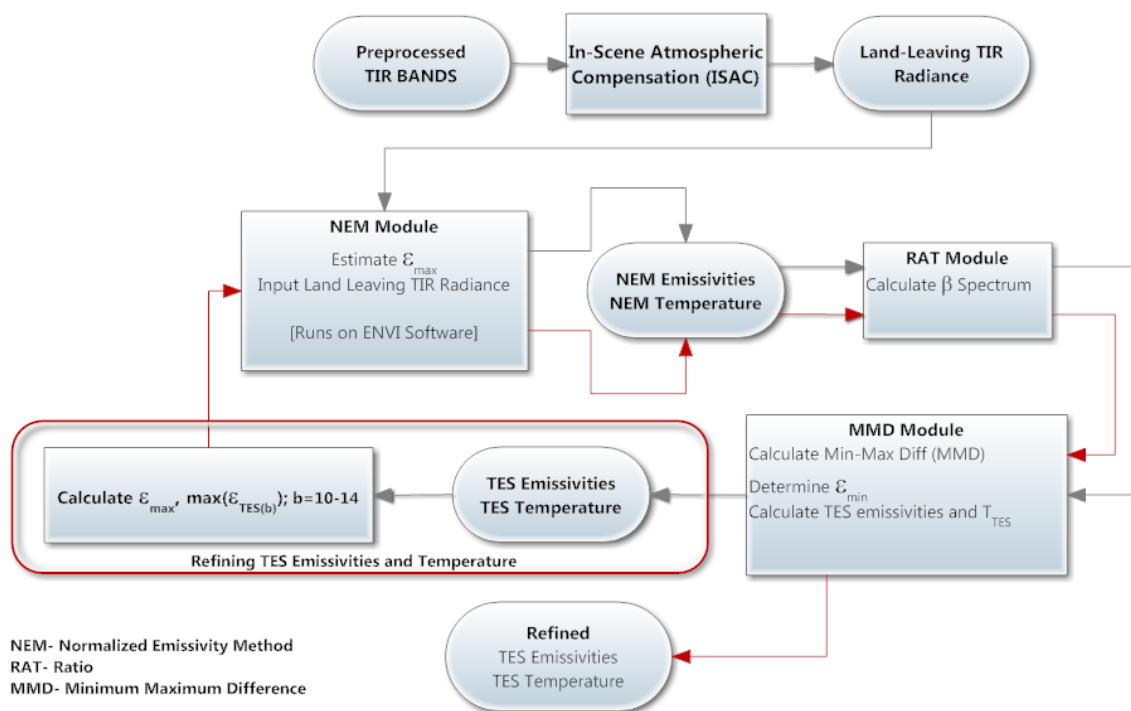
Figure 4.5 Temperature- Emissivity separation flowchart

Essentially, atmospheric correction in TES algorithm is applied in NEM module. The reflected down-welling sky irradiance is utilized along with the at-sensor radiance and its effect is removed iteratively. The result of the iterative analysis is considered being land-leaving radiance. In this study, however, instead of the iterative approach explained in the algorithm description, In-scene Atmospheric Compensation (ISAC) method was used. The atmospheric compensation generates land-leaving radiance which can be further utilized in temperature-emissivity separation algorithms (DiStasio and Resmini, 2010). The

The In-Scene Atmospheric Compensation (ISAC) algorithm uses only remotely-sensed at-sensor radiance data. Basically, the algorithm captures true state of the atmosphere along with the occurring radiative processes at the time of the data collection. The algorithm requires identification and estimation of input parameters along with the input radiance data correctly which is the main difficulty of the algorithm. The main convenience regarding the algorithm, on the other hand, is that radiative transfer model is not needed for the correction. The ISAC algorithm was described by Young et al. (2002). As explained briefly in DiStasio and Resmini (2010) ISAC uses the brightness temperature of each pixel for land-leaving radiance estimation. Then a scatter plot is generated for each band between the observed radiance and result of the Planck function. A straight line is fit to the top of the scatter plot which corresponds to the pixels having emissivity closest to 1. From this fit atmospheric transmission and upwelling path radiance are estimated. These parameters are used to estimate land-leaving radiance for each pixel.

ENVI (Environment for Visualizing Images) software includes a version of ISAC implemented as "*Thermal Atm Correction*". Therefore, in this study, the atmospheric compensation needed before TES algorithm was conducted in ENVI Software. ISAC as implemented in ENVI is considered to be a robust, effective, convenient atmospheric compensation tool for TIR for remote sensing user community (DiStasio and Resmini, 2010).

In-Scene atmospheric compensation in ENVI estimated the land-leaving radiance at once. Therefore, atmospherically compensated radiances were directly utilized in order to calculate NEM temperature and emissivities. ENVI software also includes an implementation of Normalized Emissivity Method (NEM). An emissivity value (0.96) which roughly represents the

37

terrestrial materials is selected as initial emissivity. The output batch from ENVI includes five emissivity layers (one for each ASTER TIR band) and one temperature layer.

Essentially, no modification has been done in the ratio or in MMD modules. In ratio module, through ratioing the NEM emissivities to their average the relative emissivities (β_b) were calculated on TNTmips. Then the relative values of emissivities were scaled to their actual values in MMD module. The output batch of the MMD module comprises band emissivities and temperature.

Although the temperature is not the main concern of this study, since the TES temperature will be used for recalculation of TES emissivity and temperature in order to improve the accuracy further TES temperatures were calculated as described in Section 3.3.1.4. Atmospherically compensated radiance values were used along with TES emissivities and temperature for calculation of new NEM emissivities to be used in ratio module. From this point on the calculations were the same as described before. The outputs of MMD module are the final refined TES temperature and band emissivities.

CHAPTER 5

RESULTS

In this chapter the results of the data analyses is presented. This includes the preprocessing, principal component analysis, decorrelation stretch, spectral indices and temperature-emissivity separation. The resultant images are interpreted visually from the RGB color composites. On the other hand, some of the resultant images such as the spectral indices are displayed gray-scale single image.

The image processing and enhancements are conducted mainly conducted in MicroImages TNTmips software and for mapping purposes ESRI ArcGIS 9.3 is used.

5.1. Preprocessing

As mentioned earlier ASTER L3 data need preprocessing in order to be utilized in the image analyses. In other words, raw digital numbers need to be converted into meaningful radiance values. In order to perform this operation, first, gain and offset setting of the ASTER data is identified through consulting the metadata file. It is found that in VNIR only Band 1 and Band 2 have "High Gain" settings while Band 3N and Band 3B have "Normal Gain" settings. For SWIR and TIR all the bands have "Normal Gain" settings. Then, unit conversion coefficients (UCC) are selected for all 14 ASTER bands accordingly. Unit Conversion Coefficients for ASTER bands and detailed information about the process can be found in Chapter 4 (*Section 4.1.1*). Following the calibration of the ASTER bands, TIR bands go through recalibration in order to compensate the delay in radiometric calibration coefficient (RCC) updating. As explained before, (*Section 4.1.1.2*) the recalibration coefficients obtained online from Tonooka Laboratory at Ibaraki University,

Japan web site based on the RCC version and the date of the acquisition (UTC) both of which is obtained through metadata file. Detailed information regarding the coefficients and estimated errors of radiance and temperature are presented in the following table (Table 5.1)

Table 5.1 ASTER TIR Recalibration coefficients used and estimated errors

Band	A	B	Estimated Changes (Upper: Radiance, Lower: Temperature)			
			@ 270 K	@ 300 K	@ 320 K	@ 340 K
10	1,008392	-0,0414	-0,000	+0,037	+0,072	+0,115
			-0,00 K	+0,20 K	+0,31 K	+0,41 K
11	1,016543	-0,0861	+0,000	+0,074	+0,140	+0,222
			+0,00 K	+0,41 K	+0,62 K	+0,82 K
12	1,029099	-0,1595	+0,000	+0,128	+0,240	+0,377
			+0,00 K	+0,73 K	+1,12 K	+1,47 K
13	1,014767	0,0867	-0,000	+0,057	+0,105	+0,161
			-0,00 K	+0,39 K	+0,61 K	+0,81 K
14	1,018525	-0,1082	+0,000	+0,066	+0,120	+0,182
			+0,00 K	+0,49 K	+0,77 K	+1,03 K

Preliminary visual interpretations of the data are performed on the RGB color composites of preprocessed ASTER VNIR and SWIR bands. Obviously, the first color composite image is the false color composite using VNIR bands (RGB: 3N, 2, 1) (Figure 5.1). Following the false color composite of VNIR band, two additional color composites using SWIR and VNIR bands are also produced. The first color composite is produced through utilizing only SWIR bands (RGB: 9, 6, 4) (Figure 5.2) and the second color composite is produced through utilizing two SWIR bands along with one VNIR band (RGB: 9, 4, 1) (Figure 5.3). In order to use VNIR and SWIR data in the same color composite the spatial resolutions need to be the same. Therefore, before producing any color composite out of VNIR and SWIR bands, SWIR bands are resampled to same resolution as the VNIR bands which have 15m spatial resolution. Note that the color composites produced using SWIR bands pursue a goal to visualize the response of surface materials in SWIR that is not visible to human eye. Essentially, this response is related to the chemical properties of the material and not related with the physical properties of the materials such as color.
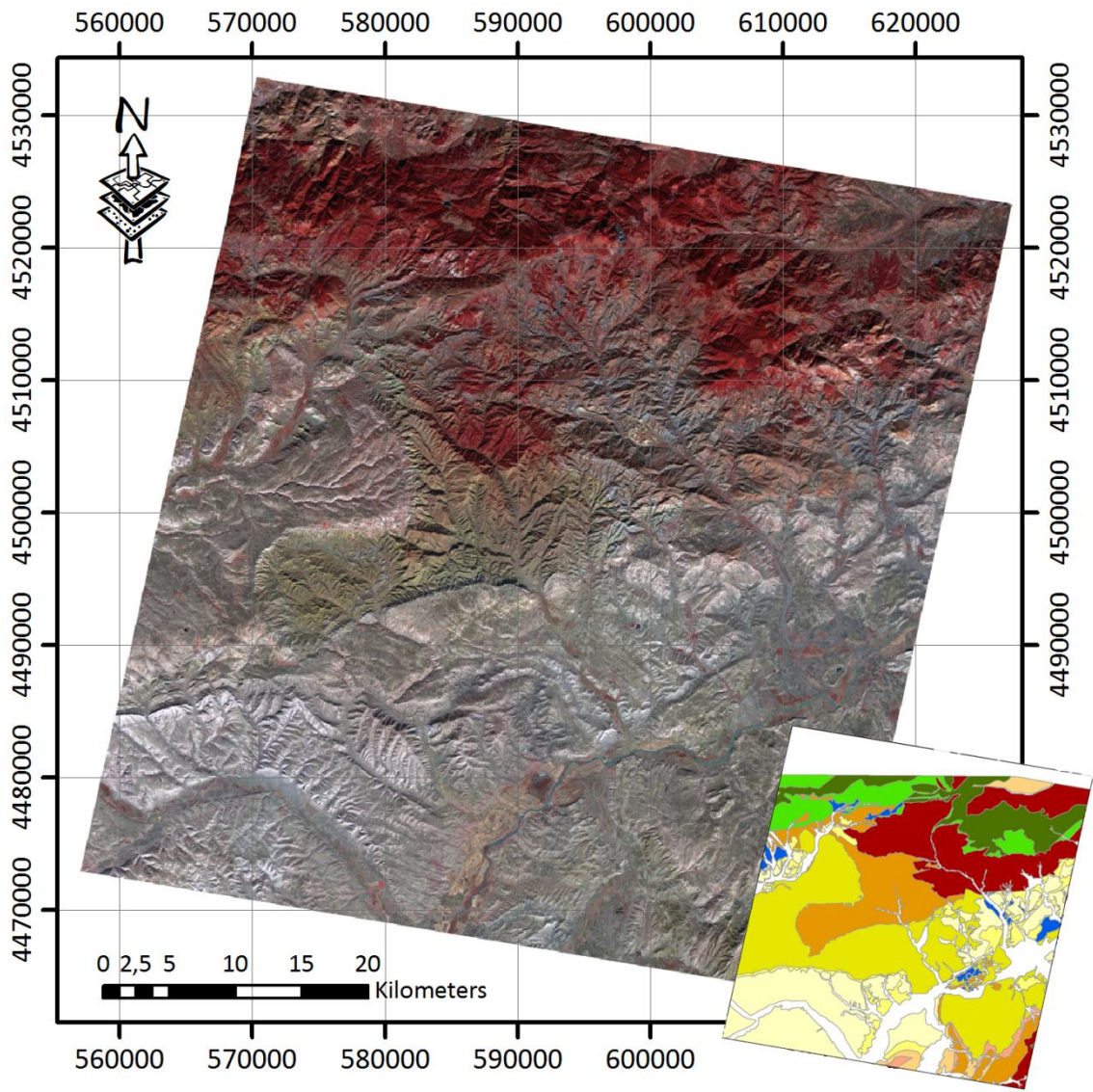
Figure 5.1 RGB false color composite of ASTER VNIR Bands (R: Band-3N, G: Band-2, B: Band-1). *See Figure 2.2 for legend of the inset map.*
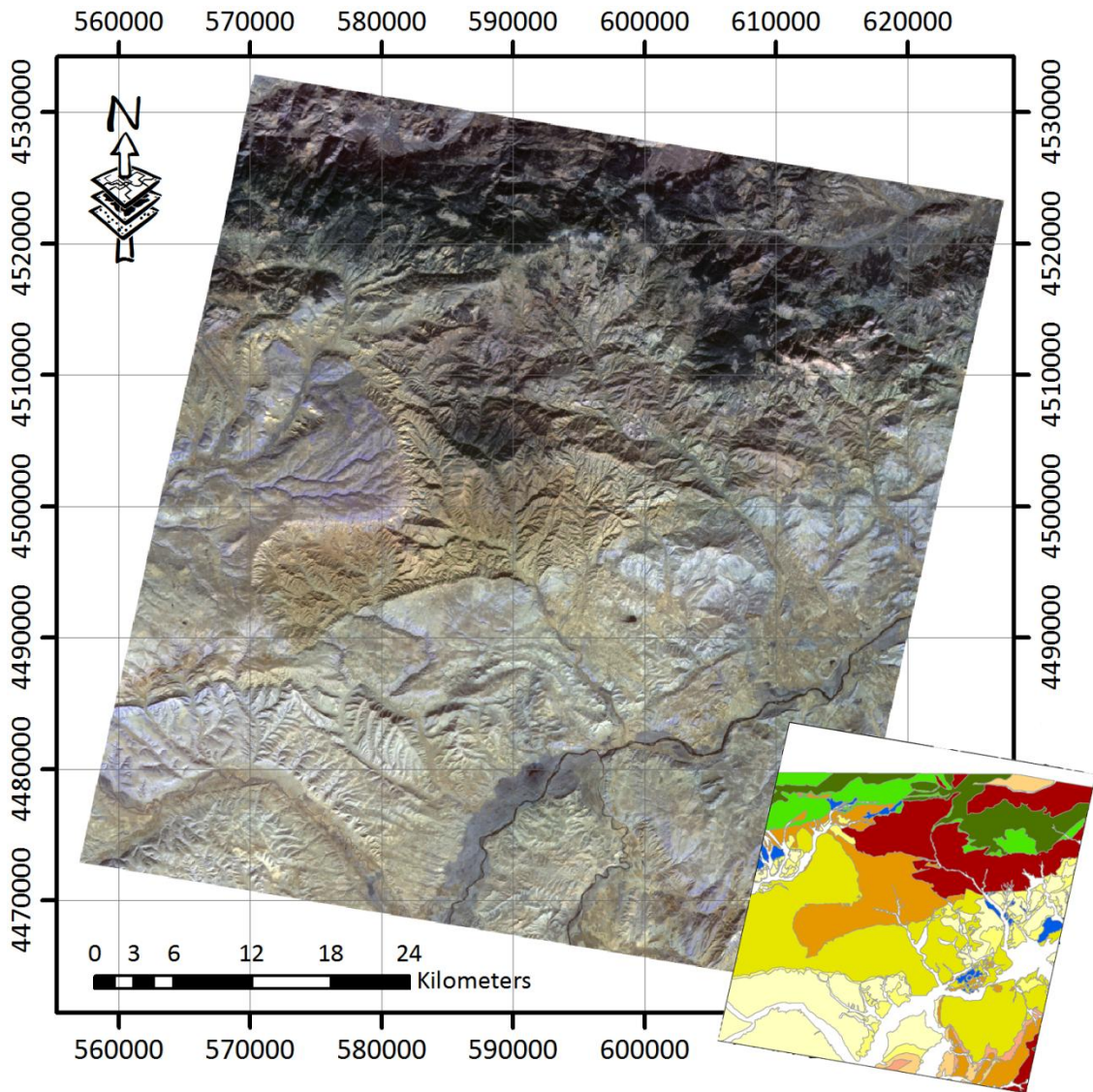
Figure 5.2 RGB color composite of ASTER SWIR Bands (R: Band-9, G: Band-6, B: Band-4). *See Figure 2.2 for legend of the inset map.*
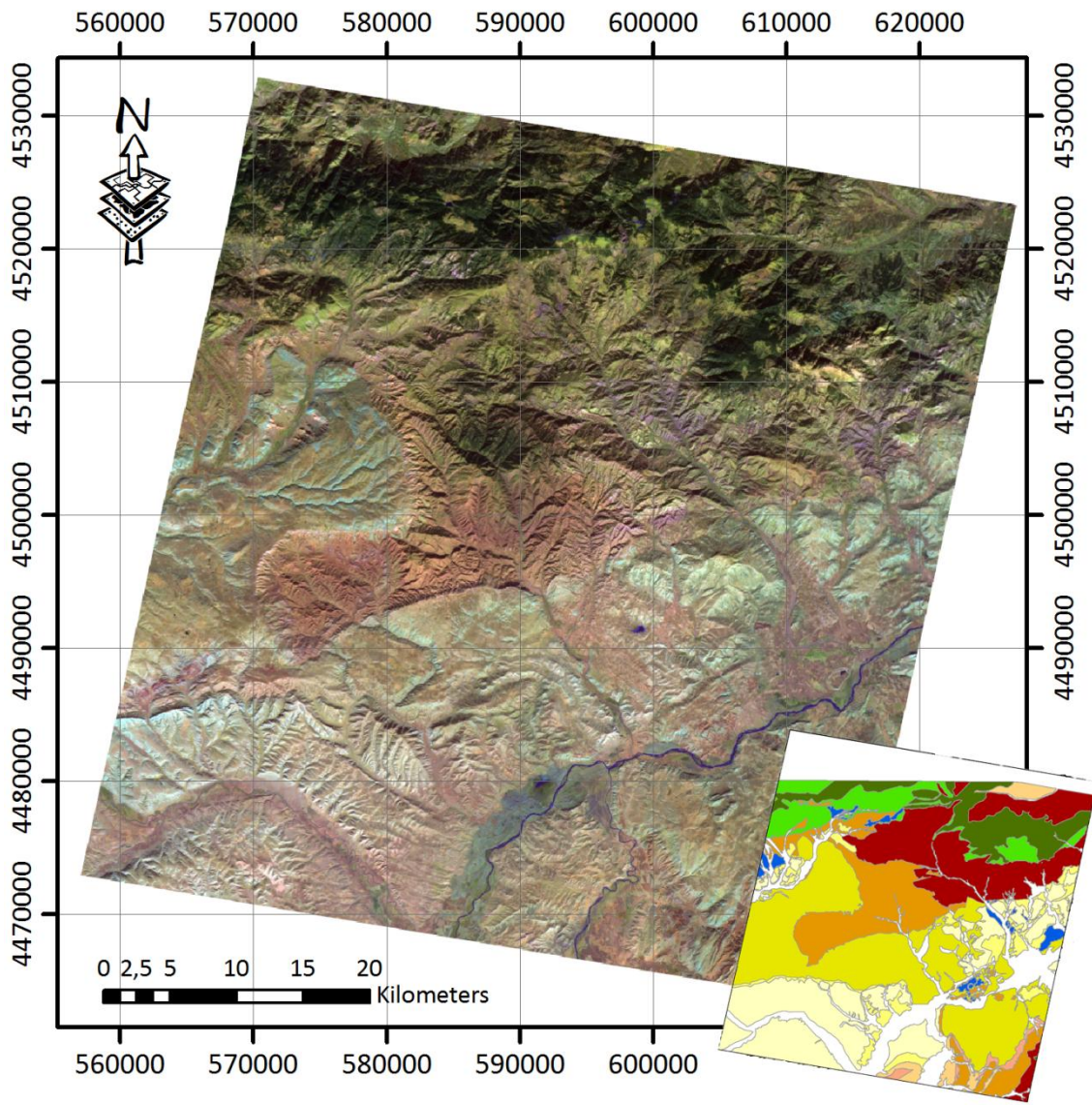
Figure 5.3 RGB color composite of ASTER SWIR Bands and a visible band (R: Band-9, G: Band-4, B: Band-1). *See Figure 2.2 for legend of the inset map.*

Preprocessing also includes the preparation of Normalized Vegetation Index (NDVI) to be used for vegetation masking. The NDVI image is produced using ASTER bands 2 and 3N as explained before where Band 2 represents red wavelength and Band 3N represents near-infrared wavelength at nadir (Figure 5.4). In the red wavelength vegetation is expected to show low response while in the near-infrared wavelength high response. Therefore, as the density of the vegetation increases the NDVI also known as the greenness index also increases. As the name implies vegetation response is normalized in a range between -1 and 1 for the sake of comparison. However, there is no absolute global threshold for NDVI. In other words, there is no absolute value that gives the vegetation in the image. Through combination of values of NDVI and visual interpretation on the false color composite a local threshold is defined as 0.21 for this study.

NDVI mask is used for masking VNIR, SWIR and TIR data separately. Since the NDVI is produced using VNIR bands, the spatial resolution of the NDVI exactly matches the resolution of resampled SWIR bands and VNIR bands (Figure 5.5). On other hand, for TIR bands, NDVI needs to be resampled in order to match the spatial resolution of 90m. Therefore, produced NDVI is resampled to match the spatial resolution of TIR bands.

Moreover, due to the parallax error in ASTER SWIR bands the extents of the bands in SWIR are not the same. For analysis such as principal component analysis and decorrelation stretch the extents of the input data need to be the same along with the size of the pixel. Therefore, VNIR, SWIR bands and NDVI mask for 15m are clipped according to the SWIR band that has the minimum extent. Even though there is no parallax error in TIR due to resampling the extent of the TIR bands and NDVI mask for 90m do not match therefore NDVI mask for 90 m is also clipped for perfect match with TIR bands.
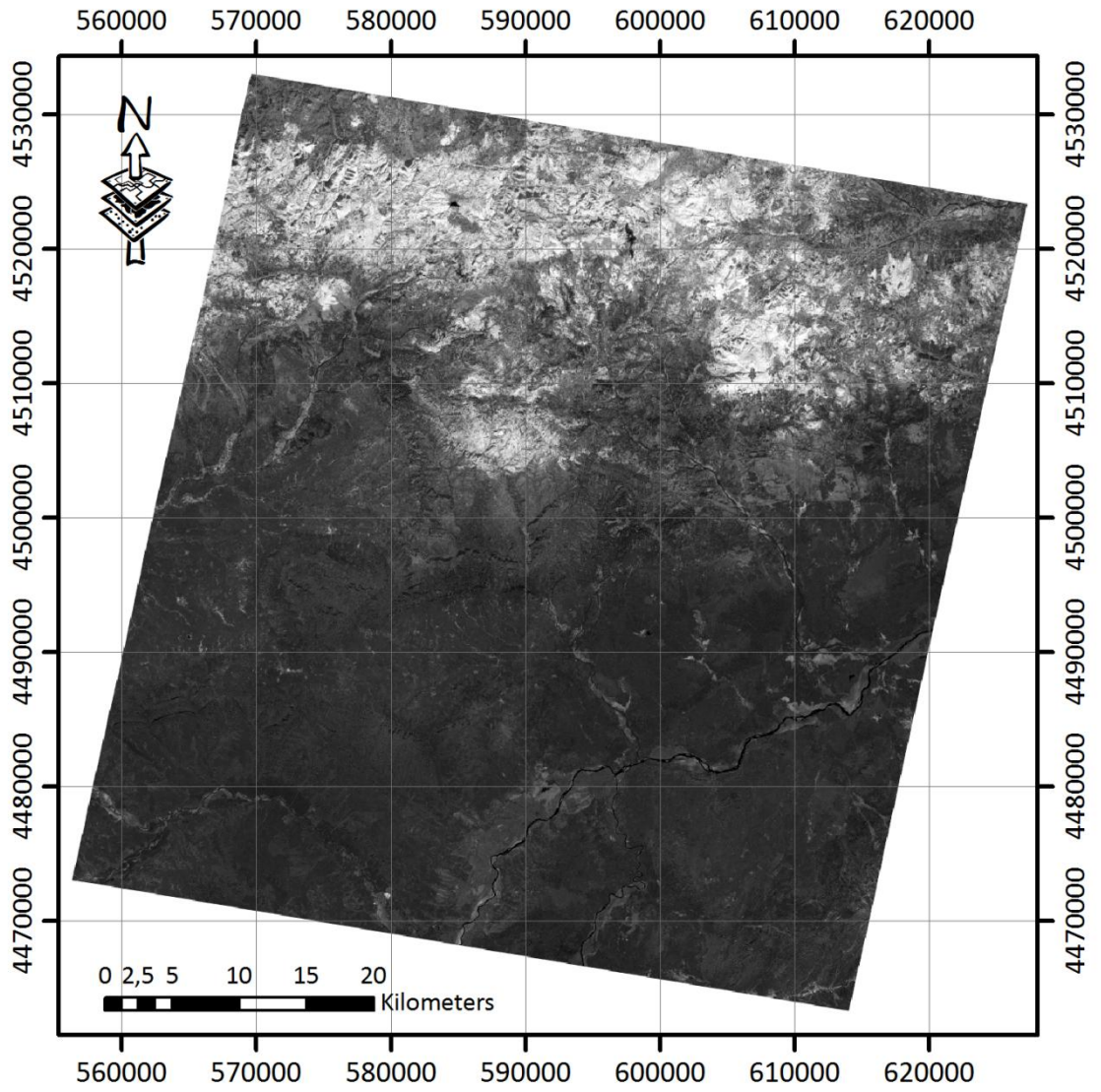
Figure 5.4 Normalized Difference Vegetation Index (NDVI)
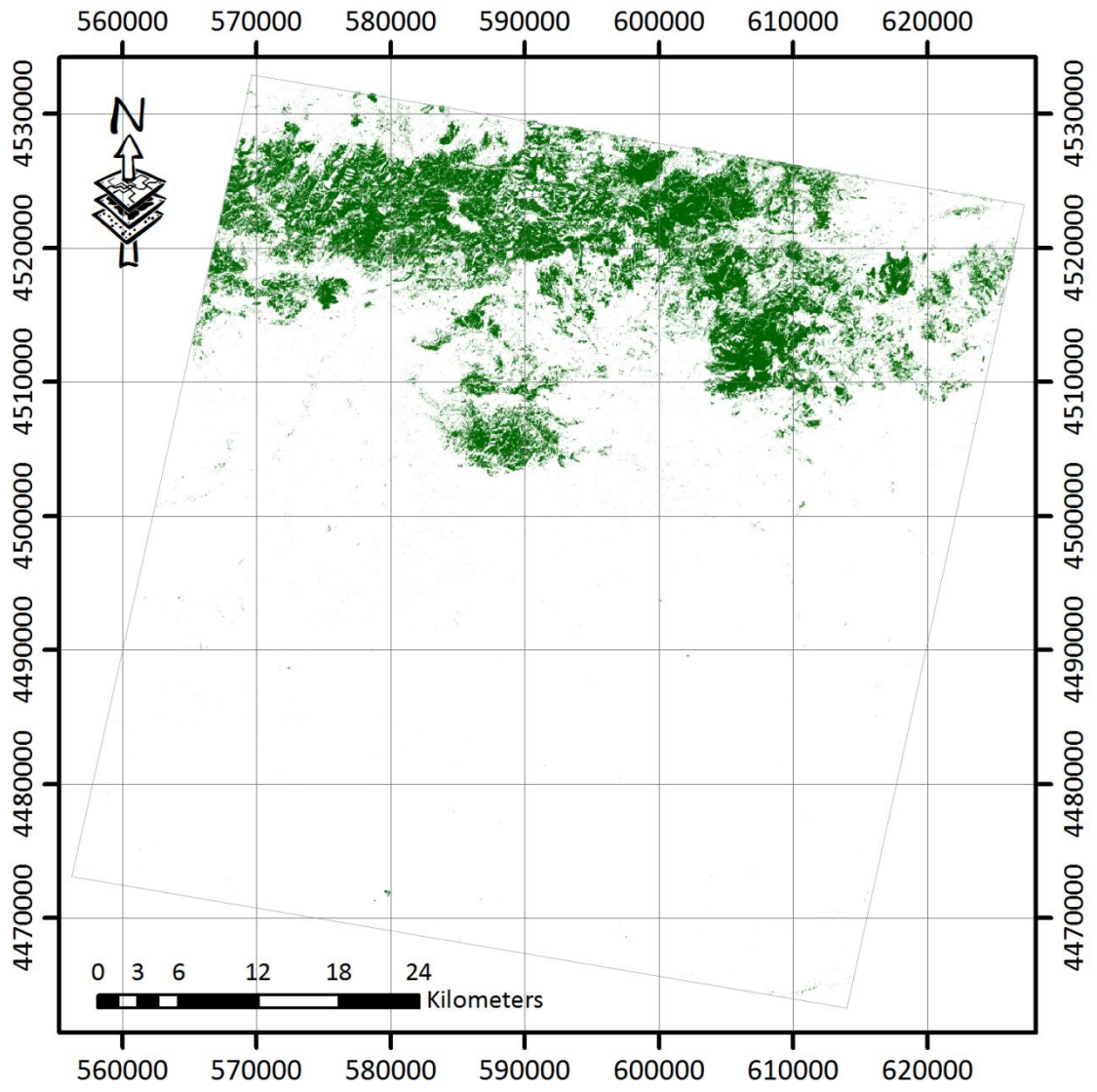
Figure 5.5 Vegetation mask prepared for 15m spatial resolution. *Note that the green area on the figure represents the vegetation*.

5.2. Principal Component Analysis

The principal component analysis is conducted in MicroImages TNTmips software for preprocessed ASTER VNIR and SWIR bands (Bands 1-9). NDVI mask is used to mask out vegetation for higher accuracy as the vegetation is out of concern in the first place. Therefore, the values of vegetated pixels are not included in statistical analysis. The resulting principal components are displayed in RGB color composites for better visualization and interpretation. The transformation parameters are provided as an output of the software and presented accordingly.

The PCA is conducted for VNIR and SWIR bands of ASTER (Bands 1-9). As explained previously, the bands used for the analysis are the preprocessed ASTER bands and clipped in order to match the extent of all the input layers. The transformation parameter of the PCA is depicted in Tables 5.2 and 5.3. The results of the principal component analysis − namely the principal components − are visualized in RGB color composites. For the first RGB color composite, the first three principal components are selected (RGB: PC1, PC2, PC3) which represents around 99.5% of the data (Figure 5.6).

Additional RGB color composites are also produced for comparison and better visual interpretation. The second color composite produced includes PC1, PC3 and PC5 triplet (RGB: PC1, PC3, PC5) (Figure 5.7). This composite represents 96% of whole data; because PC1 represents 95% of the data by itself while other principal component bands contain 1% extra information. The RGB color composite produced from PC2, PC3 and PC4 (RGB: PC2, PC3, PC4) represents only 5% of the whole data (Figure 5.8) and the RGB color composite produced from PC2, PC4 and PC6 (RGB: PC2, PC4, PC6) represents only 4% of the data (Figure 5.9). By these produced color composites using different combinations of principal component bands, whole data is analyzed and compared visually.

Table 5.2 Parameters of PCA of ASTER VNIR and SWIR bands

MEAN RASTER VALUES	
RASTER	MEAN
BAND1	39,8
BAND2	33,0
BAND3N	31,6
BAND4	8,3
BAND5	2,4
BAND6	2,2
BAND7	1,8
BAND8	1,3
BAND9	0,9

VARIANCE/COVARIANCE MATRIX								
RASTER	BAND1	BAND2	BAND3N	BAND4	BAND5	BAND6	BAND7	BAND8	BAND9
BAND1	102,7988	102,5739	76,7259	22,0241	5,5488	5,5410	4,6278	3,2979	2,0080
BAND2	102,5739	109,7970	82,1563	22,9383	5,8134	5,8509	4,8803	3,5012	2,1459
BAND3N	76,7259	82,1563	75,1384	18,5381	4,3363	4,5035	3,6702	2,6552	1,6365
BAND4	22,0241	22,9383	18,5381	6,0673	1,4664	1,4882	1,2177	0,8708	0,5356
BAND5	5,5488	5,8134	4,3363	1,4664	0,3989	0,3946	0,3245	0,2317	0,1443
BAND6	5,5410	5,8509	4,5035	1,4882	0,3946	0,4080	0,3273	0,2343	0,1461
BAND7	4,6278	4,8803	3,6702	1,2177	0,3245	0,3273	0,2799	0,1969	0,1215
BAND8	3,2979	3,5012	2,6552	0,8708	0,2317	0,2343	0,1969	0,1438	0,0878
BAND9	2,0080	2,1459	1,6365	0,5356	0,1443	0,1461	0,1215	0,0878	0,0565

CORRELATION MATRIX								
RASTER	BAND1	BAND2	BAND3N	BAND4	BAND5	BAND6	BAND7	BAND8	BAND9
BAND1	1,0000	0,9655	0,8730	0,8819	0,8665	0,8556	0,8627	0,8578	0,8329
BAND2	0,9655	1,0000	0,9045	0,8887	0,8784	0,8742	0,8803	0,8812	0,8612
BAND3N	0,8730	0,9045	1,0000	0,8682	0,7920	0,8134	0,8003	0,8078	0,7939
BAND4	0,8819	0,8887	0,8682	1,0000	0,9426	0,9458	0,9344	0,9323	0,9144
BAND5	0,8665	0,8784	0,7920	0,9426	1,0000	0,9780	0,9712	0,9674	0,9606
BAND6	0,8556	0,8742	0,8134	0,9458	0,9780	1,0000	0,9686	0,9673	0,9620
BAND7	0,8627	0,8803	0,8003	0,9344	0,9712	0,9686	1,0000	0,9813	0,9659
BAND8	0,8578	0,8812	0,8078	0,9323	0,9674	0,9673	0,9813	1,0000	0,9741
BAND9	0,8329	0,8612	0,7939	0,9144	0,9606	0,9620	0,9659	0,9741	1,0000

EIGENVALUES AND ASSOCIATED PRECENTAGES			
AXIS	EIGENVALUES	PERCENTAGES	CUMULATIVE
1	278,8133	94,4846	94,4846
2	11,6089	3,9340	98,4186
3	3,3172	1,1241	99,5428
4	1,2384	0,4197	99,9624
5	0,0853	0,0289	99,9913
6	0,0118	0,0040	99,9953
7	0,0080	0,0027	99,9980
8	0,0039	0,0013	99,9994
9	0,0019	0,0006	100,0000

EIGENVECTORS								
RASTER	BAND1	BAND2	BAND3N	BAND4	BAND5	BAND6	BAND7	BAND8	BAND9
BAND1	0,5950	0,6207	0,4890	0,1341	0,0332	0,0336	0,0279	0,0200	0,0122
BAND2	-0,4864	-0,2075	0,8478	0,0353	-0,0164	-0,0045	-0,0103	-0,0049	-0,0018
BAND3N	0,6331	-0,7516	0,1768	0,0406	-0,0165	-0,0174	-0,0182	-0,0161	-0,0120
BAND4	-0,0910	-0,0689	-0,0984	0,9090	0,2212	0,2248	0,1745	0,1224	0,0778
BAND5	0,0147	-0,0445	0,0335	-0,3899	0,4850	0,5158	0,4405	0,3147	0,2243
BAND6	-0,0015	0,0044	-0,0001	-0,0216	0,3447	0,5221	-0,6590	-0,3947	-0,1342
BAND7	0,0046	0,0017	-0,0077	0,0088	-0,7683	0,6338	0,0584	0,0640	0,0158
BAND8	0,0036	-0,0022	-0,0022	0,0088	-0,0405	-0,0751	-0,5741	0,6623	0,4736
BAND9	0,0015	0,0000	-0,0013	0,0100	-0,0585	-0,0456	0,0831	-0,5355	0,8371
TOTAL VARIANCE		295,0887						
DETERMINANT		0,0000						

Table 5.3 Transformation Parameters of PCA of ASTER VNIR and SWIR bands

TRANSLATION VECTOR

| 61,0181 | 0,8062 | 6,1839 | 0,0928 | 0,6526 | 0,0492 | -0,1385 | 0,0413 | 0,1208 | |

TRANSFORMATION MATRIX

RASTER	BAND1	BAND2	BAND3N	BAND4	BAND5	BAND6	BAND7	BAND8	BAND9
BAND1	0,3027	0,3157	0,2488	0,0682	0,0169	0,0171	0,0142	0,0102	0,0062
BAND2	-0,3012	-0,1285	0,5250	0,0218	-0,0102	-0,0028	-0,0064	-0,0030	-0,0011
BAND3N	0,3763	-0,4467	0,1051	0,0242	-0,0098	-0,0104	-0,0108	-0,0096	-0,0071
BAND4	-0,0458	-0,0346	-0,0495	0,4573	0,1112	0,1131	0,0878	0,0616	0,0391
BAND5	0,0060	-0,0181	0,0136	-0,1583	0,1969	0,2094	0,1789	0,1278	0,0911
BAND6	-0,0007	0,0021	0,0000	-0,0104	0,1655	0,2507	-0,3165	-0,1895	-0,0645
BAND7	0,0029	0,0011	-0,0050	0,0056	-0,4915	0,4055	0,0374	0,0410	0,0101
BAND8	0,0019	-0,0012	-0,0012	0,0048	-0,0220	-0,0407	-0,3116	0,3594	0,2571
BAND9	0,0009	0,0000	-0,0008	0,0064	-0,0372	-0,0290	0,0529	-0,3405	0,5323

CORRELATION BETWEEN INPUT RASTERS AND PRINCIPAL COMPONENT

RASTER	BAND1	BAND2	BAND3N	BAND4	BAND5	BAND6	BAND7	BAND8	BAND9
BAND1	0,9799	0,9891	0,9420	0,9088	0,8789	0,8788	0,8802	0,8806	0,8599
BAND2	-0,1634	-0,0675	0,3332	0,0488	-0,0885	-0,0238	-0,0666	-0,0438	-0,0254
BAND3N	0,1137	-0,1306	0,0371	0,0300	-0,0477	-0,0497	-0,0628	-0,0776	-0,0917
BAND4	-0,0100	-0,0073	-0,0126	0,4107	0,3897	0,3916	0,3671	0,3593	0,3641
BAND5	0,0004	-0,0012	0,0011	-0,0462	0,2242	0,2358	0,2431	0,2423	0,2754
BAND6	0,0000	0,0000	0,0000	-0,0010	0,0593	0,0888	-0,1353	-0,1131	-0,0613
BAND7	0,0000	0,0000	-0,0001	0,0003	-0,1086	0,0885	0,0099	0,0151	0,0059
BAND8	0,0000	0,0000	0,0000	0,0002	-0,0040	-0,0073	-0,0678	0,1092	0,1245
BAND9	0,0000	0,0000	0,0000	0,0002	-0,0041	-0,0031	0,0069	-0,0618	0,1542
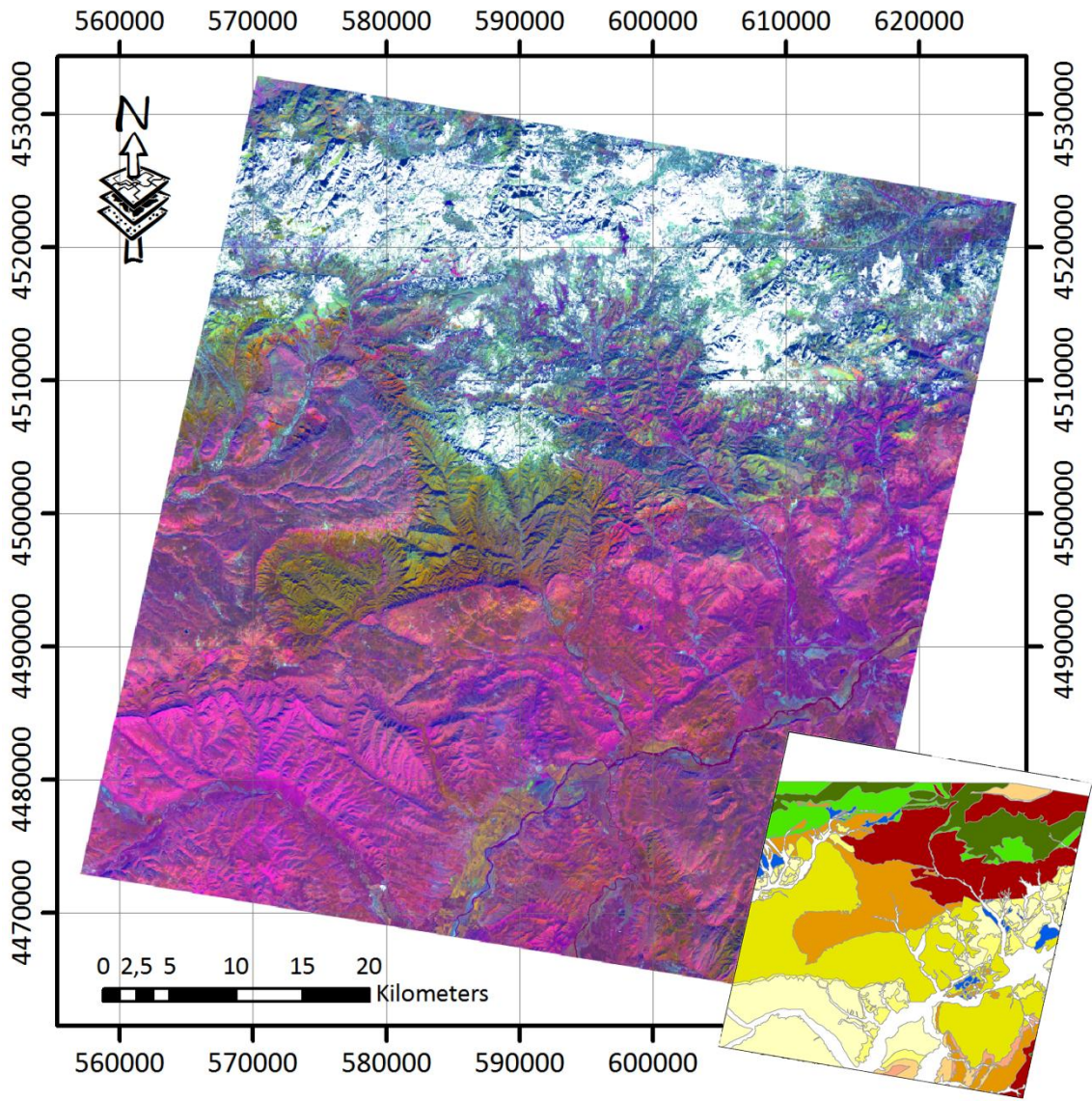
Figure 5.6 RGB color composite of principal components (R: PC1, G: PC2, B: PC3). *Note that the white area on the figure represents the vegetation. See Figure 2.2 for legend of the inset map.*

On the Figure 5.6 mainly three units stand out; brownish green unit in the middle of the image, pale pinkish unit in the west and east of the image and bright pink unit in the south east of the image. As the results are compared with the geological map, the green units corresponds to the continental red clastics (İncik Formation), bright pink unit corresponds to evaporites (Bozkır Formation) and pale pink unit corresponds to evaporates and shale/marl (Tuğlu Formation).
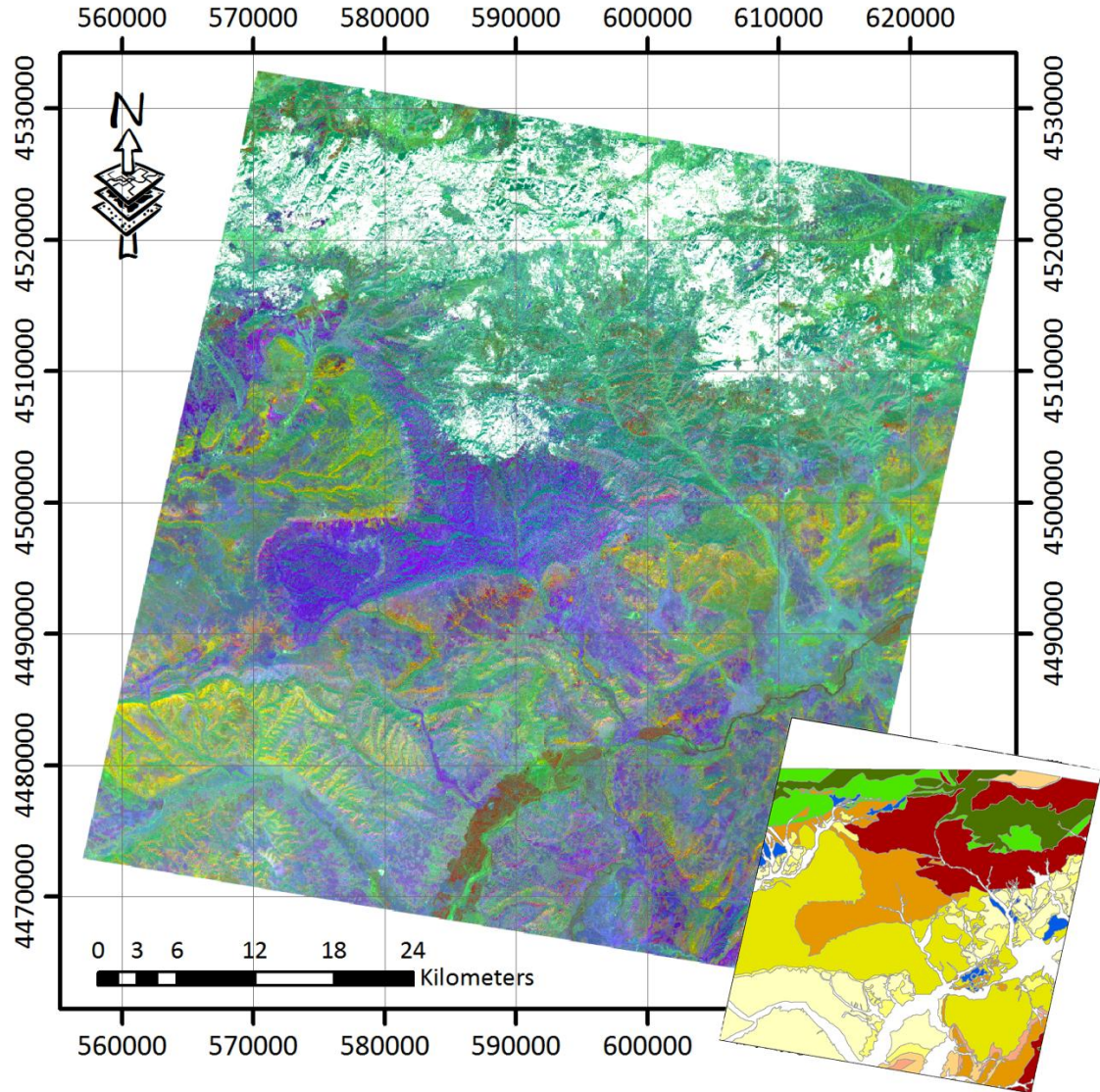
Figure 5.7 RGB color composite of principal components (R: PC1, G: PC3, B: PC5). *Note that the white area on the figure represents the vegetation. See Figure 2.2 for legend of the inset map.*

As on the previous image on Figure 5.7 three distinct units stand out; continental red clastics (İncik formation) is represented by blue-navy color in the middle, north-west and south-east of the image, Paleocene-Eocene units are represented by light green-turquoise color in the north-east of the image and evaporites (Tuğlu and Bozkır Formations) represented by greenish-yellowish color. Note that the evaporitic units were not recognized as separate units as in the previous image.
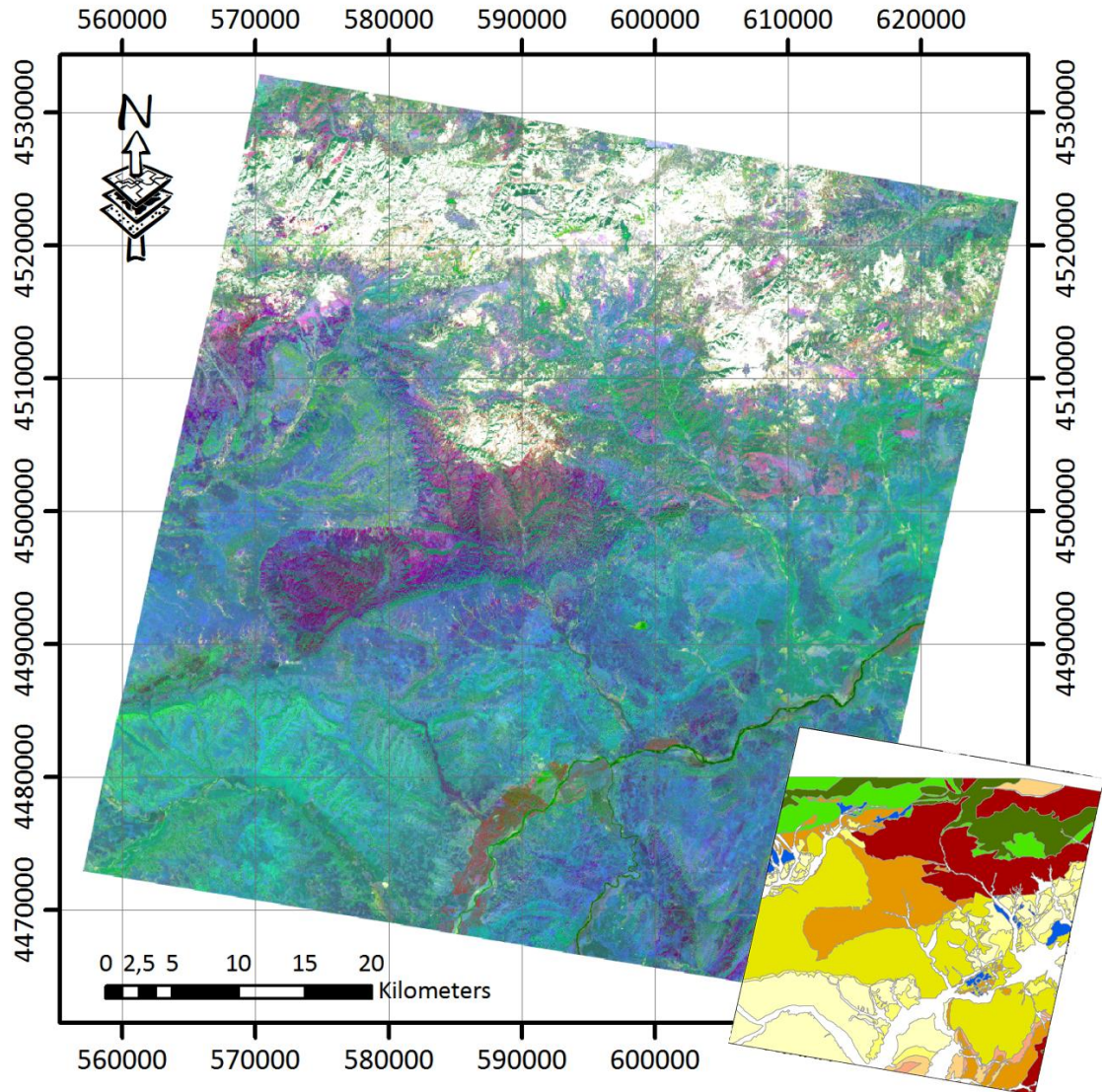
Figure 5.8 RGB color composite of principal components (R: PC2, G: PC3, B: PC4). *Note that the white area on the figure represents the vegetation. See Figure 2.2 for legend of the inset map.*

On Figure 5.8 only continental red clastics (İncik Formation) stands out by blue-navy color while the rest of the image has not so different color composition. On Figure 5.9, on the other hand, no distinct unit stands out and the whole image has quite same color composition. Therefore, Figure 5.9 and the principal component used for RGB composite would not be efficient for surface material discrimination.
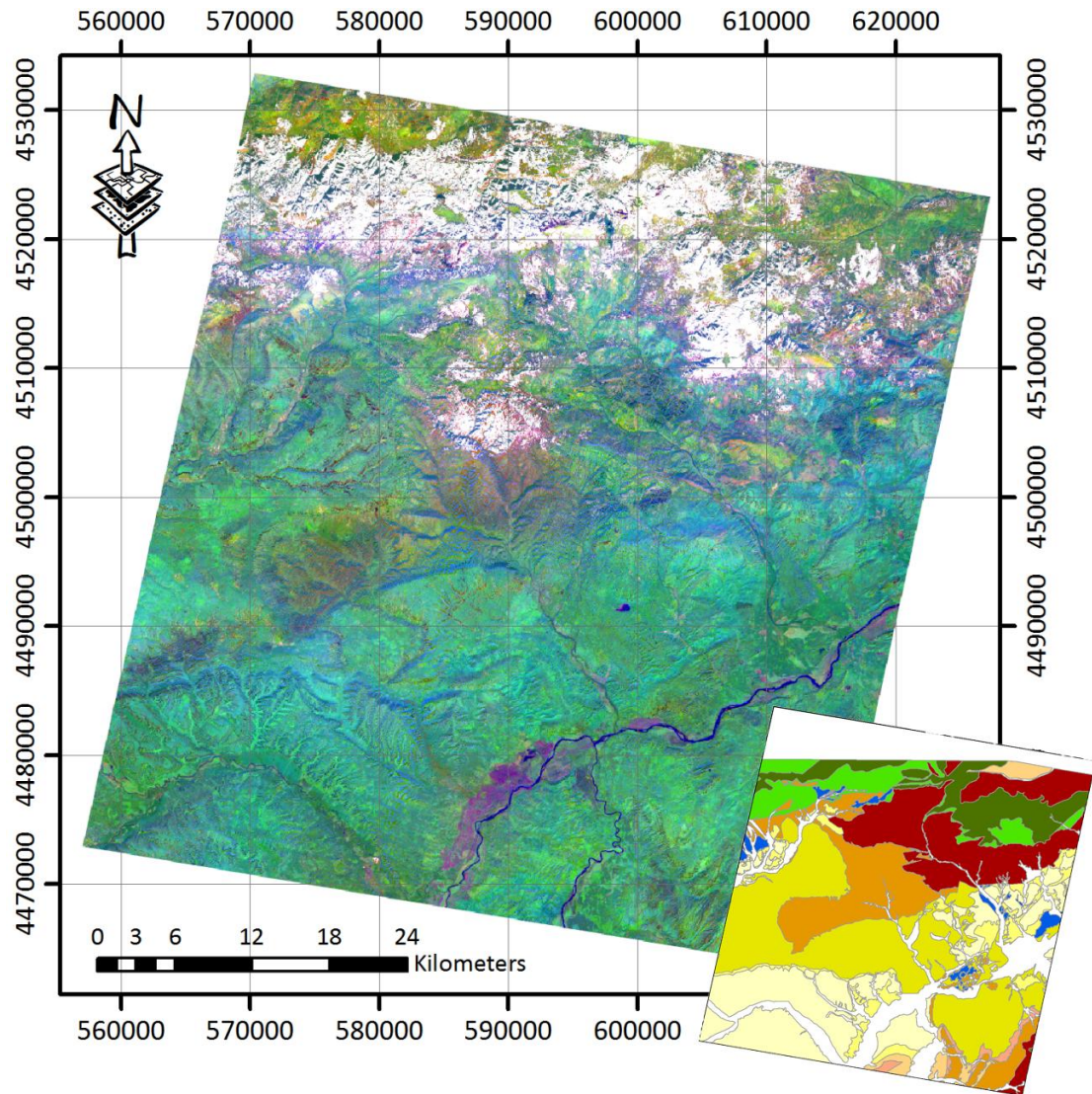
Figure 5.9 RGB color composite of principal components (R: PC2, G: PC4, B: PC6). *Note that the white area on the figure represents the vegetation. See Figure 2.2 for legend of the inset map.*

The results of the principal component analysis showed that through interpretation RGB color composites produced using principal component is capable to discriminate surface materials based on the variance between the materials. Based on the selection of the principal components the materials delineated may change. Essentially, starting with the PC1 through PC9 the components show the abundance of the information embedded. In other words, PC1 represents the information abundant and mediocre for the image while the mediocrity decreases gradually for latter principal components.

5.3. Decorrelation Stretch

Decorrelation Stretch is performed using MicroImages TNTmips software like most of the other image processing operations.. The Decorrelation Stretch is utilized for ASTER VNIR and SWIR bands (Bands 1-9. For spatial coherence, the spatial resolution of SWIR bands resampled to 15m to match them with the VNIR bands. In this data set, vegetation mask is also applied as explained previously. Therefore, the vegetation pixels are not included in analysis.

Essentially, the combination of the RGB color composites produced are the same as the ones produced for preprocessed ASTER VNIR and SWIR data (Figure 5.1, Figure 5.2 and Figure 5.3). The main difference, however, here is that on the same bands decorrelation contrast enhancement is applied. Following the contrast enhancement through principal component transformation decorrelated (statistically independent) bands are then retransformed into their original coordinates so that the distortion of hues due to decorrelation transformation is limited.

The first RGB color composite is the false color composite produced from decorrelated VNIR bands 3N, 2 and 1 (RGB: 3N, 2, 1) (Figure 5.10). As seen on the figure the contrast of the image increased discernibly when it is compared to the first false color composite produced. The additional RGB color composites can be seen in Figures 5.11 and 5.12. It can easily be seen that surface materials showing different responses in SWIR and VNIR can be discriminated through contrast enhanced images. Note that unlike principal component analysis the meaning of the colors and relation between the bands and the materials are known in decorrelation stretch.
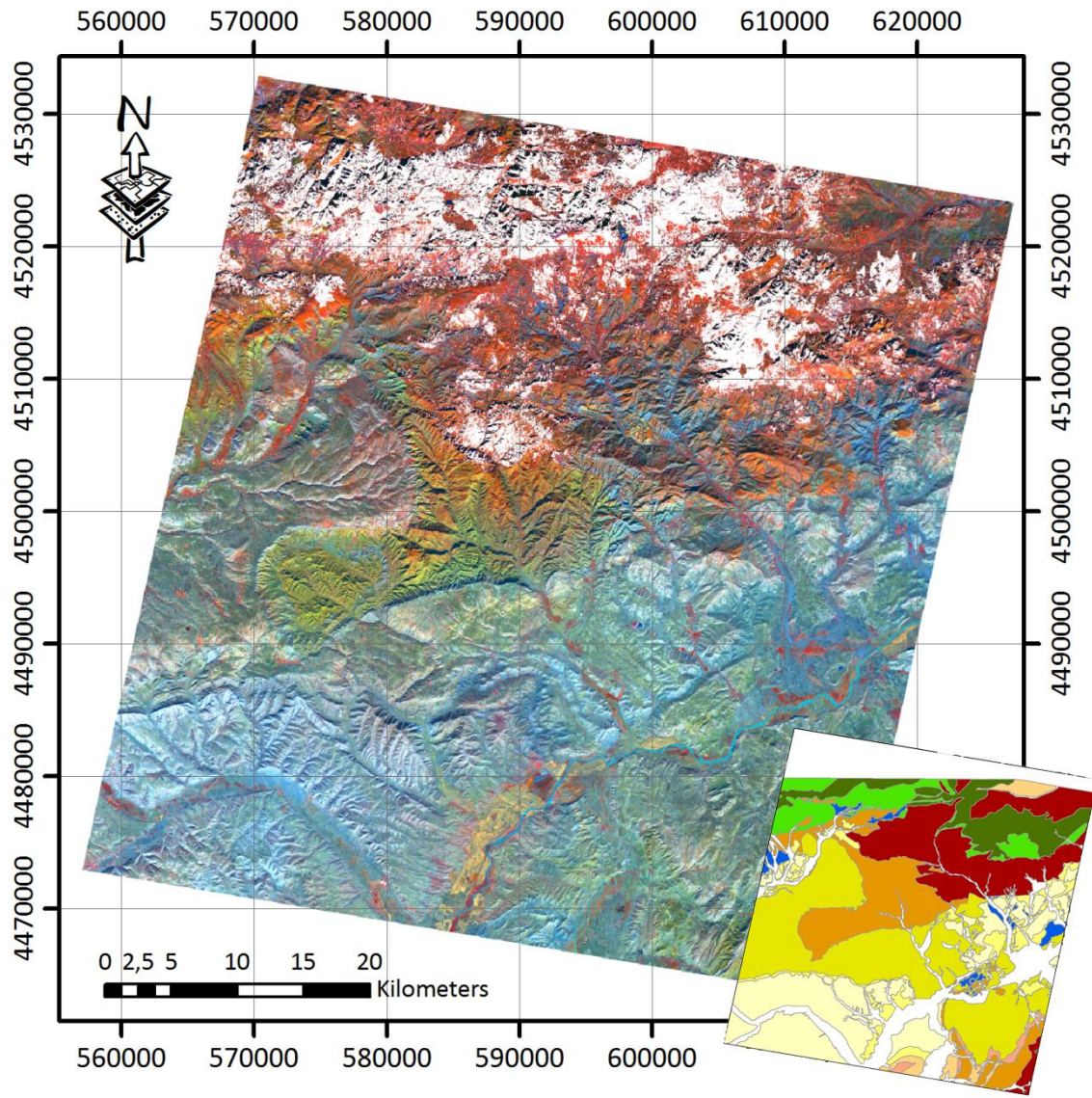
Figure 5.10 RGB color composite of decorrelated bands (R: Band-3N, G: Band-2, B: Band-1). *Note that the white area on the figure represents the vegetation. See Figure 2.2 for legend of the inset map.*

Several units stands out on Figure 5.10; continental red clastics (İncik Formation) represented by brownish-green color, evaporites (Bozkır Formation) represented by bluish gray, evaporites and shale/marl (Tuğlu Formation) represented by pale greenish-gray.
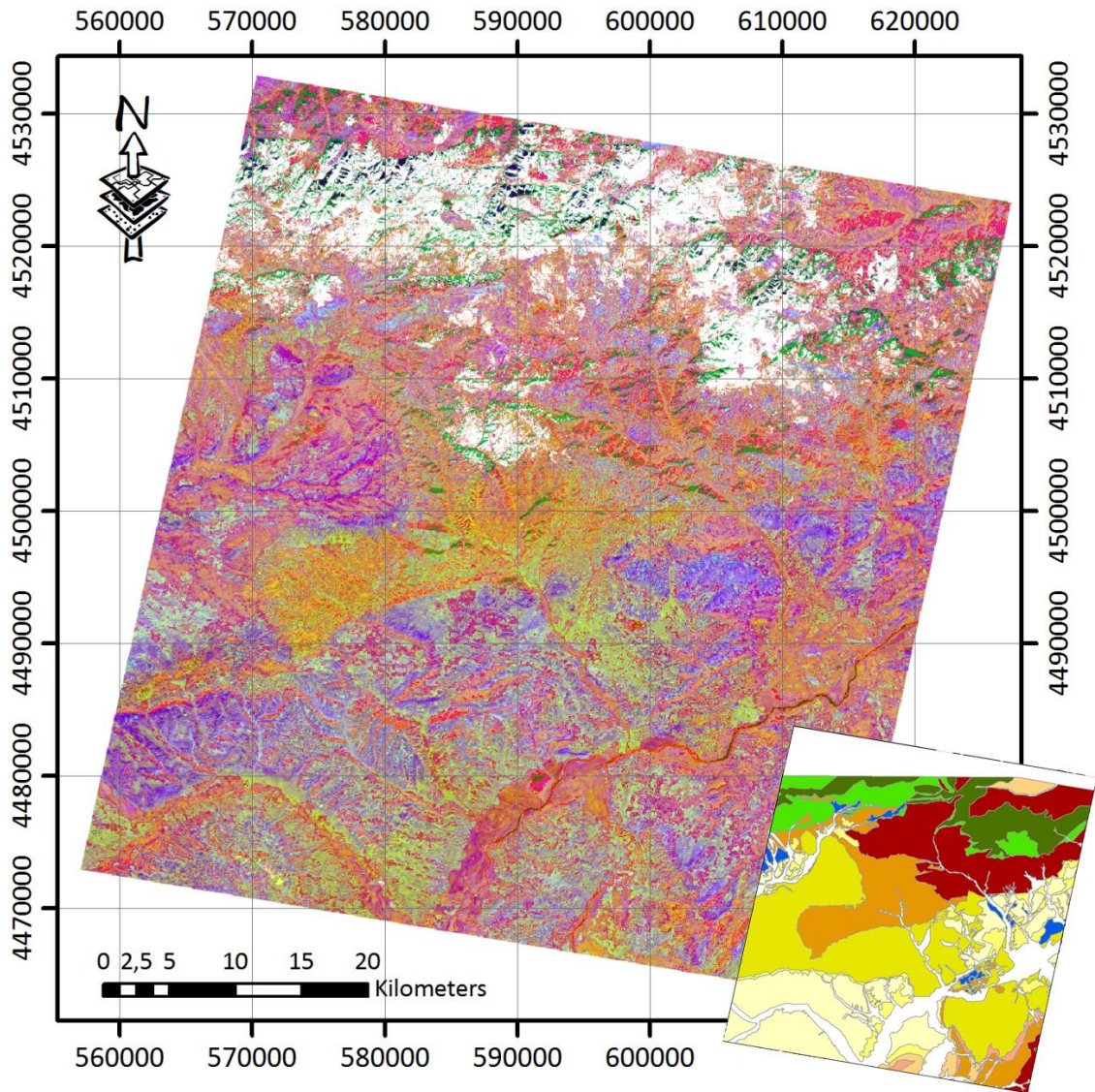
Figure 5.11 RGB color composite of decorrelated bands (R: Band-9, G: Band-6, B: Band-4). *Note that the white area on the figure represents the vegetation. See Figure 2.2 for legend of the inset map.*

On Figures 5.11 and 5.12, basically, two distinct units stand out: (1) the continental red clastics (İncik Formation) and (2) evaporitic units (Tuğlu and Bozkır Formations). On Figure 5.11, continental red clastics are represented by yellow-orange color where evaporitic units are represented by pinkish-purple color. On Figure 5.12, red-orange color shows continental red clastics and greenish color shows evaporitic units.
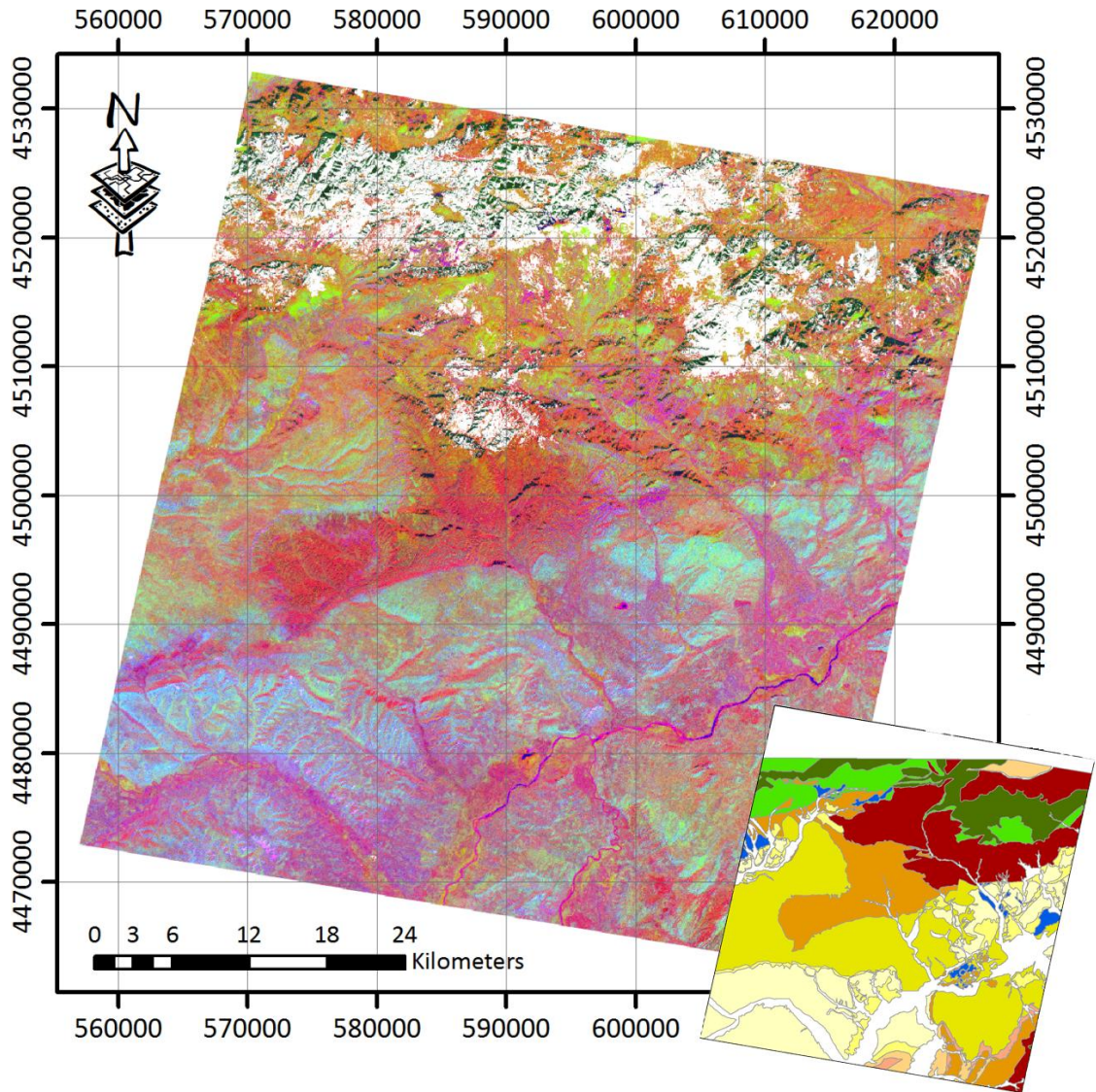
Figure 5.12 RGB color composite of decorrelated bands (R: Band-9, G: Band-4, B: Band-1). *Note that the white area on the figure represents the vegetation. See Figure 2.2 for legend of the inset map.*

5.4. Spectral Indices

In this study, quartz (QI), carbonate (CI), mafic (MI) indices defined by Ninomiya (2002) and sulfate (SI) index defined by and Öztan and Süzen (2011) for TIR data along with calcite (CI_{SWIR}), OH bearing altered mineral (OHI_a and OHI_b) and alunite (ALI) indices defined for SWIR by Ninomiya (2004) are used. The results of the spectral indices are displayed in linear gray-scale as the resultant image is a single layer. Additionally, in order to facilitate visual interpretation, the resultant layers are subjected to contrast enhancement through linear stretching.

Primarily, the spectral indices for SWIR bands are calculated starting with alunite index (ALI) (Eq.5.1). Although most of the hydroxyl bearing minerals is silicates, alunite is sulfate mineral which has a unique spectral feature. In 2.295 – 2.365 µm wavelength region which corresponds to ASTER SWIR Band-8, alunite has a sharp absorption feature unlike the other hydroxyl bearing minerals. The resultant image is linearly stretched for better contrast and interpretation (Figure 5.13).

$$ALI = \frac{Band7 * Band7}{Band5 * Band8}$$
(E.q.5.1)

The second index calculated for SWIR is the calcite index (CI_{SWIR}) (Eq.5.2). Calcite shows featured spectral response in SWIR, that is, in 2.295 – 2.365 µm wavelength region (ASTER SWIR Band-8) calcite has a deep and wide absorption while showing rather high reflectance in 2.185 – 2.225 µm wavelength region (ASTER SWIR Band-6) and in 2.360 – 2.430 µm wavelength regions (ASTER SWIR Band-9). The resultant image can be seen on Figure 5.14.

$$CI_{SWIR} = \frac{Band6 * Band9}{Band8 * Band8}$$
(E.q.5.2)

Two other indices calculated for SWIR are hydroxyl bearing altered minerals indices (Eq.5.3) Note that for hydroxyl bearing altered minerals two different indices are defined. The first index designated by OHI_a is mainly used for montmorillonite and mica both of which have similar deep and sharp absorption feature in 2.185 – 2.225 µm wavelength region (ASTER SWIR Band-6). The latter index designated by OH_b is used for pyrophillite which has a deep and sharp

absorption feature in 2.145 – 2.185 μm wavelength region (ASTER SWIR Band-5). The results of the spectral indices are depicted in Figures 5.15 and 5.16.

$$OHI_a = \frac{Band\,4 * Band\,7}{Band\,6 * Band\,6} \; ; \; OHI_b = \frac{Band\,4 * Band\,7}{Band\,5 * Band\,5} \qquad \text{(E.q.5.3)}$$
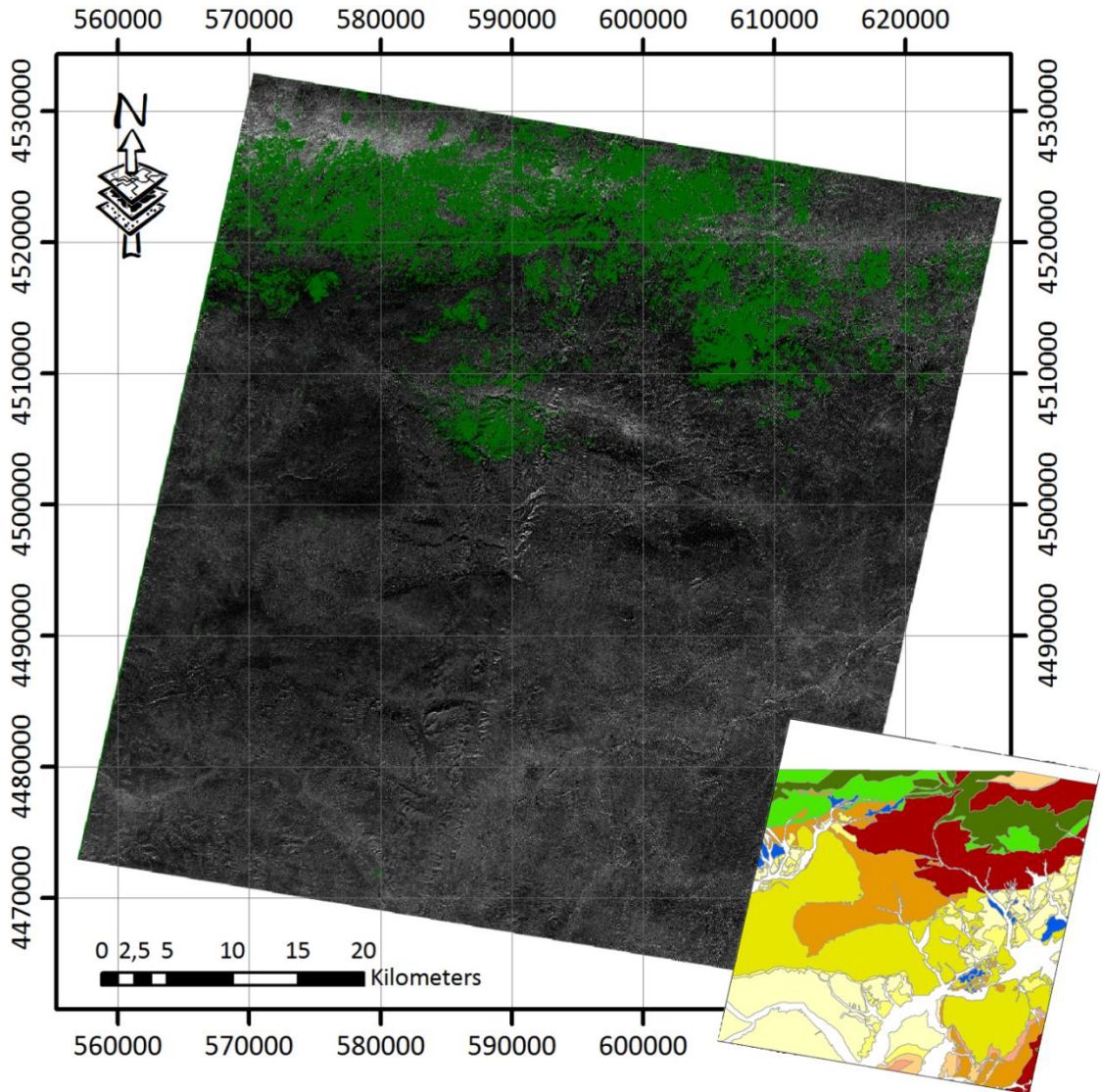
Figure 5.13 Alunite Index (ALI). Brighter pixels are expected to show higher alunite composition. *Note that the green area on the figure represents the vegetation. See Figure 2.2 for legend of the inset map.*
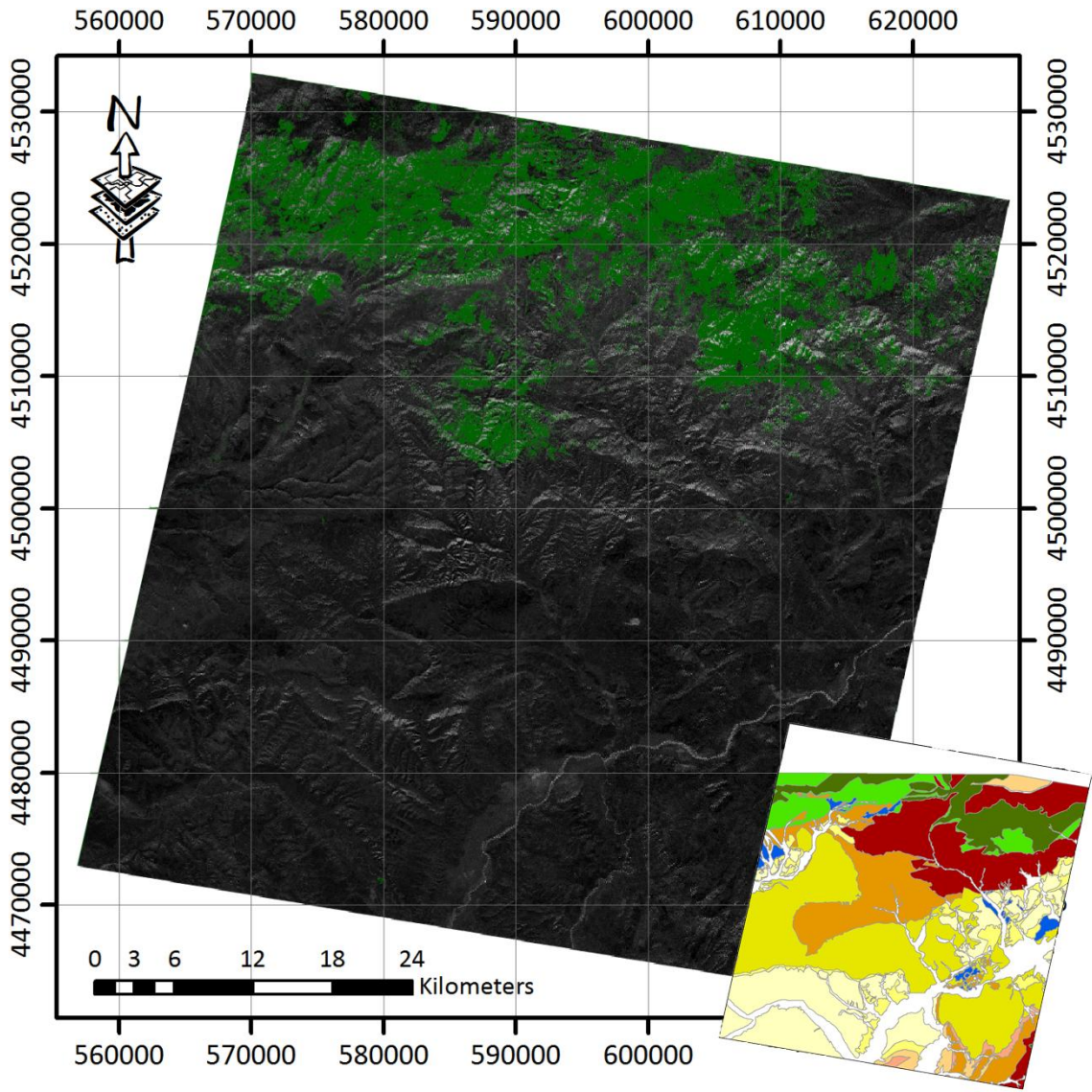
Figure 5.14 Calcite Index (CI$_{SWIR}$). Brighter pixels are expected to show higher calcite composition *Note that the green area on the figure represents the vegetation. See Figure 2.2 for legend of the inset map.*
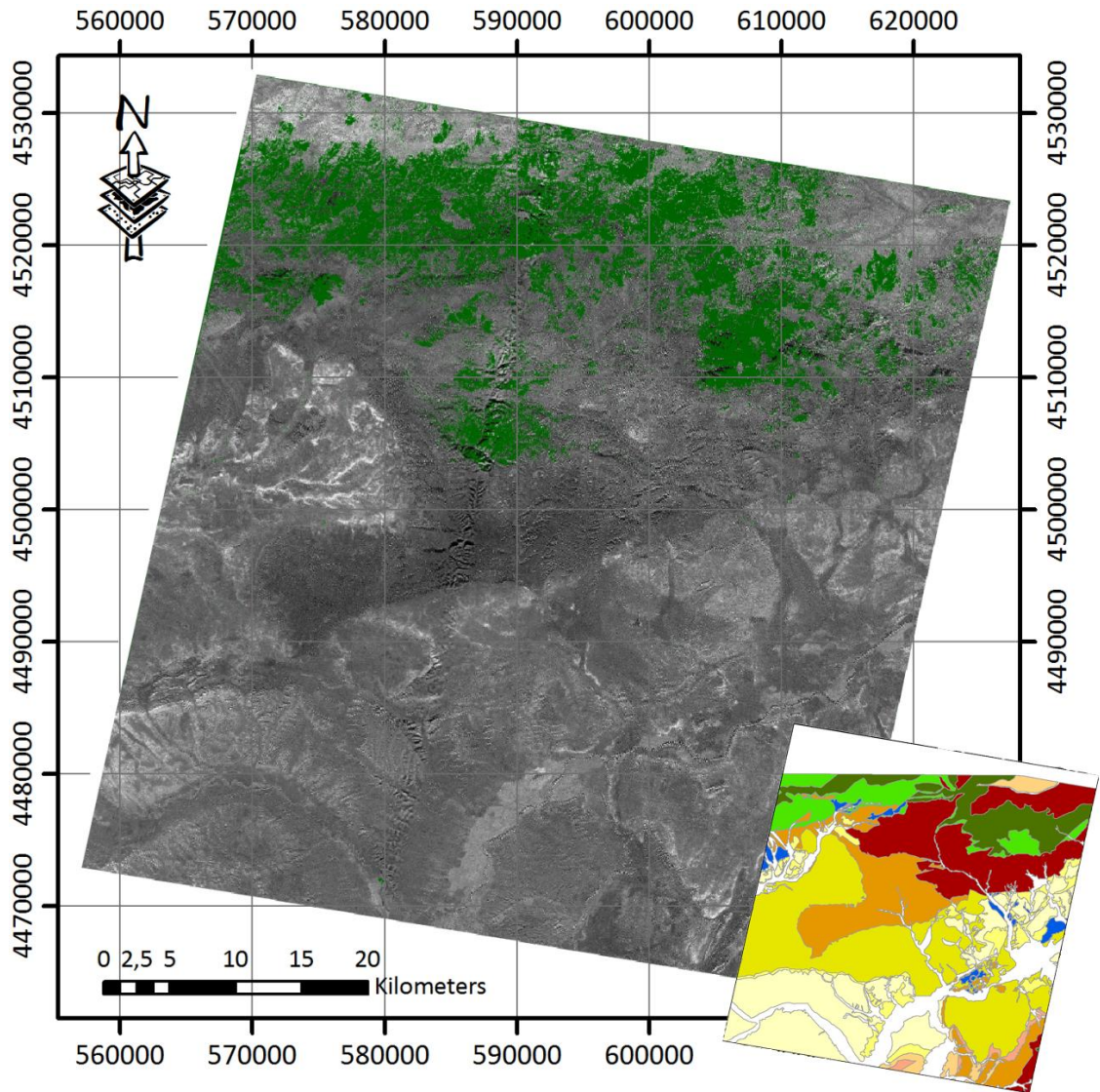
Figure 5.15 Hydroxyl Bearing Altered Minerals Index (OHI$_a$). Brighter pixels are expected to show higher OH bearing altered mineral (particularly, montmorillonite and mica) composition *Note that the green area on the figure represents the vegetation. See Figure 2.2 for legend of the inset map.*
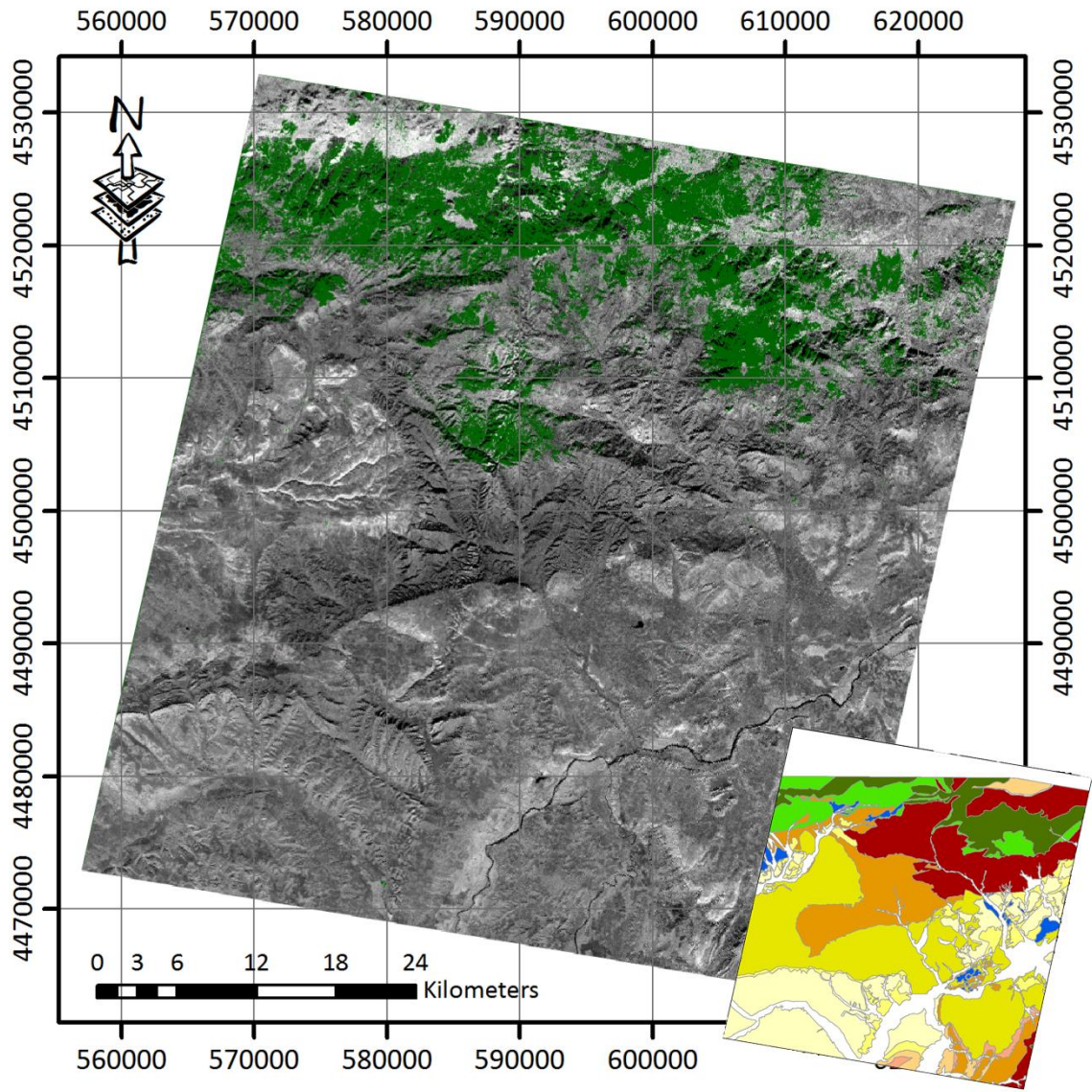
Figure 5.16 Hydroxyl Bearing Altered Minerals Index (OHI$_b$). Brighter pixels are expected to show higher OH bearing altered mineral (particularly, pyrophillite) composition *Note that the green area on the figure represents the vegetation. See Figure 2.2 for legend of the inset map.*

Following the indices defined for SWIR bands, indices defined for TIR bands are also calculated. From the spectral absorption property of quartz, the index is defined as in Eq.5.4. Essentially, quartz show high emissivity in 8.475 – 8.825 μm wavelength region (ASTER TIR Band-11) while showing high absorption in 8.125 – 8.475 μm wavelength region (ASTER TIR Band-10) and 8.925 – 9.275 μm wavelength regions (ASTER TIR Band-12). The applied result of QI index can be seen in Figure 5.17.

$$QI = \frac{Band11 * Band11}{Band10 * Band12}$$ (Eq.5.4)

The second index calculated for TIR is the carbonate index (CI) which is mainly used for carbonate rocks composed of calcite and dolomite two major carbonate minerals on the earth. The essential difference from the calcite index for SWIR (CI_{SWIR}) is that CI index uses emissivity and absorption property of the carbonate minerals in TIR and defined as in Eq.5.5. The result of the calculation of the CI index is depicted in Figure 5.18.

$$CI = \frac{Band13}{Band14}$$ (Eq.5.5)

The mafic index (MI) which is essentially based on the bulk silica content of the target materials is defined by the Eq.5.6 based on the spectral emissivity and absorption property of silica.

$$MI = \frac{Band12}{Band13}$$ (Eq.5.6)

However it is also sensitive to carbonate rocks. In order to reduce the effect of carbonates in mafic index Ninomiya (2002) separated MI from carbonates through (E.q.5.7) and it is observed that the best separation would be in MI_3. Therefore mafic index is refined as follows:

$$MI_n = \frac{Band12}{Band13 * CI^n} = \frac{Band12 * Band14^n}{Band13^{n+1}} \Rightarrow MI_3 = \frac{Band12 * Band14^3}{Band13^4}$$ (E.q.5.7)

The applied results of both MI and MI_3 can be seen in Figures 5.19 and 5.20 respectively.

The last index calculated for TIR is the sulfate index (SI) (Öztan and Süzen 2011) which is essentially the inverse of the quartz index (QI). The spectral property of the sulfate minerals such as gypsum is almost opposite of quartz i.e. high emissivity in ASTER band-10 and band-12 region and high absorption in ASTER band-10 region (Eq.5.8). The applied result of SI can be seen in Figure 5.21.

$$SI = \frac{Band10*Band12}{Band11*Band11}$$ (Eq.5.8)
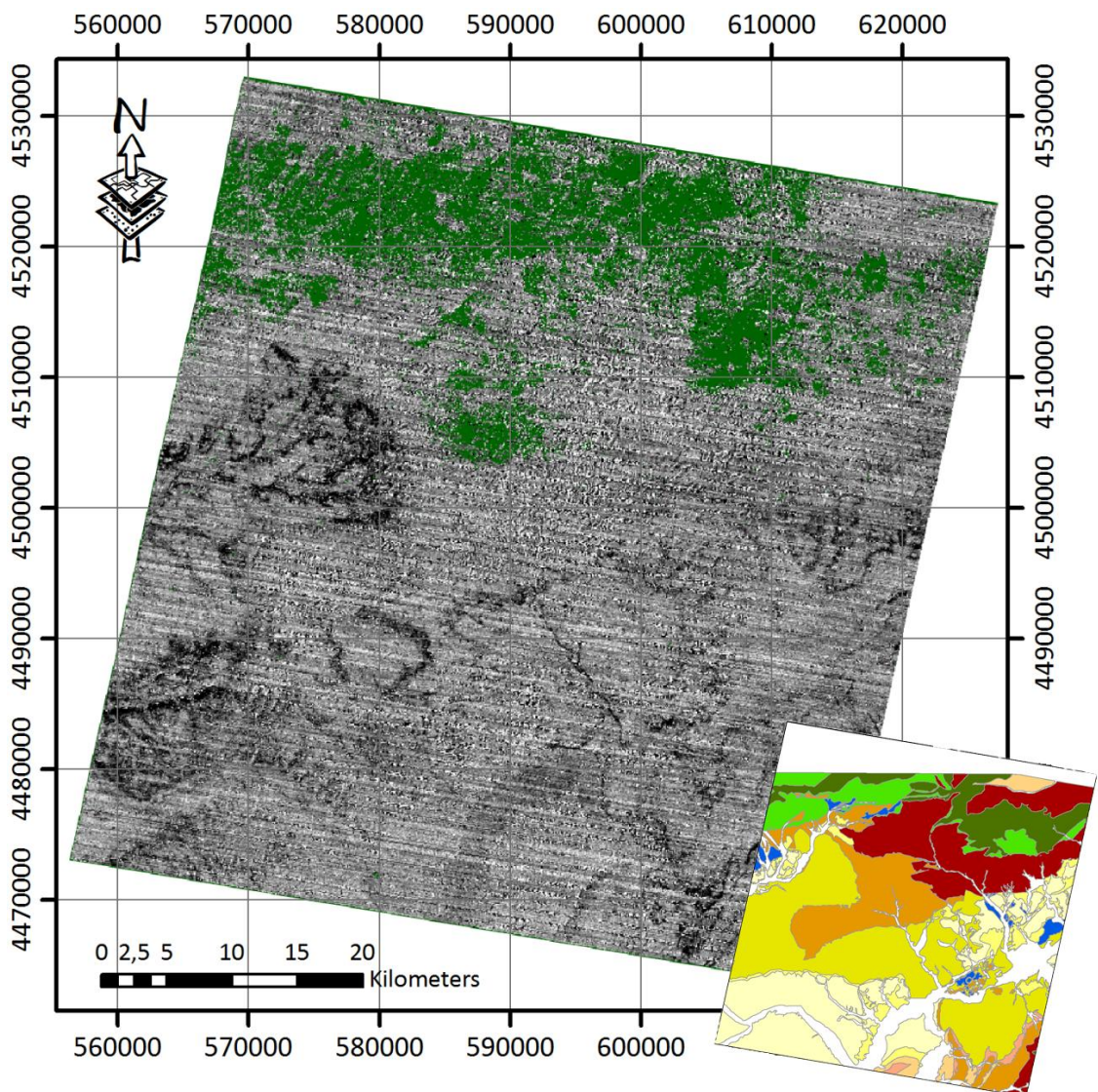
Figure 5.17 Quartz Index (QI). Brighter pixels are expected to show higher quartz composition. *Note that the green area on the figure represents the vegetation*
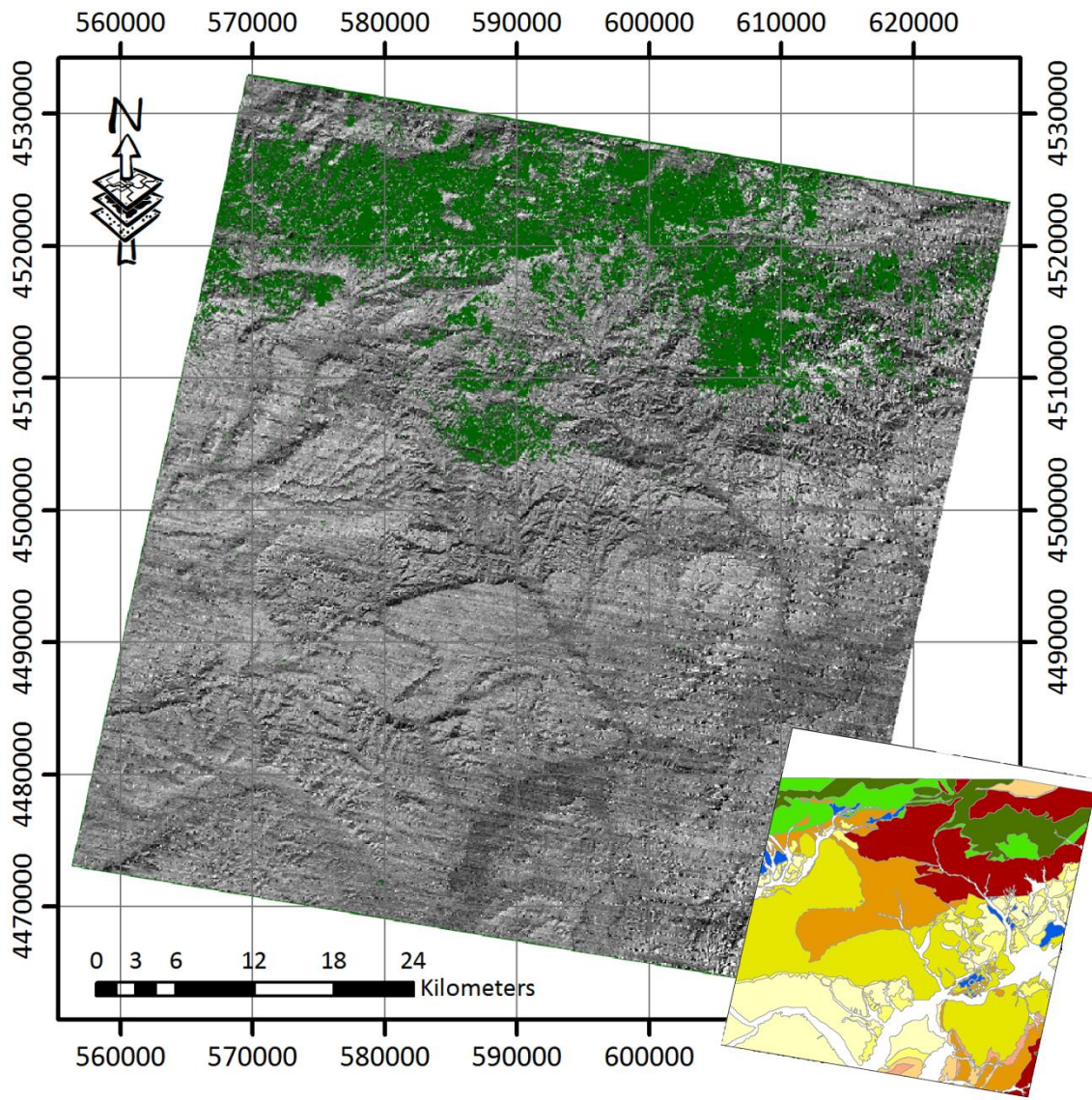
Figure 5.18 Carbonate Index (CI). Brighter pixels are expected to show higher carbonate composition. *Note that the green area on the figure represents the vegetation. See Figure 2.2 for legend of the inset map.*
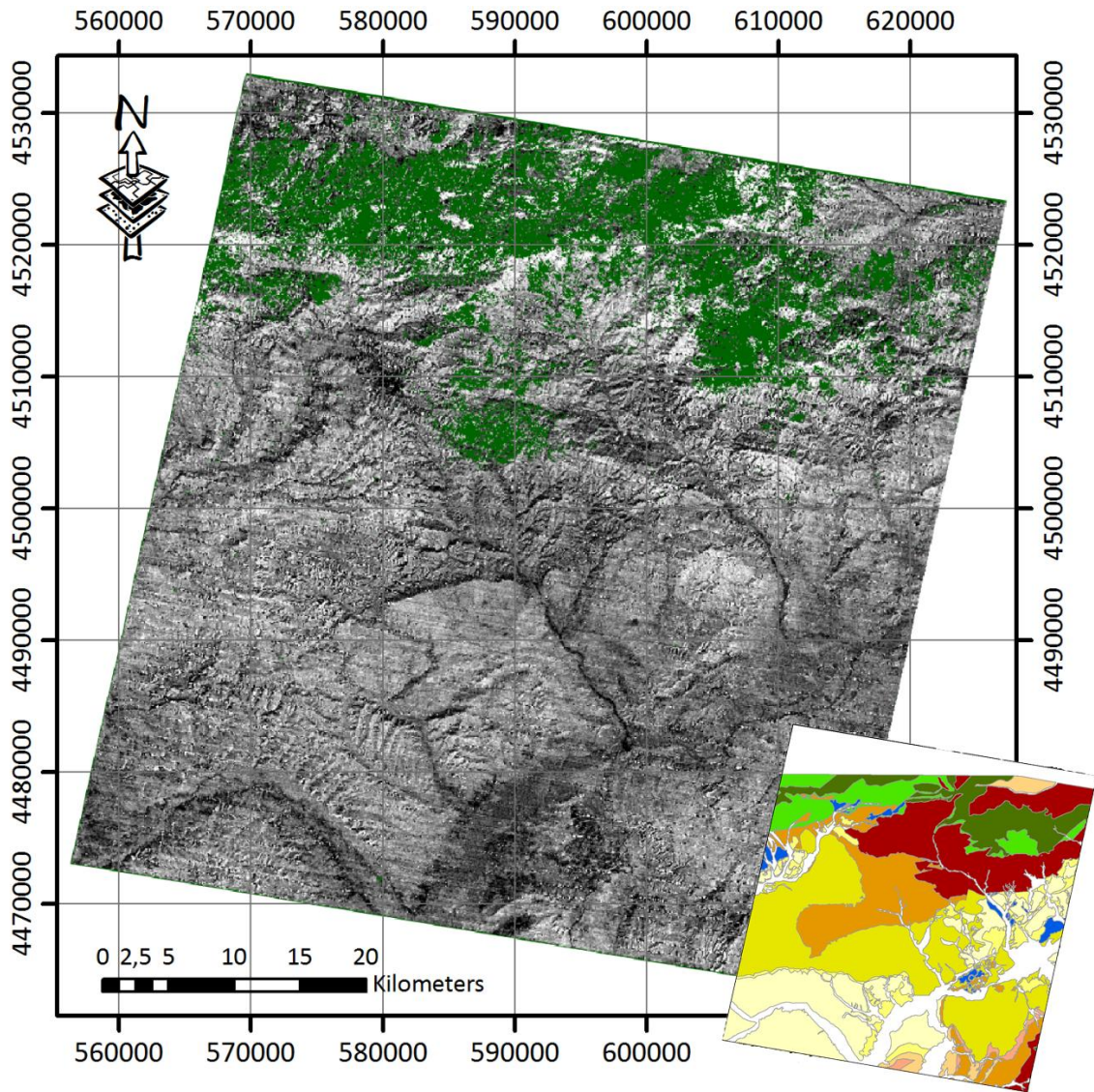
Figure 5.19 Mafic Index (MI). Brighter pixels are expected to show higher mafic composition. *Note that the green area on the figure represents the vegetation. See Figure 2.2 for legend of the inset map.*
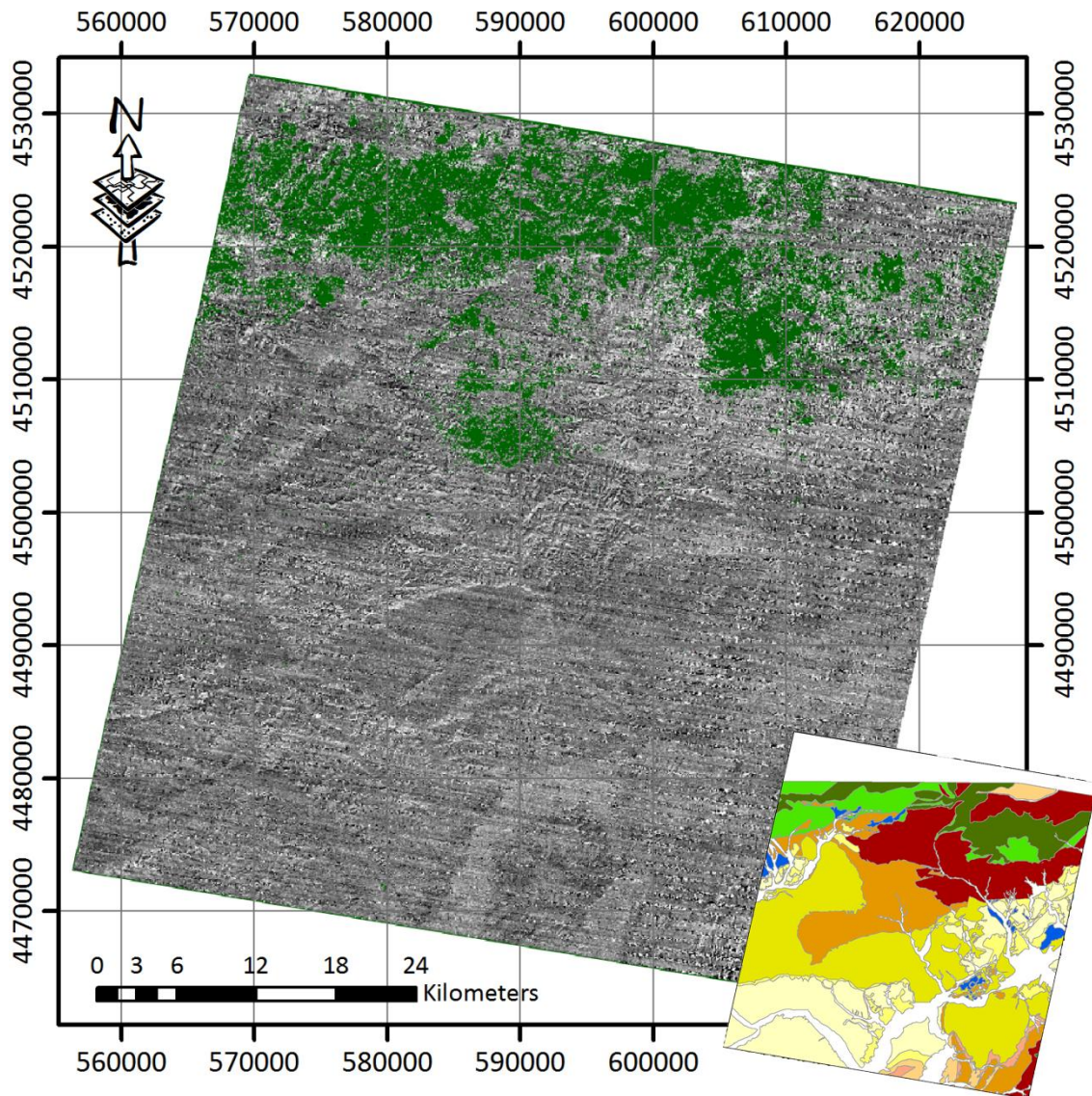
Figure 5.20 Mafic Index refined ($MI_{n=3}$). Brighter pixels are expected to show higher mafic composition with reduced effect of carbonates. *Note that the green area on the figure represents the vegetation. See Figure 2.2 for legend of the inset map.*
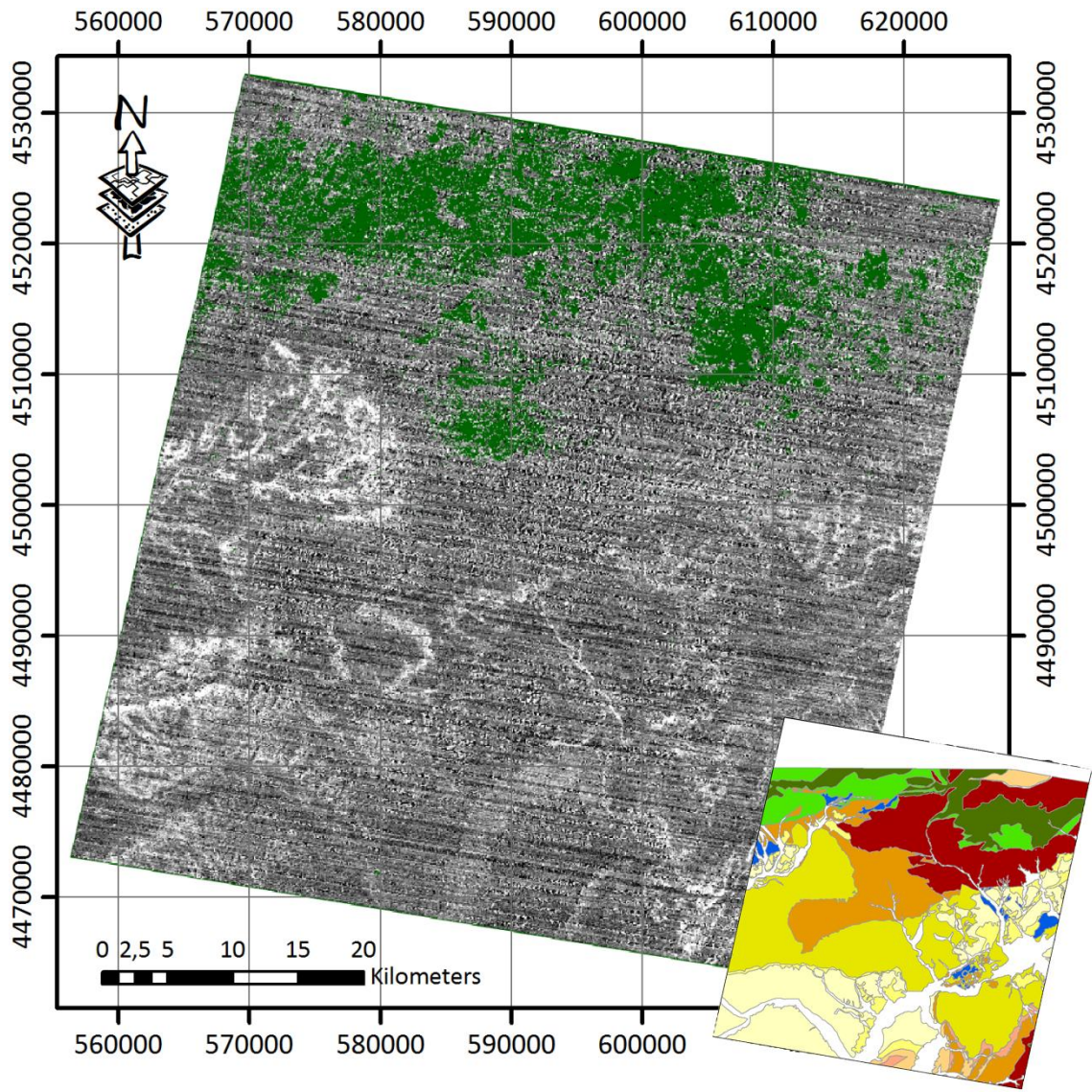
Figure 5.21 Sulfate Index (SI). Brighter pixels are expected to show higher sulfate mineral composition *Note that the green area on the figure represents the vegetation. See Figure 2.2 for legend of the inset map.*

5.5. Temperature – Emissivity Separation

Through TES algorithm emissivity values of five TIR bands (Band 10-14) is retained along with the surface temperature. The NDVI mask is not used through the temperature- emissivity separation since vegetation is a near-gray body and has representative emissivity and temperature values. However, in the algorithm the near-gray bodies (vegetation and water bodies) and selective radiators (surface materials) are treated separately. Thus, for vegetation and water bodies, a constant emissivity value (0.983), appropriate for near-gray bodies, is assigned while the rest is calculated as explained previously in the algorithm description.

The emissivity values from different bands are represented in RGB color composites for visual interpretation. Essentially, the discrimination of the surface materials is through identification of emissivity anomalies of the surface materials. Note that no quantitative approach is used for surface material classification through emissivity which is discussed in the next chapter.

Even though the surface temperature retained from the TES algorithm is not the primary concern of the study and does not bear any explicit meaning regarding the surface material discrimination, it is also provided so that the emissivity and temperature relationship could be well understood (Figure 5.22).

The first color composite is produced using TES emissivities of Band-13, Band-12 and Band-10 (RGB: 13, 12, 10) (Figure 5.23). The second RGB color composite comprises TES emissivities of Band-12, Band-11 and Band-10 (RGB: 12, 11, 10) (Figure 5.24) and the last RGB color composite is produced using TES emissivities of Band-14, Band-12 and Band-10 (RGB: 14, 12, 10) (Figure 5.25).

Note that the RGB color composites show almost the same pattern due to the fact that regardless of the band the emissivity values are not different greatly.
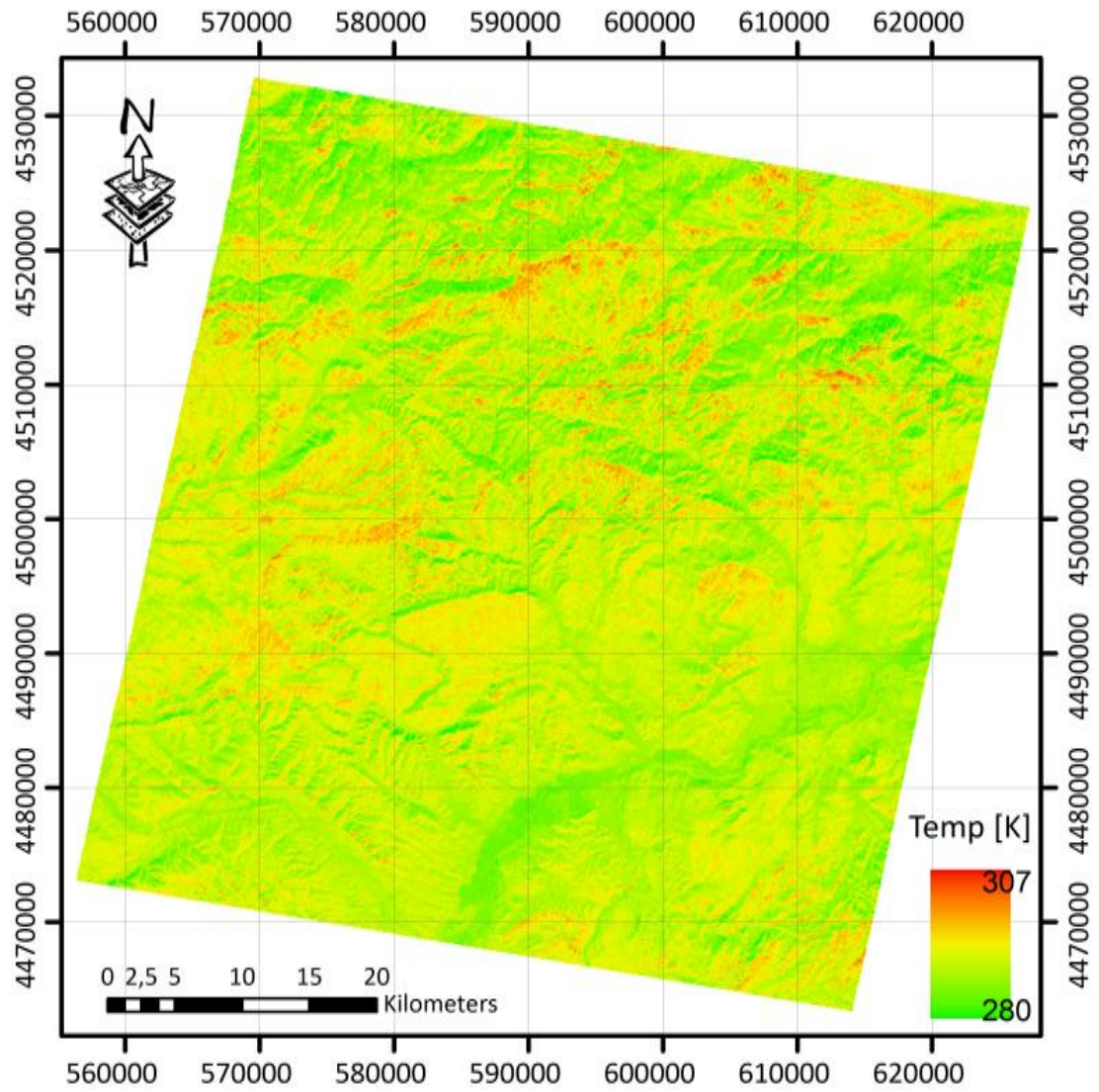
Figure 5.22 Surface kinetic temperature
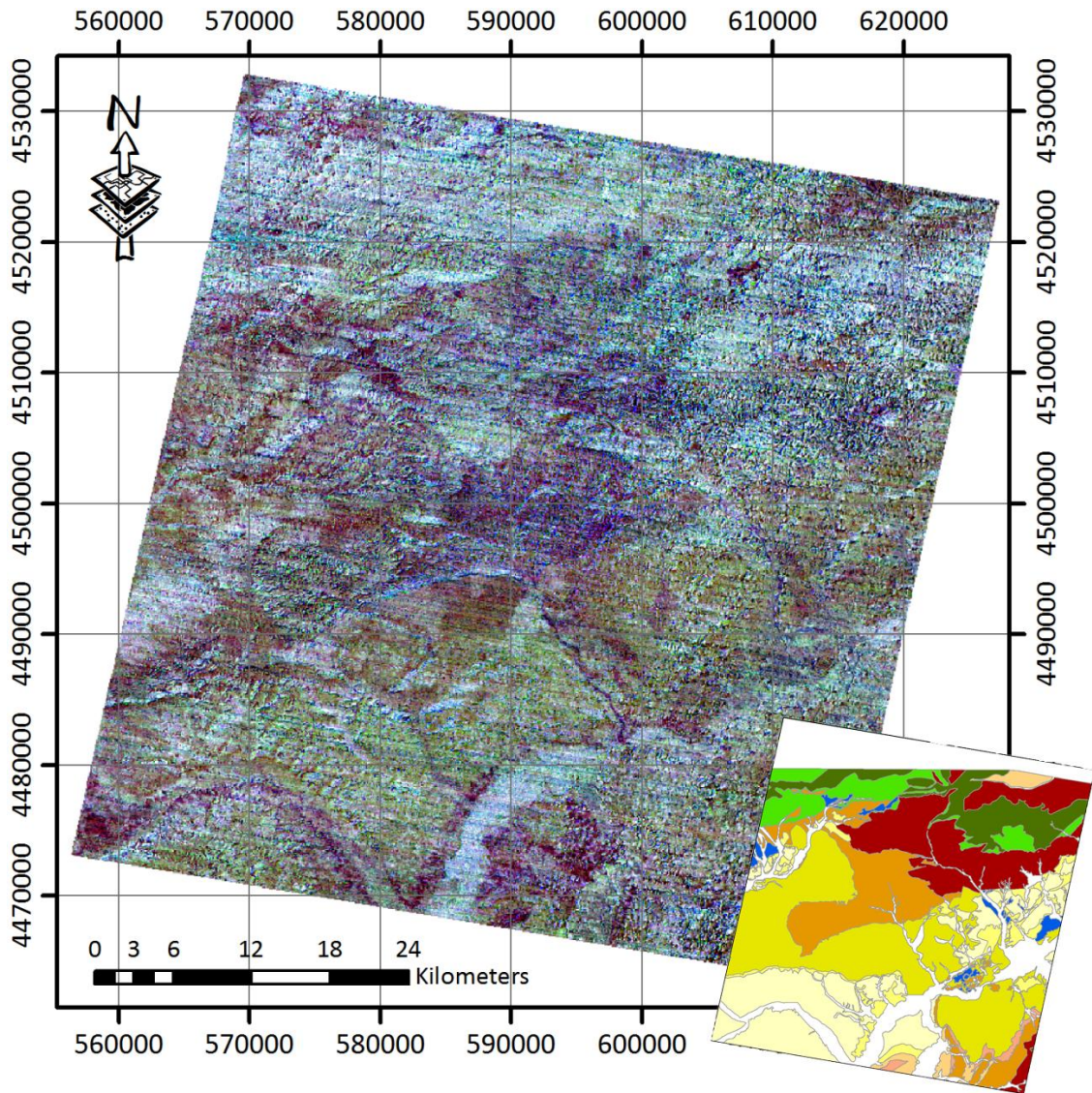
Figure 5.23 Emissivity color composite (R: Band-13 G: Band-12 B: Band-10). *See Figure 2.2 for legend of the inset map.*
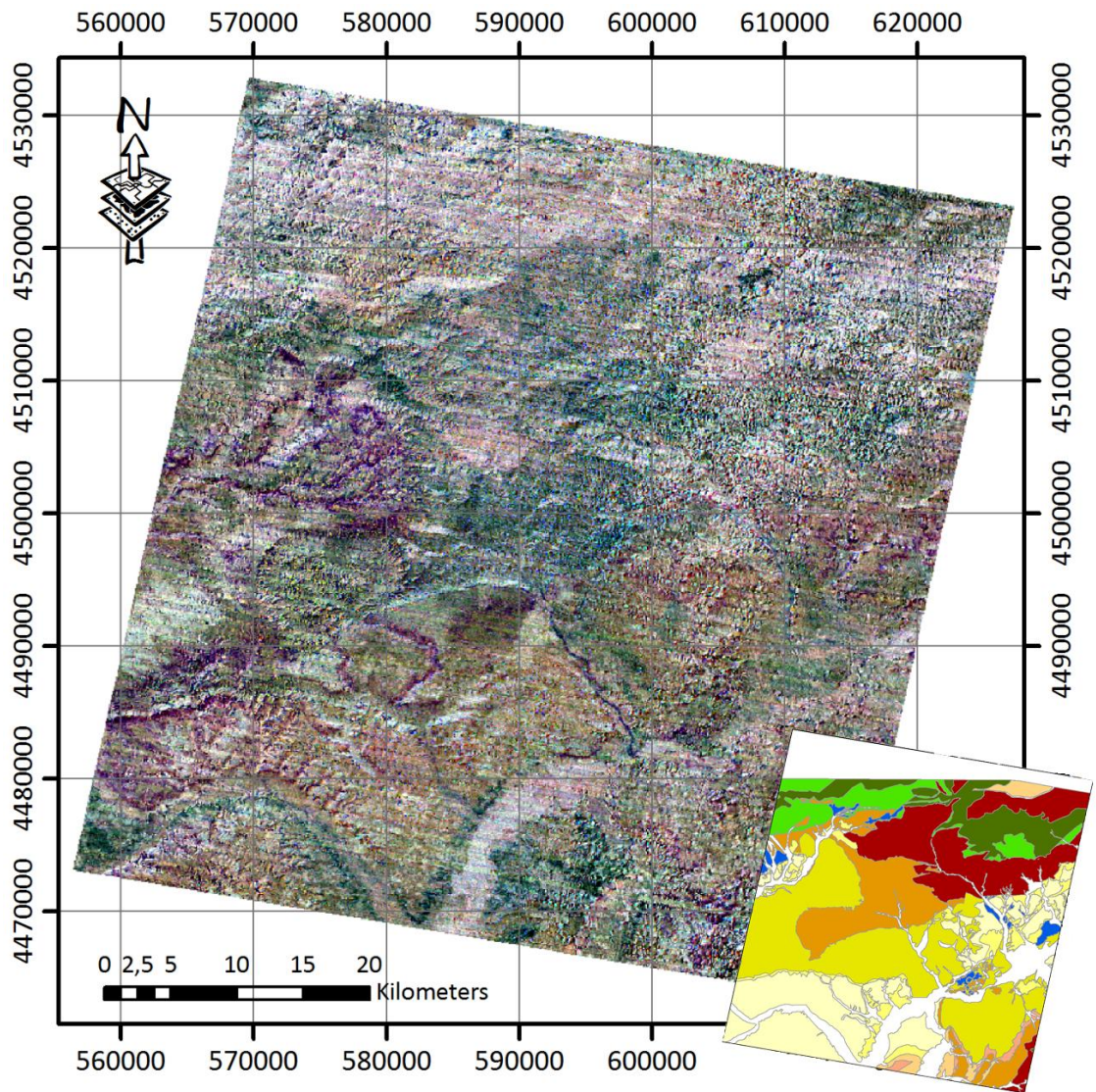
Figure 5.24 Emissivity color composite (R: Band-12 G: Band-11 B: Band-10). *See Figure 2.2 for legend of the inset map.*
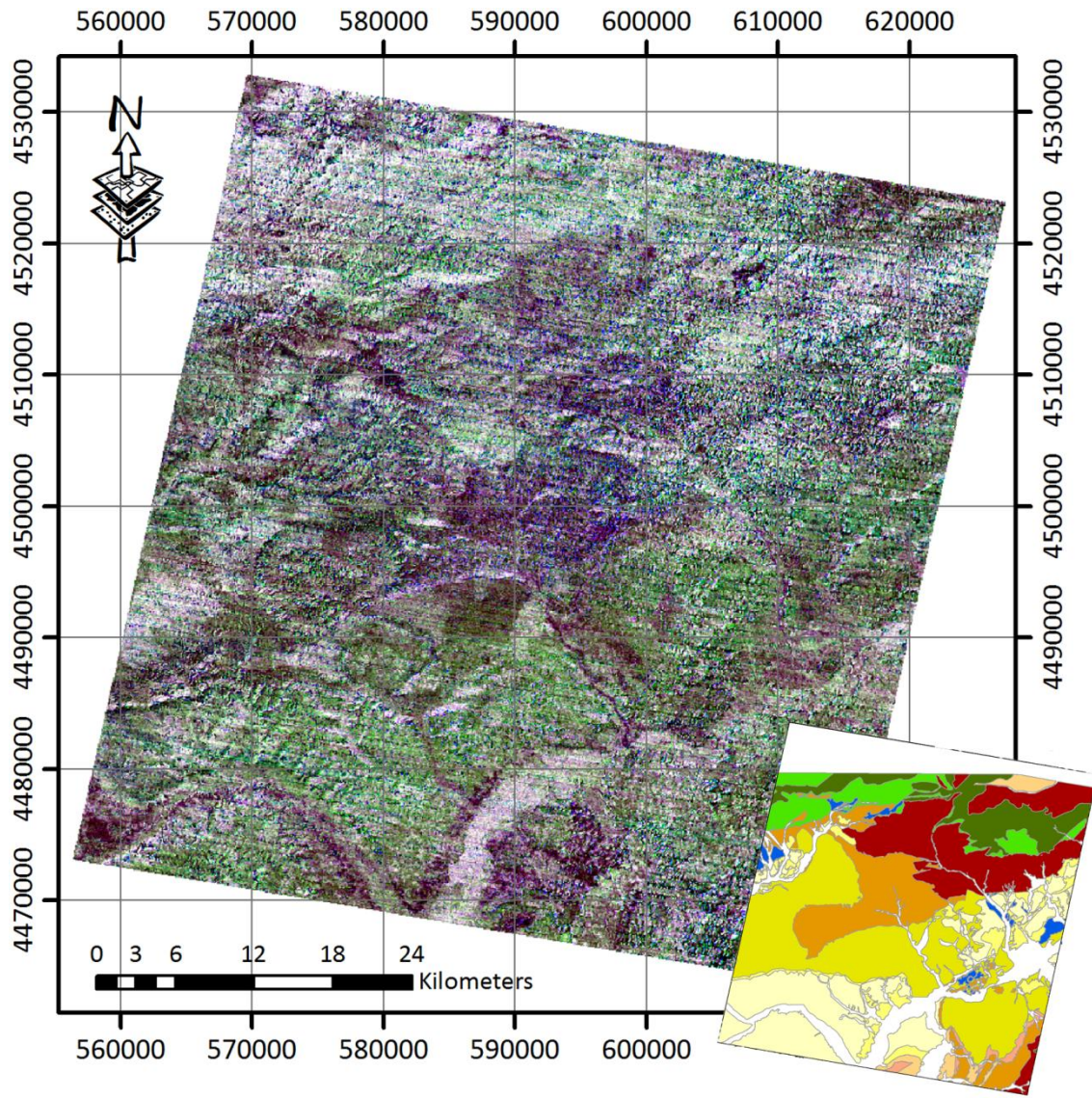
Figure 5.25 Emissivity color composite (R: Band-14 G: Band-12 B: Band-10). *See Figure 2.2 for legend of the inset map.*

Some regions showed quite different emissivity responses than their surroundings on the RGB color composites. The geographical and physical properties of these regions are quite similar to those of their surroundings, such that the aspect, elevation and color of these regions are not greatly different than their immediate vicinity. Furthermore, these regions are not considered to be different lithological units but mapped together with their surroundings. So, despite the similar geographical, physical properties the regions that have diversified emissivity responses

than their immediate vicinity are considered being anomalous regions which require further inspection. Note that these anomalous regions were not recognized in the previous methods.

Regardless of the band combination used for the RGB color composites anomalous regions are presented in the same localities on the images. These anomalous regions can be delineated from surroundings however identification of these regions is not possible and requires field validation. On Figure 5.26 the anomalous regions are highlighted and these regions are examined in the field.
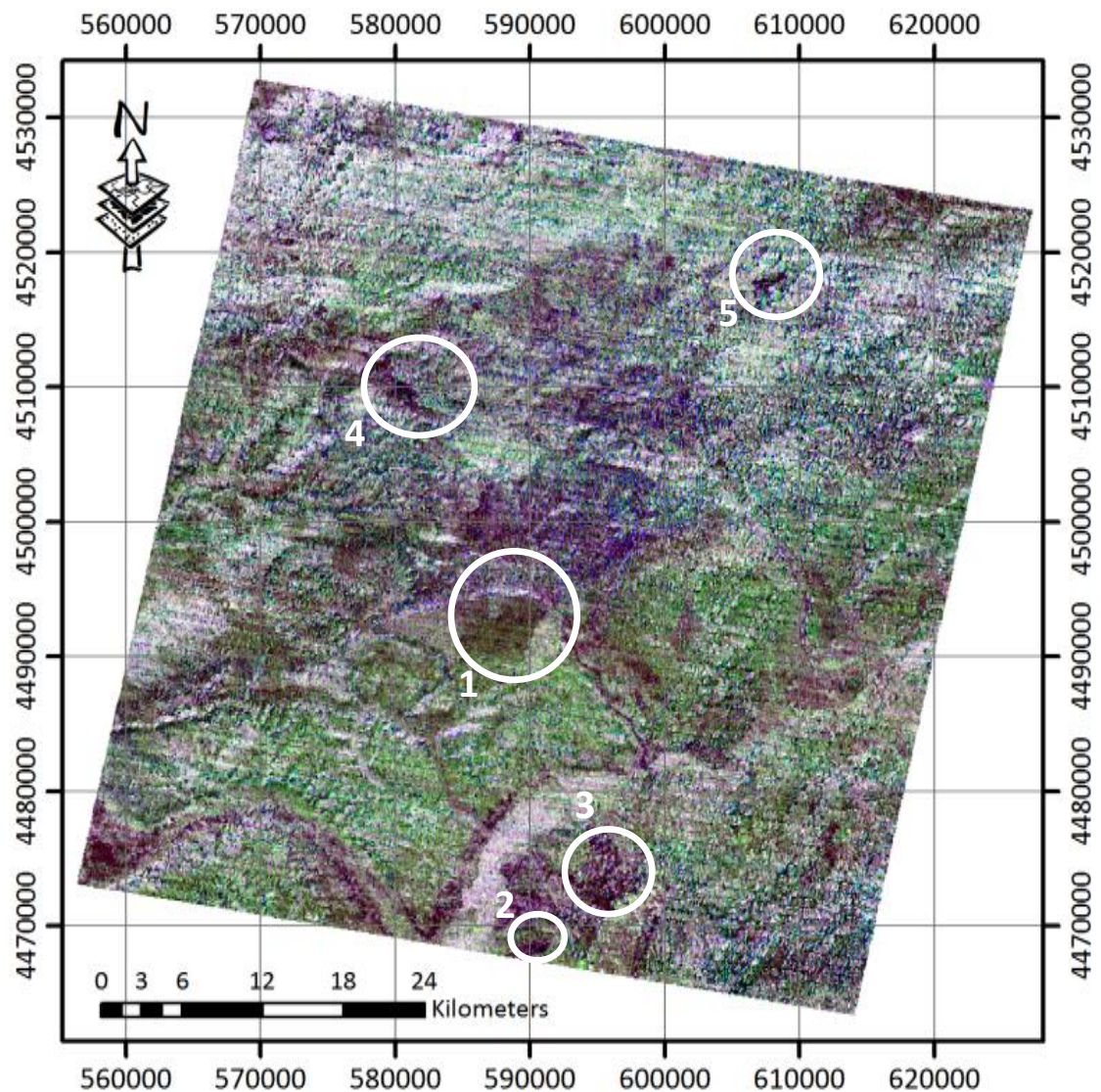
Figure 5.26 RGB color composite of emissivity values showing anomalous regions (R: Band-14, G: Band-12, B: Band-10). White circles indicate the anomalous regions examined in the field.

The first locality is the largest anomaly region that stands out near Satıyüzü. Field observations show that there is no distinct lithology or single surface material is presented however the anomaly represents a distinct property of a mixture of surface materials. The brownish region characterized by a sharp border is agricultural area where fragments of gypsum is collected and emplaced randomly by farmers (Figures 5.27 and 5.28).

Figure 5.27 General view of gypsum fragments accumulated by the farmers on the sides of fields in the first locality

Figure 5.28 Gypsum fragments collected and emplaced nearby the agricultural fields in the first locality

The area also comprises several points where dissolved sub-terrestrial gypsum is transported and recrystallized on the surface (Figure 5.29). The soil in the area that causes the anomaly is plowed every season by the farmers. The plowing of the surficial material creates a mixture mainly comprises clay, and gypsum. Note that gypsum may be presented either directly in the agricultural soil or as rock fragments emplaced nearby the agricultural area. The spectral response of this mixture is happened to be quite different from nearby areas. Therefore, it can be claimed that the main reason for the anomaly would is the mixture of surface materials presented in the area.

Figure 5.29 Recrystallization of dissolved sub-terrestrial gypsum on the surface in the first locality

The second and third localities are quite close to each other. These localities together show the second largest anomaly that stands out in the study area. The field observations show that the locations with emissivity anomalies corresponds the areas where organic matter is presented with various amounts (Figures 5.30 and 5.31).

The field observations cover only the first three localities highlighted on Figure 5.16. Although two additional localities highlighted on the image, due to the accessibility problems the last two localities were excluded from field observation.
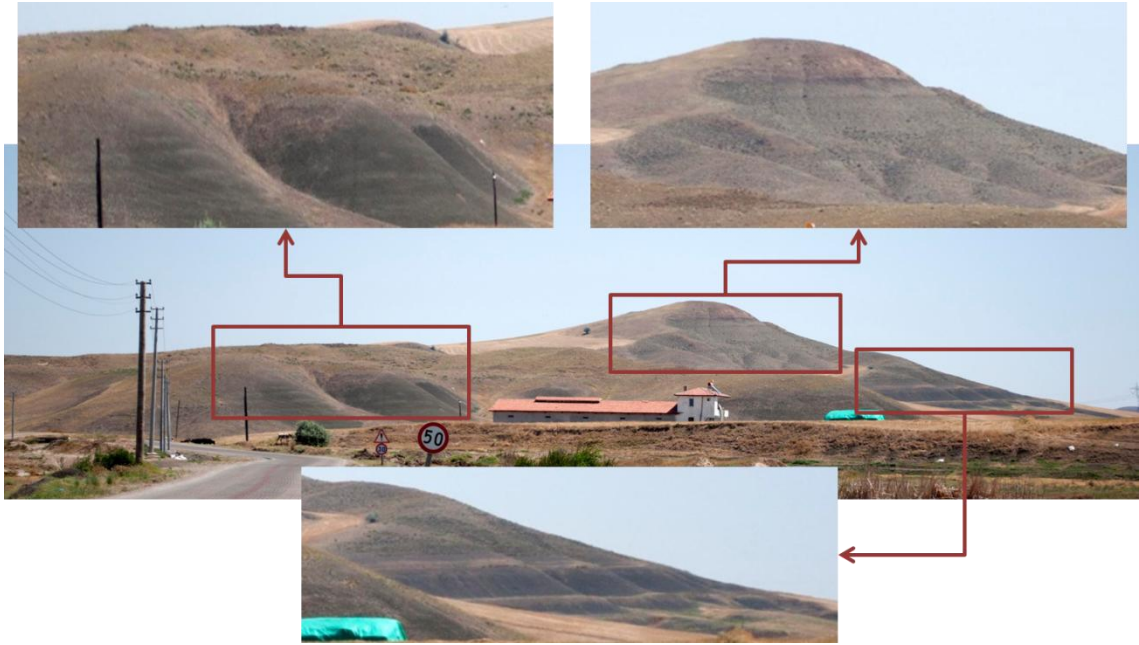
Figure 5.30 General view from the third locality: surface materials that bear organic matter
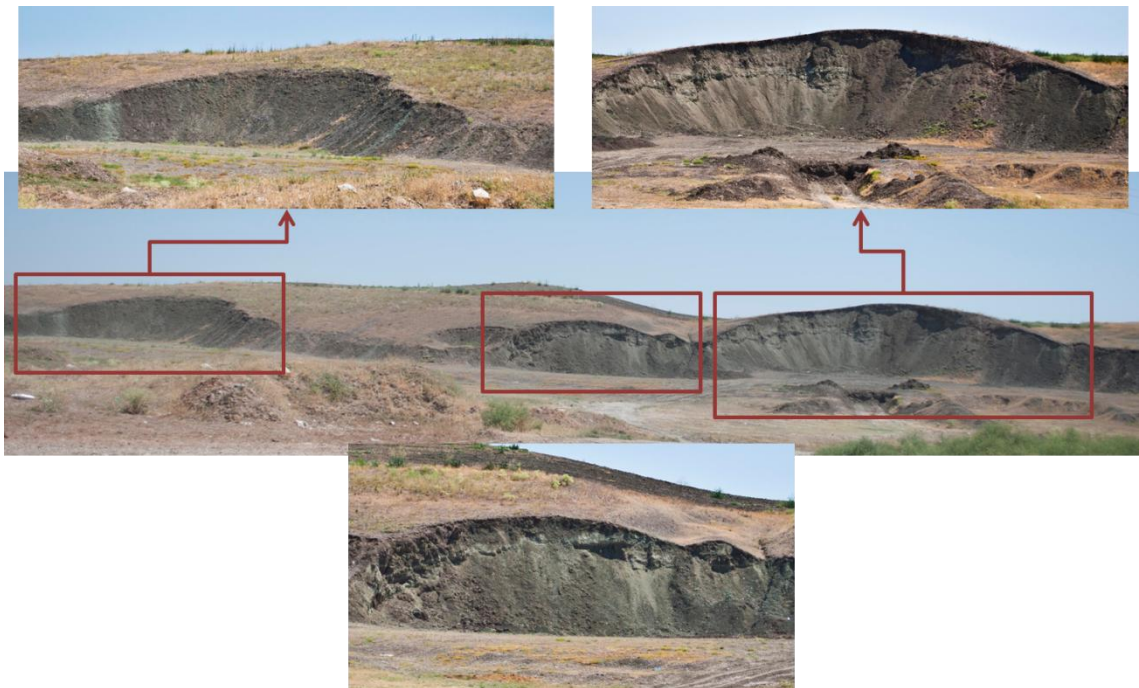
Figure 5.31 Close-up view of the organic matter bearing surface material in the second locality
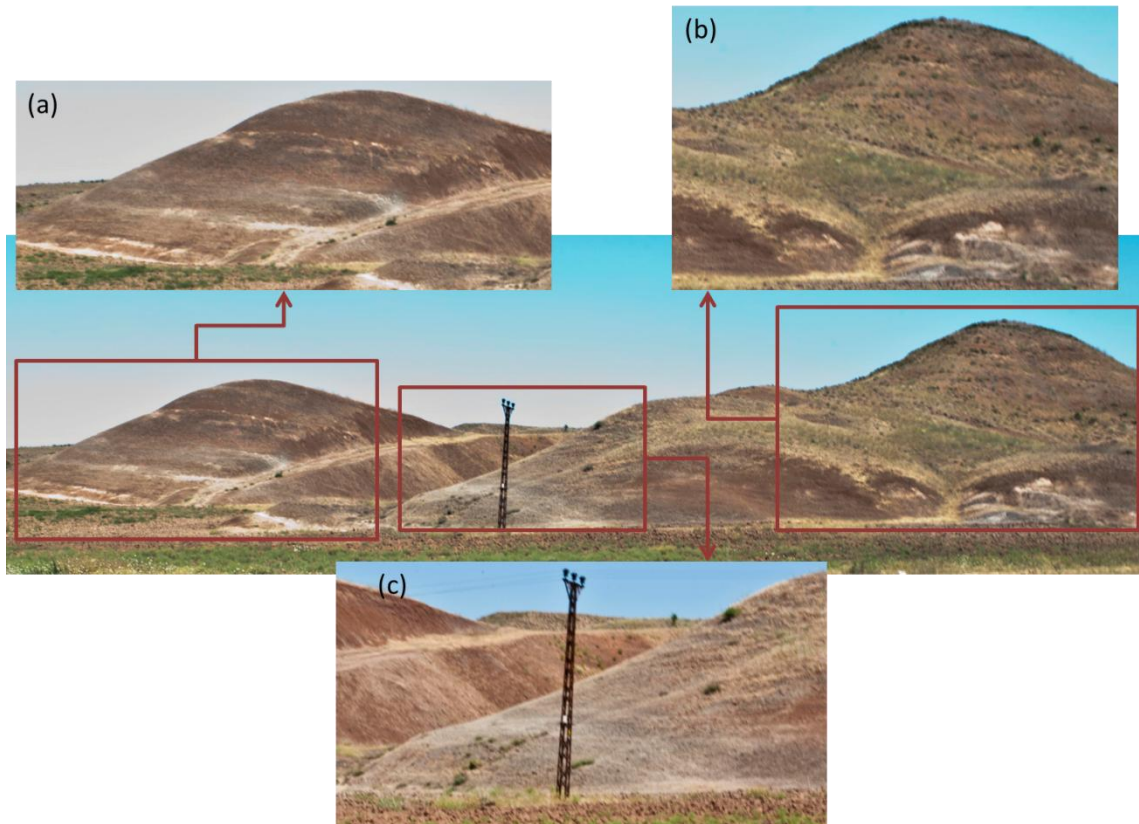
Figure 5.32 A view of Süleymanlı Formation: (a) and (b) sections free from organic matter and (c) organic matter bearing section

5.5.1. Principal Component Analysis of TES Emissivities

An additional PCA is conducted for the emissivities retained from TES algorithm. Even though the vegetated pixels are treated separately in TES algorithm and an appropriate emissivity value is assigned to those pixels, for better accuracy in PCA, NDVI mask is also used.

The transformation parameters of PCA are provided in detail in Table 5.4. The principal components of TES emissivities are also displayed in RGB color composite for interpretation. Similarly, the first RGB color composite is produced from the first three principal components (RGB: PC1, PC2, PC3) in order to represent as much data as possible (Figure 5.26). The first three principal components represent 94% of the data; 78.5%, 10.6% and 4.8% respectively.

Additional RGB color composites are also produced from PC2, PC3 and PC4 (RGB: PC2, PC3, PC4) (Figure 5.27). PC2 represents 10.6% of the data and together with PC3 and PC4, the

represented data increases only to 16%. The last RGB color composite produced from PC3, PC4 and PC5 (RGB: PC3, PC4, PC5) represents 11% of the data (Figure 5.28).

Table 5.4 PCA parameters ASTER band emissivities

MEAN RASTER VALUES	
RASTER	**MEAN**
TES EMISS 10	0,90
TES EMISS 11	0,90
TES EMISS 12	0,90
TES EMISS 13	1,00
TES EMISS 14	1,00

VARIANCE/COVARIANCE MATRIX					
RASTER	**TES EMISS 10**	**TES EMISS 11**	**TES EMISS 12**	**TES EMISS 13**	**TES EMISS 14**
TES EMISS 10	0,0006	0,0004	0,0003	0,0002	0,0001
TES EMISS 11	0,0004	0,0005	0,0003	0,0002	0,0001
TES EMISS 12	0,0003	0,0003	0,0003	0,0002	0,0001
TES EMISS 13	0,0002	0,0002	0,0002	0,0001	0,0001
TES EMISS 14	0,0001	0,0001	0,0001	0,0001	0,0001

CORRELATION MATRIX					
RASTER	**TES EMISS 10**	**TES EMISS 11**	**TES EMISS 12**	**TES EMISS 13**	**TES EMISS 14**
TES EMISS 10	1,0000	0,7726	0,6552	0,5908	0,5668
TES EMISS 11	0,7726	1,0000	0,8105	0,6882	0,5997
TES EMISS 12	0,6552	0,8105	1,0000	0,7122	0,6724
TES EMISS 13	0,5908	0,6882	0,7122	1,0000	0,6375
TES EMISS 14	0,5668	0,5997	0,6724	0,6375	1,0000

EIGENVALUES AND ASSOCIATED PRECENTAGES			
AXIS	**EIGENVALUES**	**PERCENTAGES**	**CUMULATIVE**
1	0,0013	78,5693	78,5693
2	0,0002	10,6226	89,1919
3	0,0001	4,8576	94,0495
4	0,0001	3,4429	97,4924
5	0,0000	2,5076	100,0000

EIGENVECTORS					
RASTER	**TES EMISS 10**	**TES EMISS 11**	**TES EMISS 12**	**TES EMISS 13**	**TES EMISS 14**
TES EMISS 10	0,6187	0,5569	0,4494	0,2553	0,1998
TES EMISS 11	-0,7505	0,2181	0,5456	0,2539	0,1643
TES EMISS 12	0,1831	-0,7305	0,2172	0,3883	0,4846
TES EMISS 13	-0,1134	0,2592	-0,6333	0,7038	0,1536
TES EMISS 14	-0,0872	0,2034	-0,2282	-0,4736	0,8214
TOTAL VARIANCE			0,0016		
DETERMINANT			0,0000		

TRANSLATION VECTOR				
1,9318	0,4198	0,5356	0,3749	0,2333

TRANSFORMATION MATRIX					
RASTER	**TES EMISS 10**	**TES EMISS 11**	**TES EMISS 12**	**TES EMISS 13**	**TES EMISS 14**
TES EMISS 10	0,2974	0,2677	0,2160	0,1227	0,0961
TES EMISS 11	-0,3884	0,1129	0,2823	0,1314	0,0850
TES EMISS 12	0,0914	-0,3646	0,1084	0,1938	0,2418
TES EMISS 13	-0,0608	0,1391	-0,3399	0,3777	0,0824
TES EMISS 14	-0,0481	0,1122	-0,1258	-0,2611	0,4529

CORRELATION BETWEEN INPUT RASTERS AND PRINCIPAL COMPONENT					
RASTER	**TES EMISS 10**	**TES EMISS 11**	**TES EMISS 12**	**TES EMISS 13**	**TES EMISS 14**
TES EMISS 10	0,9104	0,9362	0,8740	0,7626	0,7036
TES EMISS 11	-0,4061	0,1348	0,3902	0,2789	0,2127
TES EMISS 12	0,0670	-0,3054	0,1050	0,2884	0,4242
TES EMISS 13	-0,0349	0,0912	-0,2578	0,4400	0,1132
TES EMISS 14	-0,0229	0,0611	-0,0793	-0,2527	0,5167
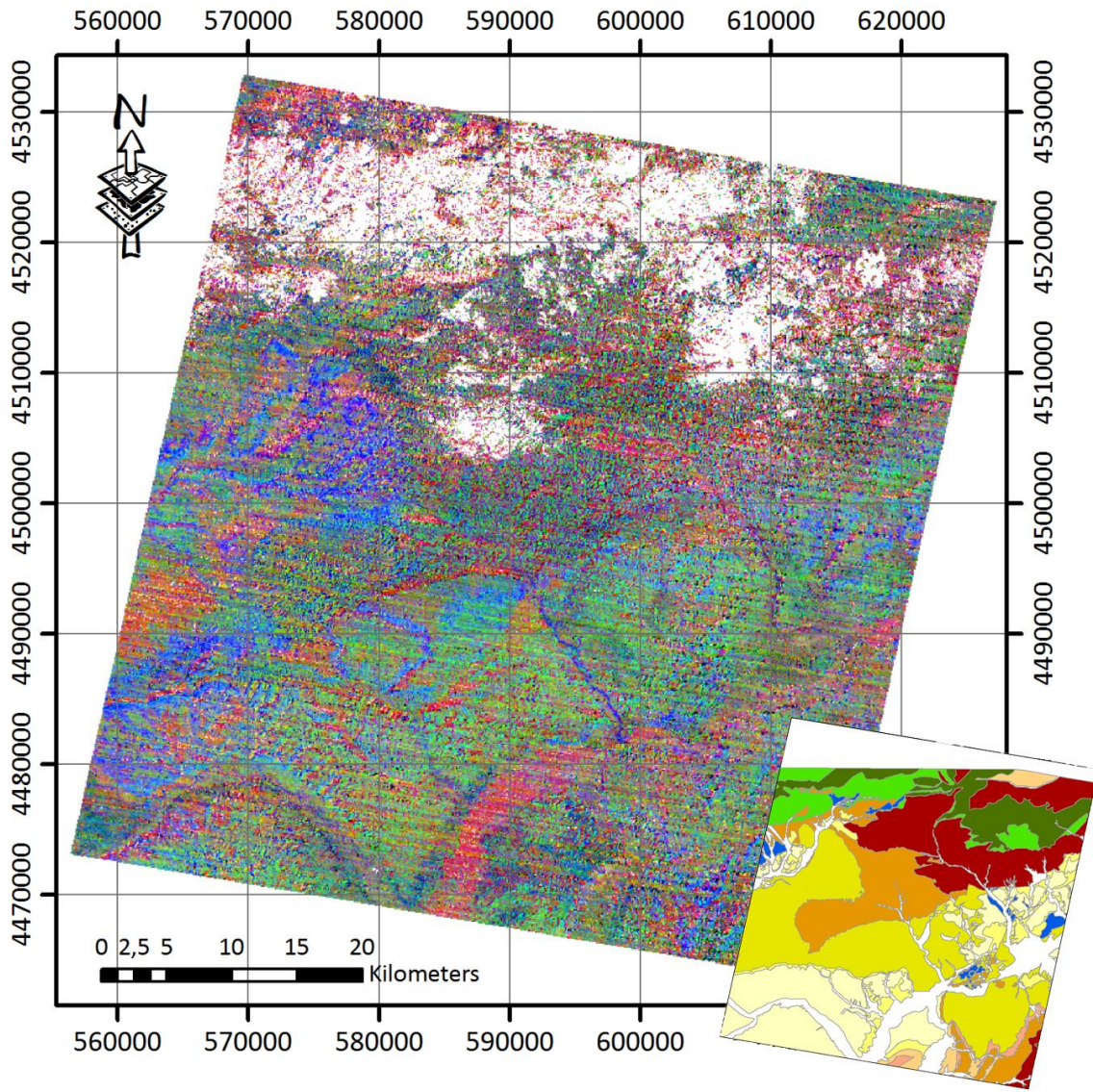
Figure 5.33 RGB color composite of principal components of band emissivities (R: PC1, G: PC2, B: PC3). *Note that the white area on the figure represents the vegetation. See Figure 2.2 for legend of the inset map.*
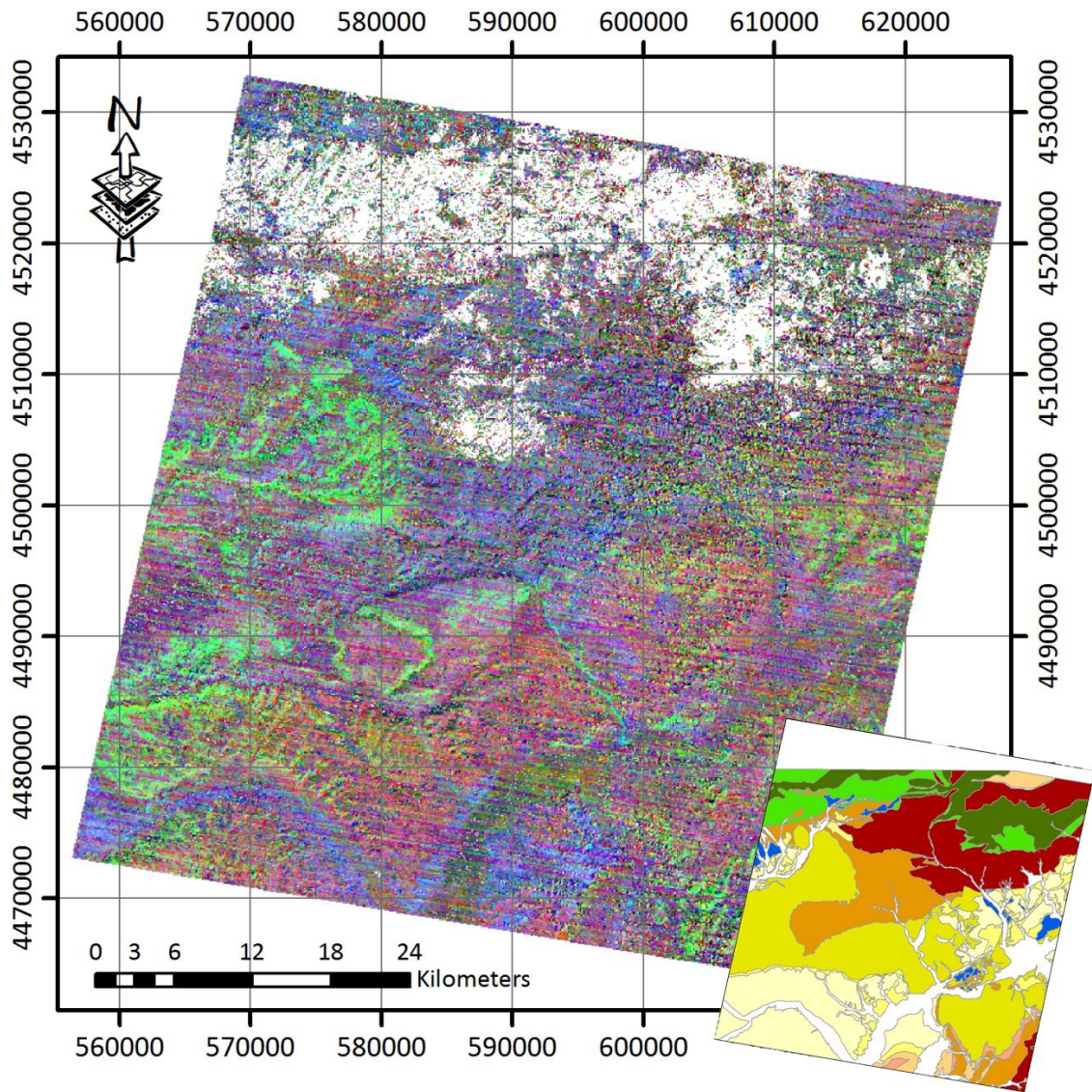
Figure 5.34 RGB color composite of principal components of band emissivities (R: PC2, G: PC3, B: PC4). *Note that the white area on the figure represents the vegetation. See Figure 2.2 for legend of the inset map.*
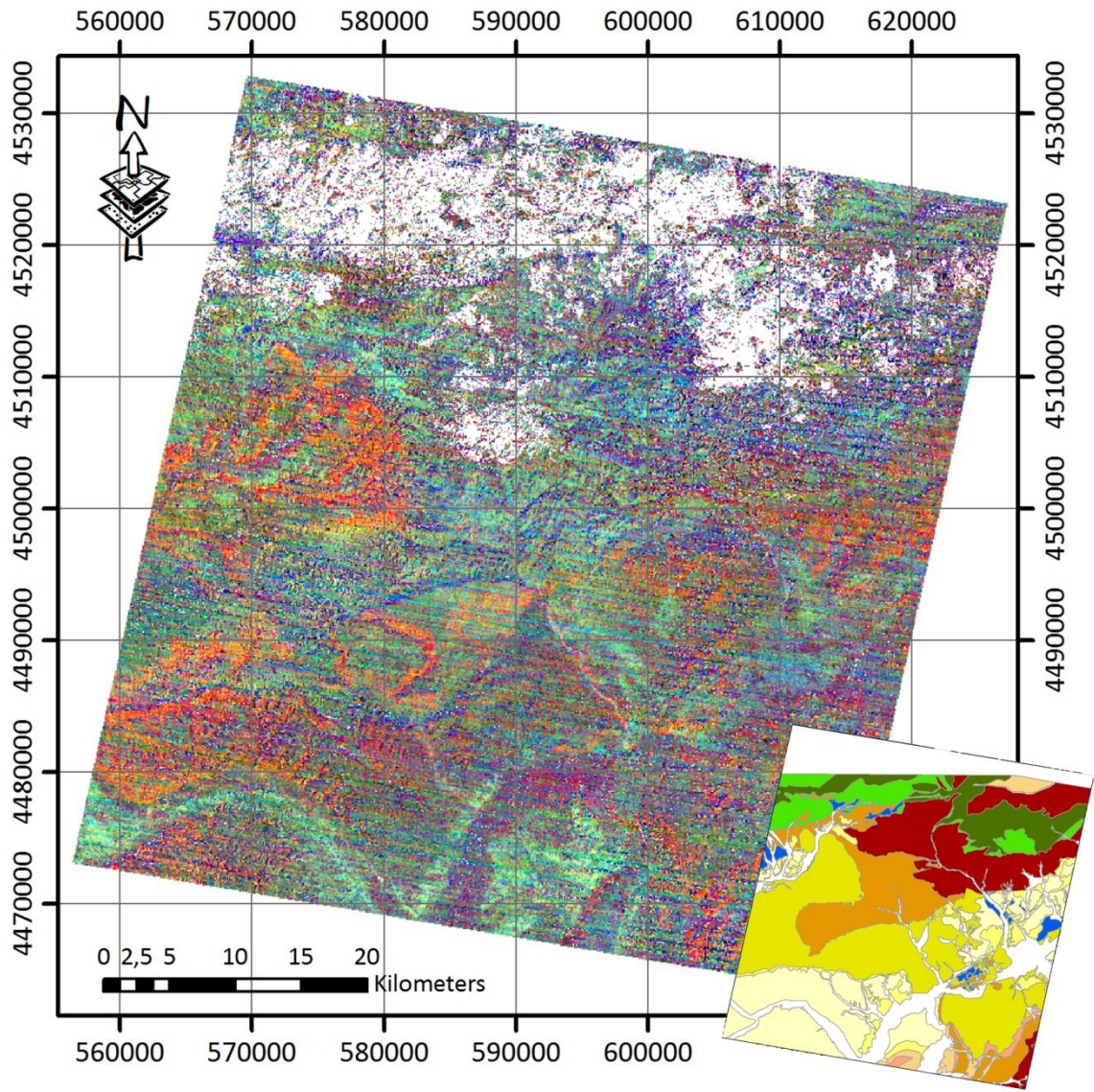
Figure 5.35 RGB color composite of principal components of band emissivities (R: PC3, G: PC4, B: PC5). *Note that the white area on the figure represents the vegetation. See Figure 2.2 for legend of the inset map.*

CHAPTER 6

DISCUSSION AND CONCLUSION

The purpose of this study was to evaluate the ASTER multispectral data for lithological discrimination and mapping; more precisely, to evaluate the capacity and usability of emissivity with respect to conventional remote sensing techniques such as PCA, decorrelation stretch and spectral indices. This chapter includes discussions on the findings in this study, limitations, recommendations for future studies and conclusion.

6.1. Discussions

The RGB color composites images produced using preprocessed ASTER VNIR and SWIR data is used only for preliminary interpretation which is mainly based on known physico-chemical properties of the materials. Based only on these color composites surface material discrimination and mapping is not feasible since the information embedded in the images is not greatly different in immediate vicinity.

The results of the principal component analysis showed that through interpretation of RGB color composites produced using principal components is capable to discriminate surface materials based on the variance between the materials. Based on the selection of the principal components the materials delineated may change. In this study, the combinations of principal components led mainly discrimination of continental red clastics (İncik Formation) and evaporites (Tuğlu and Bozkır Formations). Discrimination of two evaporitic units separately, however, is not explicit. Only one of the RGB color composite was capable to discriminate Bozkır and Tuğlu formations tentatively. Another RGB color composite was capable to

discriminate Paleocene-Eocene units in the north-east of the image. The principal component analysis has an intrinsic identification problem of the materials. This can be considered being the main drawback of the PCA that is the principal components are defined mathematically so that the maximum variance in the image is guaranteed however what does an individual component represent is not certain. Identification of principal components needs either additional data such as geological map and/or land-cover map or direct field observations. In this study, the geological map of the study area is utilized for identification of the principal components.

Decorrelation stretch eliminates this draw-back through retransformation of the component to their original coordinate system such that the resultant components exactly match the input data but the contrast is enhanced. Therefore, the corresponding ASTER band of each color is known and as long as the spectral response of materials is known it can be used for surface material discrimination and also identification. The results of the decorrelation stretch was capable of discriminating clastics (İncik Formation) and evaporites (Tuğlu and Bozkır Formation), however, discrimination of evaporitic units separately was not possible.

Spectral indices are defined based on empirical analysis along with the spectral responses of the surface materials. Essentially, the idea behind spectral indices is not to discriminate first and identify the material but rather to discriminate the material through identification. In other words, spectral indices focus on specific materials and identifies on the image. Since the number of the indices is limited it can only be utilized for limited minerals. The main drawback of utilizing spectral indices is that even though it relies on numerical calculation there are no absolute values that would show the presence of the material and these results of calculations are not reproducible. In other words, the indices are scene dependent and as are not normalized it is not possible to compare between scenes. In that manner it also requires visual interpretation either on image or through field validation.

When it is compared to the previous methods used, using emissivity for surface discrimination is quite unused and needs more inspection and evaluation. The results obtained in this study are rather peculiar. Regardless of the band combination used for the RGB color composites anomaly regions are presented in the same localities on images. These anomalous regions can be delineated from surroundings however identification of these regions is not possible and

84

requires field observation. The field observations showed that the anomalous regions correspond to the areas bearing organic matter at various amounts. Note that discrimination of the organic matter bearing surface material has not been possible through utilizing only VNIR and SWIR bands due to the fact that the organic matter in surface materials dominates the spectral response of the materials. Clark (1983) stated that intimate mixtures of clay and organic matter cause non-linear aspects on reflectance spectra. Organic matter as low as 2.5% in clay flattens the reflection and absorption features while not changing the rest of the reflectance spectra (Clark, 1999). This feature makes discrimination and identification of the materials that bears organic matter impossible. In that regard, utilizing emissivity for surface material discrimination shows potential and needs further assessment.

On the other hand, visual interpretation of RGB color composites of band emissivities is not capable of discriminating surface materials as in the previous materials. In other words, except the anomalous regions no distinct unit stands out on the RGB color composites of band emissivities. The results of the principal component analysis of emissivities, however, highlighted several features of surface materials. It can be said that along with the PCA the level of discrimination has increased. In other words, PCA of TIR band emissivities was capable to discriminate surface materials than PCA of VNIR and SWIR band radiances. Having said that PCA still has its intrinsic draw back that is it is not possible to identify what is highlighted and need field validation. Nonetheless, it provides spatial information for mapping purposes. When the results of PCA compared with the visual interpretation of RGB color composite the same localities that have organic matter content stand out as one of the principal components and highlighted as very light green. It can be said that utilizing TIR emissivity values characteristic for materials would be more efficient rather than utilizing radiance values particularly in PCA. For spectral indices method, however, utilizing TIR radiances or TIR emissivities would not change the final output. Although the quantitative values are changed the pattern and the brighter regions that show the locations of the minerals stay the same. Therefore, utilizing emissivity values for spectral indices is not worth, unless the target is large and homogenous enough to create a particular spectral character. Note that the process including but not limited to temperature-emissivity separation is not straightforward and user-friendly.

6.1.1. Discussion on Research Questions

1. The results show that utilizing emissivity has potential for surface material discrimination and mapping. Through anomalous regions and pixels different units that have distinct spectral responses can be delineated visually. Furthermore, principal component analysis of emissivities also showed that emissivities bear representative information regarding the surface materials. The main draw-back here is that distinct units can be discriminated but not identified without additional data such as geological map and/or field observation.

2. The anomalous pixels or regions detected through visual interpretation of emissivities and PCA of emissivities could not be discriminated through previously used techniques. Therefore, it can be said that using emissivitities can increase the discrimination level to some extend at least for some of the specific materials. In this study, as mentioned before the field validations showed that the anomalous regions detected contains organic matter which could not be discriminated by any of the previous methods.

6.1.2. Limitations

1. The atmospheric effect in the thermal bands of ASTER is compensated through ISAC (In-scene Atmospheric Compensation) which provides ground-leaving radiance as explained before. The ISAC uses merely in-scene parameters for atmospheric compensation while the local atmospheric parameters and conditions on the acquisition date are not known explicitly. Since the atmospheric parameters are not the main concern for this study utilizing ISAC for atmospheric compensation is considered being sufficient. However, should the atmospheric parameters are in question a radiative transfer model could be used for recovering these parameters quantitatively. Moderate Resolution Atmospheric Transmission (MODTRAN) a computer program designated to model the atmospheric propagation of radiation. Using MODTRAN for recovering atmospheric parameters and using them for atmospheric correction may refine the land-leaving radiance since local parameters are utilized. Note that removal of the reflected down-welling sky irradiance in NEM module of TES algorithm is iterative. A reflection factor $(1-\varepsilon)$ accompanies the down-welling sky irradiance. Since the maximum emissivity value is selected for NEM is greater than 0.9 (mostly 0.96 for

surface material) the effect of the down-welling sky irradiance on the land-leaving radiance would not be significant.

2. The spatial resolution of TIR bands of ASTER (90m) is quite coarse for reflecting detailed information about surface materials. Spectral mixing is one of the main draw-back of TIR. In other words, one ASTER TIR pixel covers 8100 meter-square (8.1 decare) on the Earth's surface which likely to comprise different surface materials in its extent. Therefore, unless the materials have broad extent it is highly possible to be missed by ASTER TIR pixels or near homogenously mixed materials having broad extent clay, organic matter and gypsum for our case can show a surface anomaly and be seen as a distinct unit through visual interpretation of emissivity images. Note that without field validation identification of such cases would not be possible.

3. Quantitative comparison and/or classification of surface materials through emissivity values are not seem to be feasible. Two reasons govern this argument: (1) Laboratory spectrum results which are used for emissivity extraction represents the materials under constant temperature. Note that emissivity of a material will change with change in its temperature and this change is not straightforward to be predicted. Moreover, as stated before the emissivity values of surface material vary 0.9 and 1.0 which is quite narrow for detection of changes. This change in emissivity values is thought to be order of thousandth to ten-thousandth which requires sensitive calculation and classification procedure. (2) Emissivity values of surface materials would be affected by physical and/or slight chemical weathering, thin acute vegetation and again thin acute dust/soil cover on the material.

4. In the TES algorithm due to its intrinsic mathematical approach some of the resultant pixels are saturated and have emissivity values greater than 1.0 which is obviously not possible in the nature. These pixels create noise on the data and identified with salt-pepper pattern. Apart from that emissivity images inherit the systematic noise presented in ASTER TIR data which affect the image quality.

5. The radiance readings of pixels are affected by the insolation therefore based on topography the incident radiation may vary which will affect the calculations and interpretations of both temperature and emissivity. For instance, while foot slopes are

illuminated back slopes would remain in shadow which will directly affect the calculation of surface brightness temperature and therefore surface material emissivity.

6.1.3. Recommendations for Future Studies

1. As stated in the limitations MODTRAN can be used for atmospheric correction and recovering atmospheric parameters if those parameters are in question. Moreover, using these parameters through NEM module while reflected sky irradiance is removed iteratively, the maximum emissivity values can also be refined for better NEM outputs.

2. The effect of insolation discussed in the previous section would be compensated in order to have more homogenous distribution of temperature and emissivity. The insolation parameters can be calculated through software such as ArcGIS which provide direct and diffuse insolation images separately. Accordingly, the dimly illuminated pixels such as back slopes would be illuminated artificially or more precisely the illumination would be increased artificially in order to have homogenous distribution on the original image.

3. Instead of multispectral spaceborne data having low spatial and spectral resolution, hyperspectral airborne data would be utilized. Airborne hyperspectral data for TIR can be obtained from HyMap, EPS-H (Environmental Protection System), DAIS 21115 and DAIS 7915 (Digital Airborne Imaging Spectrometer) sensors. One of the advantages of using airborne data would be acquisition of data in different spatial resolutions.

6.2. Conclusion

Utilizing emissivity values possesses significant potential for surface material discrimination and mapping since it shows diversified properties of materials. Particularly, for surface materials bearing organic matter that has not been possible through utilizing VNIR and SWIR radiances. Furthermore, utilizing emissivity values in PCA increase the level of discrimination for the surface materials even further. Despite its potential since the utilization of emissivity values are rather unused throughout in literature and new, further accuracy assessment and field validation are also needed. Emissivity utilization for discrimination of organic matter bearing surface materials should be tested on different and preferably well-known areas that have diversified environmental (vegetation, temperature, atmospheric parameters etc.) and observational (date and time of the observation, azimuth and solar angle) settings.

REFERENCES

ASTER GDS. (2010, 3 12). Retrieved 07 25, 2012, from ASTER-ERSDAC GDS Web site: http://gds.aster.ersdac.jspacesystems.or.jp/gds_www2002/news20100312_e.html

Abrams, M. J., Abbott, E. A., & Kahle, A. B. (1991). Combined Use of Visible, Reflected Infrared and Thermal Infrared Images for Mapping Hawaiian Lava Flows. *Journal of Geophysical Research, 96*(B1), 475-484.

Abrams, M. J., Kahle, A. B., Palluconi, F. D., & Schieldge, J. P. (1984). Geological Mapping Using Thermal Images. *Remote Sensing of the Environment, 16*, 13-33.

Allis, R. G., Nash, G. D., & Johnson, S. D. (1999). Conversion of Thermal Infrared Surveys to Heat Flow: Comparisons from Dixie Valley, Nevada and Wairakei, New Zealand. *Geothermal Resources Transactions, 23*, 17-20.

Barton, I. J. (1985). Transmission model and ground truth investigation of satellite derived sea surface temperatures. *Journal Climate and Applied Meteorology, 24*, 508-516.

Becker, F. (1987). The impact of spectral emissivity on the measurement of land surface temperatures from satellite. *International Journal of Remote Sensing, 8*(10), 1509-1522.

Becker, F., & Li, Z. L. (1990). Temperature-Independent Spectral Indices in Thermal Infrared Bands. *Remote Sensing of Environment, 32*, 17-32.

Brown, O. B. (1994). MODIS Infrared sea surface temperature algorithm. *Algorithm Theoretical Basis Document, NASA Contract Number NAS5-31361*.

Chabrillat, S., Pinet, P. C., Ceuleneer, G., Johnson, P. E., & Mustard, J. F. (2000). Ronda Peridotite Massif: Methodology for its geological mapping and lithological discrimination from airborn hyperspectral data. *International Journal of Remote Sensing, 21*(12), 2363-2383.

Clark, R. N. (1983). Spectral Properties of Mixtures of Montmorillonite and Dark Carbon Grains: Implications for Remote Sensing Minerals Containing Chemically and Physically Absorbed Water. *Journal of Geophysical Research, 88*, 10635-10644.

Clark, R. N. (1999). Chapter1: Spectroscopy of Rocks and Minerals and Principles of Spectroscopy. In A. N. Rencz (Ed.), *Manual of Remote Sensing, Volume 3, Remote Sensing for the Earth Sciences* (pp. 3-58). New York: John Wiley and Sons, Inc.

Corrie, R. K., Ninomiya, Y., & Aitchison, J. C. (2010). Applying Advanced Spaceborne Thermal Emission and Reflection Radiometer (ASTER) Spectral Indices for Geological Mapping and Mineral Identification on the Tibetian Plateau. *Internationaş Archieves of the Photorammetry, Remote Sensing and Spatial Information Science, XXXVIII*(Part 8), 464-469.

Crist, E. P., & Cicone, R. C. (1984). A physically-based transformation of Thematic Mapper data-the TM tasseled cap. *IEEE Transactions on Geoscience and Remote Sensing, 22*, 256-263.

DiStasio, J. R., & Resmini, R. G. (2010). Atmospheric Compensation of Thermal INfrared Hyperspectral Imagery with the Emissive Emprical Line Method and the In-Scene Atmospheric Compensation Algorithm: A Comparison.

Dudley-Murphy, E. A., & Nash, G. D. (2003). TIR (ASTER) Geothermal Anomalies. *Geothermal Resources Council Transactions, 27*, 645-647.

Gillespie, A. R. (1985). Lithologic Mapping of Silicate Rocks Using TIMS. *The TIMS Data Users' Workshop, June 18-19, 1985*, 29-44.

Gillespie, A. R. (1992). Spectral mixture analysis of multispectral thermal images. *Remote Sensing of Environment, 42*, 137-145.

Gillespie, A. R., Kahle, A. B., & Walker, R. E. (1986). Color enhancement of highly correlated images. I.Decorrelation and HIS contrast stretches. *Remote Sensing of Environment, 20*, 209-235.

Gillespie, A. R., Rokugawa, S., Hook, S. J., Matsunaga, T., & Kahle, A. B. (1999). Temperature/Emissivity Separation Algorithm Theoretical Basis Document, Version 2.4.

Gillespie, A. R., Rokugawa, S., Matsunaga, T., Cothern, J. S., Hook, S. J., & Kahle, A. B. (1998). A Temperature and Emissivity Separation Algorithm for Advanced Spaceborne Thermal Emission and Reflection Radiometer (ASTER) Images. *IEEE Transactions on Geoscience and Remote Sensing, 36*(4), 1113-1126.

Gürçay, O. B. (2010, July 5-7). Extracting Olivine-rich portions of ultramafic rocks using ASTER TIR data. (W. Wagner, & B. Székely, Eds.) *ISPRS TC VII Symposium-100 Years ISPRS, XXXVIII*, Part 7B.

Hook, S. J., Abbott, E. A., Grove, C., Kahle, A. B., & Palluconi, F. (1999). Use of Multispectral Thermal Infrared Data in Geological Studies. In N. Andrew (Ed.), *Remote Sensing for the*

Earth Sciences: Manual of Remote Sensing (3. ed., Vol. 3, pp. 59-110). John Wiley & Sons, Inc.

Hook, S. J., Cudahy, T. J., Kahle, A. B., & Whitboum, L. B. (1998). Synergy of Active and Passive Airborne Thermal Infrared Systems for Surface Compositional Mapping. *Journal of Geophysical Research, 103*(B8), 18,269-18,276.

Hook, S. J., Dmochowski, J. E., Howard, K. A., Rowan, L. C., Karlstrom, K. E., & Stock, J. M. (2005). Mapping variations in weight percent silica measured from multispectral thermal infrared imagery-Examples from the Hiller Mountains, Nevada and Tres Virgenes-La Reforma Baja Califormia Sur, Mexico. *Remote Sensing of Environment*, 273-289.

Hook, S. J., Gabell, A. R., Green, A. A., & Kealy, P. S. (1992). A Comparison of Techniques for Extracting Emissivity Information from Thermal Infrared Data for Geologic Studies. *Remote Sensing of Environment, 42*, 123-135.

Kahle, A. B., Madura, D. P., & Soha, J. M. (1980). Middle Infrared Multispectral Aircraft Scanner Data Analysis for Geological Applications. *Applied Optics, 19*, 2279-2290.

Kahle, A. B., Schieldge, J. P., & Alley, R. E. (1984). Sensitivity of Thermal Inertia Calculations to Variations in Environmental Factors. *Remore Sensing of the Environment, 16*, 211-232.

Kaymakçı, N. (2000). *Tectono-stratigraphical Evolution of the Çankırı Basin (Central Anatolia, Turkey).* Ph.D. Thesis [unpublished], Faculty of GeoScience (Vening Meinesz Research School of Geodynamics), Utrecht University.

Kaymakçı, N., Özçelik, Y., White, H. S., & Van Dijk, P. M. (2001). Neogene Tectonic Development of the Çankırı Basin (Central Anatolia, Turkey). *The Bulletin of Turkish Association of Petroleum Geologists, 13*(1), 27-58.

Kaymakçı, N., Özmutlu, Ş., Van Dijk, P. M., & Özçelik, Y. (2010). Surface and Subsurface Characteristics of the Çankırı Basin (Central Anatolia, Turkey): Integration of Remote Sensing, Seismic Interpretation and Gravity. *Turkish Journal of Earth Sciences, 19*, 79-100.

Kaymakçı, N., White, S. H., & Van Dijk, P. M. (2000). Paleostress inversion in a multiphase deformed area: kinematic and structural evolution of the Çankırı Basin (Centrak Turkey), Part 1. In E. Bozkurt, J. A. Winchester, & J. A. Piper (Eds.), Tectonics and Magmatism in Turkey and the Surrounding area. *Geological Society London Special Publications No.173* (pp. 445-473).

Kealy, P. S., & Gabell, A. R. (1990). Estimation of Emissivity and Temperature using Alpha Coefficients. *Proceedings of 2nd TIMS Workshop*.

Kealy, P. S., & Hook, S. J. (1993). Separating Temperature and Emissivity in Thermal Infrared Multispectral Scanner Data: Implication for Recovering Land Surface Temperature. *Geoscience and Remote Sensing, 31*(6), 1155-1164.

Kirchhoff, G. (1860). On the relation between the radiating and absorbing powers of different bodies for light and heat. (F. Guthrie, Ed.) *Philosophical Magazine, 20*(4), 1-20.

Koçyiğit, A. (1991). An example of an accretionary forearc basin from north Central Anatolia and its implications for the history of subduction of neotethys in Turkey. *Geological Society of America Bulletin, 103*, 22-36.

Koçyiğit, A., Özkan, S., & Rojay, B. F. (1988). Examples from the fore-arc basin remnants at the active margin of northern neotethys: Development and emplacement age of the Anatolian Nappe. *METU Journal of Pure Applied Science, 21*(1-3), 183-220.

Landberg, P. T. (1990). Chapter 13: Bosons: blackbody radiation. In P. T. Landberg, *Thermodynamics and statistical mechanics.* Courier Dover Publications.

Masuda, K., Takashima, T., & Takayama, Y. (1988). Emissivity of Pure and Sea Waters for the Model Sea Surface in the Infrared Window Region. *Remote Sensing of Environment, 24*, 313-329.

Matsunaga, T. (1994). A Temperature-Emissivity Separation Methof Using an Emprical Relationship between the Mean, the Maximum and the Minimum of the Thermal Infrared Emissivity Spectrum. *Journal of the Remote Sensing Society of Japan, 14*(2), 230-241.

McMillan, L. M., & Crosby, D. S. (1984). Theory and validation of themultiple window sea surface temperature technique. *Journal of Geophysical Research, 89*(C3), 655-661.

Misra, A., Gupta, R. P., & Sen, A. K. (2007). Using ASTER TIR Radiance and Surface Emissivity Data to Map Lithology and Silica Abundance ina Metamorphic Terrain. *IGARSS-IEEE International Geoscienceand Remote Sensing Symposium*, (pp. 1640-1643).

Nimoniya, Y., & Matsunaga, T. (1997). Estimation of SiO_2 content using simulated TIR remote sensing data generated from spectra measured on the sawed surface of rocks at Cuprite, Nevada. *Proceedings of 30th International Geology Congress, 10*, 49-62.

Ninomiya, Y. (2002). Mapping quartz, carbonate minerals and mafic-ultramafic rocks using remotely sensed multispectral thermal infrared ASTER data. *Proceedings of SPIE, 4710*, 191-202.

Ninomiya, Y. (2003). Advanced remote lithologic mapping in ophiolite zone with ASTER multispectral thermal infrared data. *Proceedings of 3rd IEEE Geoscience and Remote Sensing Symposium (IGARSS'03)*, 1561-1563.

Ninomiya, Y. (2004). Lithologic mapping with multispectral ASTER TIR and SWIR data. *Proceedings of the SPIE, 5234*, 180-190.

Ninomiya, Y., & Fu, B. (2002). Quartz index, carbonate index and SiO2 content index defined for ASTER TIR data. *Journal of Remote Sensing Society of Japan, 22*, 50-61.

Ninomiya, Y., Fu, B., & Cudahy, T. J. (2005). Detecting lithology with advanced spaceborne thermal emission and reflection radiometer (ASTER) multispectral thermal infrared "radiance at-sensor" data. *Remote Sensing of Environment, 99*, 127-139.

Özçelik, Y. (1994). *Tectono-stratigraphy of the Laçin area (Çorum, Turkey).* M.Sc. Thesis [unpublished], Geological Engineering Department, Middle East Technical University, Ankara.

Öztan, N. S. (2008). *Evaporite Mapping in Bala Region (Ankara) by Remote Sensing Techniques.* Ph.D Thesis [unpublished], Middle East Technical University,Geological Engineering Department, Ankara.

Öztan, N. S., & Süzen, M. L. (2011, Mar 20). *International Journal of Remote Sensing, 32*(6), 1651-1673.

Palluconi, F. D., Hoover, G., Alley, R., & Jentoft-Nilsen, M. (1994). Atmospheric correction method for ASTER thermal radiometry over land.

Pearson, K. (1901). On Lines and Planes of Closest Fit to Systems of Points in Space. *Philosophical Magazine, 2*(6), 559-572.

Planck, M. (1914). *The Theory of Heat Radiation* (2. ed.). (M. Masius, Trans.) P.Blakiston's Son & Co.

Prabhakara, C., & Dalu, G. (1976). Remote Sensing of surface emissivity at 9 um over the globe. *Journal of Geophysical Research, 81*(21), 3719-3724.

Prabhakara, C., Dalu, G., & Kunde, V. G. (1974). Estimation of Sea Surface Temperature from Remote Sensing in the 11- to 13- um Window Region. *Journal of Geophysical Research, 79*(33), 5039-5044.

Price, J. C. (1984). Land surface temperature measurements from the split window channels of NOAA 7 Advanced Very High Resolution Radiometer. *Journal of Geophysical Research, 89*, 7232-7237.

Price, J. C. (1985). On the Analysis of Thermal Infrared Theory:The Limited Utility of Apparent Thermal Inertia. *Remote Sensing of Environment, 18*, 59-73.

Realmuto, V. J. (1990). Separating the Effects of Temperature and Emissivity: Emissivity Spectrum Normalization. *Proceedings of 2nd TIMS Workshop*.

Riedl, M. J. (2001). *Optical Design Fundamentals for Infrared Systems* (2. ed.). Bellingham,Washington, USA: SPIE-The International Society for Optical Engineering.

Rowan, L. C., Mars, J. C., & Simpson, C. J. (2005). Lithologic mapping of the Mordor, NT, Australia Ultramafic Complex by using Advanced Spaceborne Thermal Emission and Reflection Radiometer (ASTER). *Remote Sensing of Environment, 99*(1-2), 105-126.

Sabine, C. (1999). Strategies for Mineral Exploration, Ch.8. In A. Renez, *Manual of Remote Sensing* (3. ed., Vol. 3). John Wiley in corporation with ASPRS.

Sabins, F. F. (1987). *Remote Sensing Principles and Interpretation.* New York: W.H. Freeman and Company.

Sakuma, F., Tonooka, H., Ohgi, N., & Ono, H. (2005). Prediction of the radiometric calibration coefficients of ASTER/TIR. *Proceedings of SPIE, 5978*, 277-284.

Saldanha, D. L., Lime E Cunha, M. C., & Haertel, V. (2004). Spectral analysis of soils from mafic/ultramafic rocks of Cerro Mantiqueira, SW of Rio Grande do Sul. *International Journal of Remote Sensing, 25*(20), 4381-4393.

Salisbury, J. W., & D'Aria, D. M. (1992a). Emissivity of Terrestrial Materials in the 8-14 um Atmospheric Window. *Remote Sensing of Environment, 42*, 83-106.

Salisbury, J. W., & D'Aria, D. M. (1992b). Infrared (8-14 um) Remote Sensing of Soil Particle Size. *Remote Sensing of Environment, 42*, 157-165.

Smith, A. M. (2012). *How to convert ASTER radiance values to reflectance: an online guide*. (C. o. Resources, Producer, & University of Idaho) Retrieved May 3, 2012, from www.cnrhome.uidaho.edu/default.aspx?pid=85984

Soha, J. M., & Schwartz, A. A. (1978). Multispectral histogram normalization contrast enhancement. *Proceedings of 5th Canadian Symposium on Remote Sensing*, 86-93.

Swayze, G. A., Higgin, C. T., Clinkenbeard, J. P., Kokaly, R. F., Clark, R. N., Meeker, G. P., et al. (2004). *Preliminary report on using imagign spectroscopy to map ultramafic rocks, serpentinites and tremolite-actinolite-bearing rocks in California.* USGS Open File Report 2004-1304.

Taylor, M. M. (1973, December 10-14). Principal component color display of ERTS imagery. *Third Earth Resources Technology Satellite-1 Symposium, December 10-14, 1*(Section B), 1877-1897.

Tonooka, H. (2012). *ASTER TIR Recalibration*. (T. Laboratory, Producer, & Ibaraki University, Japan) Retrieved May 6, 2012, from http://tonolab.cis.ibaraki.ac.jp/ASTER/RECAL/

Tonooka, H., Sakuma, F., Kudoh, M., & Iwafune, K. (2003). ASTER/TIR onboard calibration status and used-based recalibration. *Proceedings of SPIE, 5234*, 191-201.

Vidal, A. (1991). Atmospheric and emissivity correction of land surface temperatures measured from satellite using ground measurements or satellite data. *International Journal of Remote Sensing, 12*(12), 2449-2460.

Wan, Z., & Dozier, J. (1989). Land-Surface Temperature Measurement from space: Physical Principles and Inverse Modeling. *Geoscience and Remote Sensing, 27*(3), 268-278.

Watson, K. (1992a). Spectral ratio method for measuring emissivity. *Remote Sensing of Environment, 42*, 113-116.

Watson, K. (1992b). Two-temperature method for measuring emissivity. *Remote Sensing of Environment, 42*, 117-121.

Watson, K., Kruse, F. A., & Hummer-Miller, S. (1990). Thermal infrared exploration in the Carlin trend, northern Nevada. *Geophysics, 55*(1), 70-79.

Yamaguchi, Y., & Naito, C. (2003). Spectral indices for lithologic discrimination and mapping by using the ASTER SWIR bands. *International Journal of Remote Sensing, 24*(22), 4311-4323.

Young, S. J., Johnson, R. B., & Hackwell, J. A. (2002). An in-scene method for atmospheric compensation of thermal hyperspectral data. *Journal of Geophysical Research, 107*(D24), 4774.

Yüksel, A., Akay, A. E., & Gündoğan, R. (2008). Using ASTER imagery in land use/cover classification of eastern Mediterranean landscapes according to CORINE land cover project. *Sensors, 8*, 1237-1251.